Light Efficient and Foveated Head-Worn Displays

by

Mehmet Kıvanç Hedili

A Dissertation Submitted to the
Graduate School of Sciences and Engineering
in Partial Fulfillment of the Requirements for
the Degree of

Doctor of Philosophy

in

Electrical and Electronics Engineering

KOÇ ÜNİVERSİTESİ

December 2019

Light Efficient and Foveated Head-Worn Displays

Koç University

Graduate School of Sciences and Engineering

This is to certify that I have examined this copy of a doctoral dissertation by

Mehmet Kıvanç Hedili

and have found that it is complete and satisfactory in all respects,

and that any and all revisions required by the final

examining committee have been made.

Committee Members:

____

Prof. Dr. Hakan Ürey (Advisor)

____

Prof. Dr. Alper Kiraz

____

Assoc. Prof. Onur Ferhanoğlu

____

Asst. Prof. Mehmet Cengiz Onbaşlı

____

Asst. Prof. Ahmet Can Erten

Date: 26.12.2019

ABSTRACT

Light Efficient and Foveated Head-Worn Displays

Mehmet Kıvanç Hedili

Doctor of Philosophy in Electrical and Electronics Engineering

December 26, 2019

Augmented reality (AR) displays in eyeglass form are seen as the future of information displays. The image generation unit within the AR glasses, which is called a spatial light modulator (SLM), and optical architectures are among the major limitations of current AR displays. For the ultimate AR experience, the viewer should see high resolution images that cover a large portion of their viewing angle. With the current SLM technology either large viewing angle with low resolution images or high resolution images with small viewing angle can be provided. This trade-off is one of the key limitations of AR glass technology.

Considering that the human eye has high resolution only at its central vision and the rest of the view gradually seems blurred towards the periphery, more efficient displays can be designed by mimicking the human eye. These architectures that show sharp images only to the central vision and low resolution images to the rest of the viewing angle are known as foveated displays in the literature.

Foveated displays require eye tracking and special optical architectures that can change the position of the high resolution image within the larger viewing angle of the user, depending on the user's viewing direction. In this thesis, we present three different

foveated AR glass architectures and a fast, reliable and computationally light pupil tracker algorithm that we developed for foveated display architectures.

In our pinhole display we extended the eyebox using an array of light sources (LEDs), which are individually turned-on based on the pupil position in real-time. We demonstrated a 37° circular field-of-view (FOV) with a luminance of 360 cd/m^2 using an LED with only 0.42 lumen output. We achieved an extended eyebox of 14x10 mm in size with 1 mm static eyebox per LED and the static eyeboxes are spaced 2 mm apart. The resulting display is super light-efficient as most of the LED light is captured by the eye. In our holographic display with rotating beam splitters, a static 7x4° instantaneous FOV is mechanically steered in sync with the rotations of the eye, so that the viewer always sees a high resolution image at the central vision. We demonstrated 37x4° extended FOV, which is the first holographic foveated head-worn display that works in closed-loop with a pupil tracker in the literature. In our eye-centric design, we eliminated the moving parts by imaging the SLM to the rotation center of the eye. With this architecture, the SLM automatically follows the central vision by design and the holographic image is projected on to fovea by updating the hologram on the SLM. We demonstrated 28x28° instantaneous FOV, which is extended to 60x40°.

ÖZET

Işığı Verimli Kullanan ve Foveated Gözlük Mimarileri
Mehmet Kıvanç Hedili
Elektrik ve Elektronik Mühendisliği, Doktora
26 Aralık 2019

Arttırılmış gerçeklik gözlükleri geleceğin ekran teknolojisi olarak görülmektedir. Arttırılmış gerçeklik gözlüklerine görüntü oluşturma görevi gören uzaysal ışık modülatörleri ve bunun yanısıra optik mimariler güncel gözlüklerin performansını kısıtlayan temel bileşenlerdir. Hayal edilen arttırılmış gerçeklik deneyimi için yüksek çözünürlüklü ve insan gözünün görüş açısının geniş bir kısmını kaplayan görüntüler oluşturulmalıdır. Günümüz teknolojisi ile geniş görüntü açısı ve düşük çözünürlüklü görüntü veya dar görüş açısı ve yüksek çözünürlüklü görüntü sağlanabilmektedir. Bu ödünleşme arttırılmış gerçeklik gözlüklerinin tasarımında temel sorunlardan birisidir.

İnsan gözünün yalnızca merkezi görüş açısında dar bir bölgeyi net ve yüksek çözünürlükte, geri kalan bölgeleri bulanık gördüğü düşünüldüğünde çok daha verimli ve insan gözüne benzer özellikte görüntü üreten optik sistemler üretilmesi mümkündür. Gözün net gördüğü bölgeye yüksek çözünürlüklü, geri kalan bölgelere düşük çözünürlüklü görünüler sağlayan sistemlere foveated display denilmektedir.

Foveated displayler gözün gerçek zamanlı takibini ve görüntüyü gözün başış açısı içinde uygun yere kaydırabilecek özel optik mimarilere ihtiyaç duymaktadır. Bu tezde bu işlevi yerine getirebilen üç farklı optik mimari anlatılmaktadır. Bunun yanı sıra hızlı ve güvenilir göz takip algoritmamız da anlatılmaktadır.

İğne deliği kamerası ilkesi ile çalışan AR gözlük mimarimizde, bu tekniğin doğası gereği tek nokta olan görüntü penceresi ışık kaynağı dizini kullanılarak genişletilmiştir. Işık dizinindeki her LED gözün gerçek zamanlı yerine bağlı olarak uygun şekilde açılmaktadır bu sayede görüntü penceresi genişletilmektedir. 37° görüş açısı olan ve yalnızca 0.42 lumenlik LED ile 360 cd/m^2 parlaklığında görüntü elde edilmiştir. Tek LED için 1mm olan görüntü penceresi 14x10 mm kadar genişletilmiştir. Gözlüğümüz iğne deliği kamerası ilkesi sayesinde ışığı çok verimli kullanarak parlak görüntüler oluşturmaktadır. Dönen yarı-ayna tabanlı holografik gözlük mimarimizde sabit olarak 7x4° görüş açısı sağlayabilen SLM'in sanal görüntüsü göz açısına bağlı olarak yarı-aynalar yardımıyla gezdirilmektedir. Bu sayede küçük açılı görüntü sürekli gözün önünde oluşarak daha büyük bir ekran etkisi yaratmaktadır. Bu teknik ile görüş açısı 37x4° ye çıkarılmıştır. Gözlüğümüz literatürde göz pozisyonun bağlı olarak geri beslemeli olarak çalıştırılan ilk foveated holografik gözlüktür. Bir diğer mimarimiz ise SLM'in gözün dönme merkezine optik olarak görüntülenmesi ile oluşturulmuştur. Bu sayede göz nereye bakarsa baksın otomatik olarak SLM'in görüntüsü gözde oluşmaktadır. Hiçbir hareketli parça içermeyen bu mimari SLM üstündeki hologramın değiştirilmesitle fovea üzerine yüksek çözünürlüklü görüntü oluşturmaktadır. Oluşturulan görüntü tek bir bakış açısı için 28x28° görüş açısına sahip olup, gözün hareketleri 60x40° lik bir aralıkta otomatik olarak takip edilmektedir.

ACKNOWLEDGEMENT

First and foremost, I would like to express my gratitude to my advisor Prof. Hakan Ürey for his support, guidance, encouragement and patience throughout my PhD studies. His enthusiasm and limitless energy for his research was a great motivation for me. It was a privilege to work with him, and more importantly the knowledge and experience that I gained from him is beyond this thesis work.

I would also like to thank to my thesis defense committee members, Prof. Onur Ferhanoğlu, Prof. Mehmet Cengiz Onbaşlı, Prof. Alper Kiraz and Prof. Ahmet Can Erten, for accepting to participate and for giving their valuable time and support.

It would have been impossible to complete my studies without the help of my colleagues and good friends at OML. I would like to thank all of them but especially to Dr. Erdem Ulusoy, Burak Soner and Ali Cem for their technical and intellectual assistance and their direct contributions to my research.

Last but not least, I am deeply grateful to my family for doubtlessly believing in me. I would not be able to complete this thesis without the support of my family to whom I dedicate it.

Table of Contents

LIST OF FIGURES

1 INTRODUCTION

1.1 Head-Worn Displays Overview

Displays have been an indispensable part of our modern lives as the major tool for information delivery. Spending long times in front of our displays is a global epidemic, causing all sorts of health problems due to reduced physical activity. The display technology as we know it has become saturated, providing larger, brighter displays with pixel sizes so small that their resolution matches our retinal resolution. In the last 10 years or so, wearable Augmented Reality (AR) displays gained popularity as it is seen as the next generation of displays; liberating people from their desks, revolutionizing information delivery paradigms and empowering new ways of interaction with our surrounding.

A single human eye has about 180° FOV. The central 10° region provides the highest resolution, which is called fovea on the retina. This region provides the sharp central vision and the resolution degrades towards the periphery, which is called the peripheral vision. Head-mounted displays should cover the FOV of the eye as much as possible without compromising the display resolution to provide comfortable experience to the viewer. With today's technology large FOV-high resolution head-worn displays require bulky optics and display technology is deficient.

There are many different technologies for AR glasses. Convention optical systems, waveguides, free-form optics, light-field displays and holographic displays are the major architectures used in recent head-worn displays. Today, waveguide based AR glasses dominate the market. Lumus and Epson Moverio are some of the most successful examples [1], [2]. A microdisplay that is coupled to a waveguide relays the image to the eye with some refractive power as illustrated in Figure 1.1a and Figure 1.1b. Lumus has 55° FOV and Moverio BT-300 has 23° FOV [4], [5].

Figure 1.1. a)An illustration of waveguide display of Lumus [1]. b) Epson Moverio BT-300 [2]. c) Microsoft Hololens [6]. d) Google Glass [7]. e) and f) MiraPrism [8],[9].

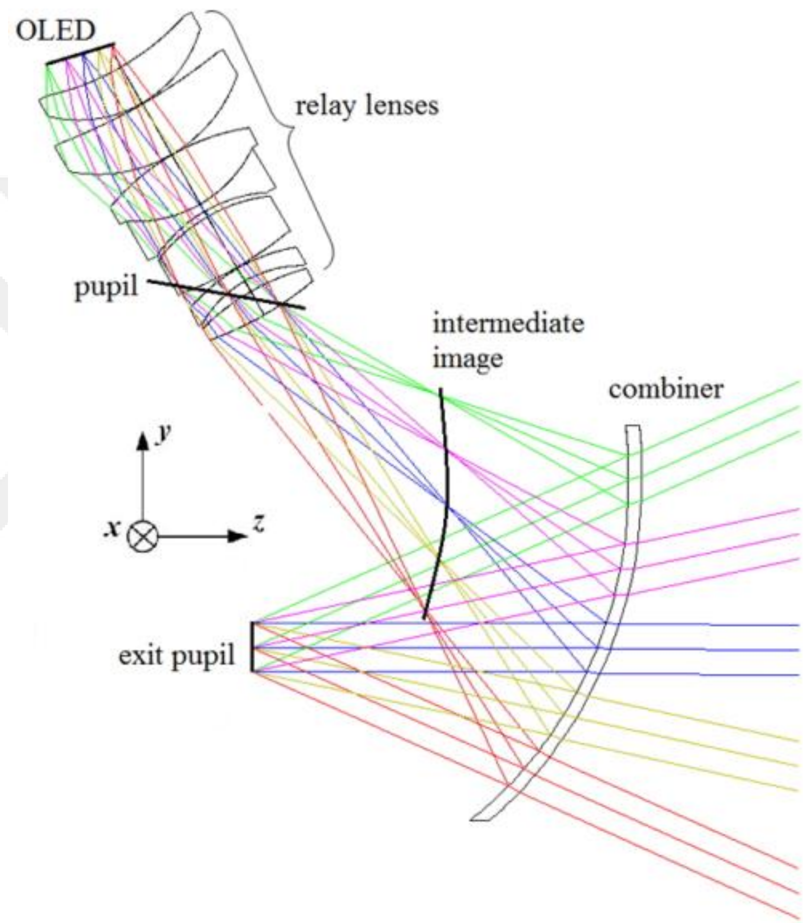

Figure 1.2. An example of a head-worn display using conventional optics. It has 40x30° FOV with 15mm eyebox [6] [11].

Conventional optical designs are also available in the literature. A microdisplay (OLED or LCOS) is magnified using refractive spherical lenses and an intermediate image plane is created as seen in Figure 1.2. A semi-reflective combiner relays this intermediate image plane to the eye. The maximum FOV that can be achieved by conventional optics is about

40° [10], [11]. Conventional optic size and weight grows rapidly with increasing FOV, therefore they are not regarded as the future of head-worn displays. An example of an aggressive design to achieve large FOV can be seen in Figure 1.3. 16 different pieces of lenses, including two ellipsoid mirrors are utilized to provide 120x120° FOV and 6mm eyebox [33]. Such systems are bulky, heavy and expensive, which prohibits their commercial use.

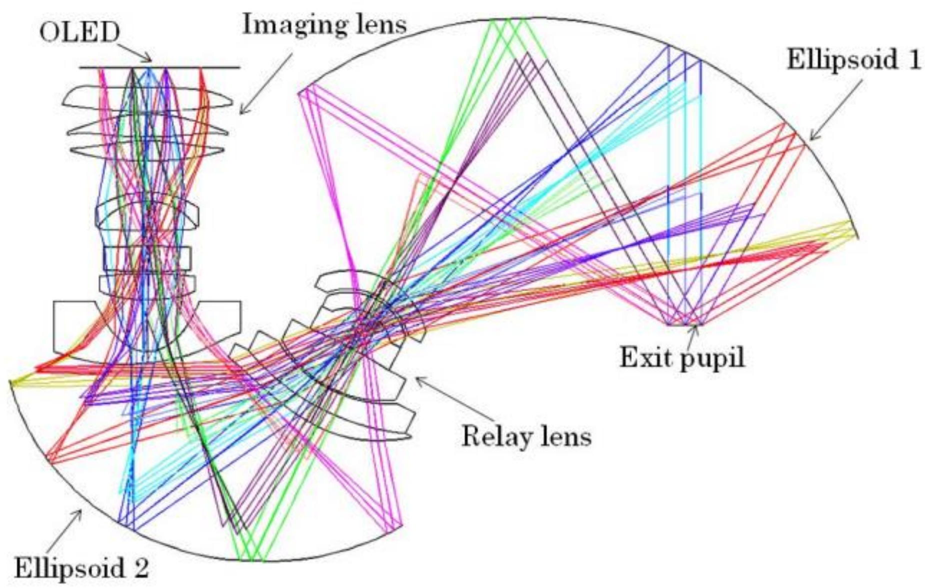

Figure 1.3. A low-distortion head-worn display design that provides 120x120° FOV with 6mm eyebox [33].

Figure 1.4. Implementation of a wide FOV display using conventional optics [13].

A third alternative method is using free-form optics. As seen in Figure 1.5, free-form prisms that work in reflective or catadioptric modes are available in the literature [12], [52]. In these prisms each surface has some optical power and the overall system can provide about 30x40° FOV with 4mm eyebox. Since the free-form prisms are compact, multiple components are tiled to provide larger FOV [54]-[56].

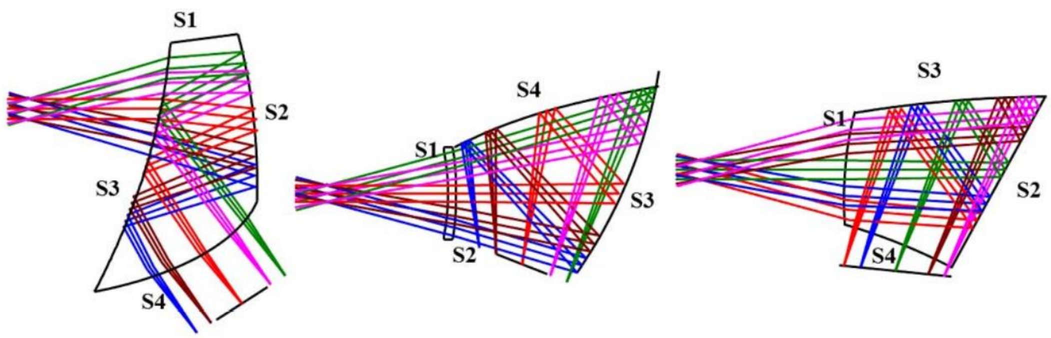

Figure 1.5. Free-form prisms can provide compact solutions. They can provide 40x30° FOV with 4mm eyebox [12], [52].

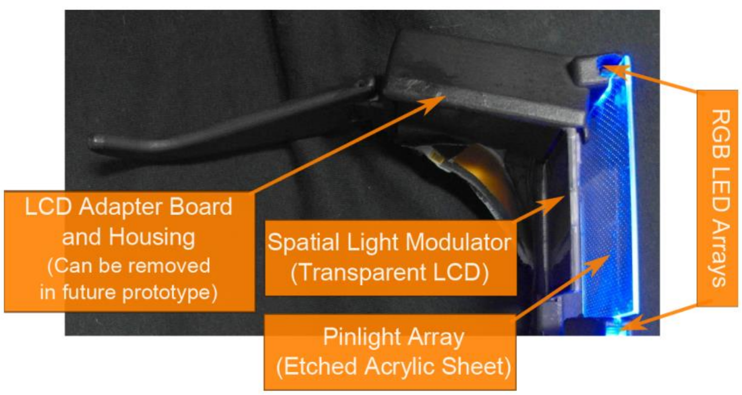

Figure 1.6. The experimental setup for pinlight diplay [14].

Pinlight displays provide large FOV (110°) with a very simple architecture. The display does not need any lenses or components with optical power, therefore they are very light and simple. The LCD is illuminated by an array of pinlights such that the image on the LCD becomes visible due to large depth of field [14]. As seen in Figure 1.7 a sharp image is produced without any optical refractive power components. The main disadvantage is low brightness.

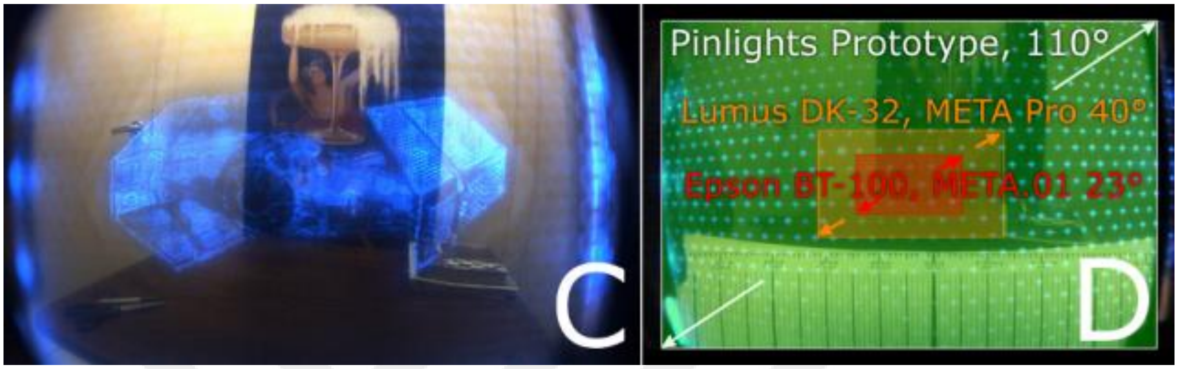

Figure 1.7. The image produced by the pinlight display [14].

1.2 Microdisplays for AR Head-Worn Displays

All head-worn displays require a small image generator, which is known as a microdisplay. Liquid Crystal on Silicon (LCOS), Organic Light Emitting Diode (OLED), Digital Micromirror Device (DMD) and pico-projectors are the preferred technologies for their small size and high pixel numbers.

As the name suggest LCOS displays consist of a liquid crystal on reflective silicon electronics that modulate the incident light in an analog fashion by rotating the liquid crystal by the applied voltage. The structure of LCOS displays can be seen in Figure 1.8. The advantages of LCOS displays are they can provide ultra-high brightness with good contrast (2000:1), high percentage of the incident light reflects back (70-80%) and they can modulate amplitude, phase or the polarization of the incident light, making them suitable for holographic displays [15].

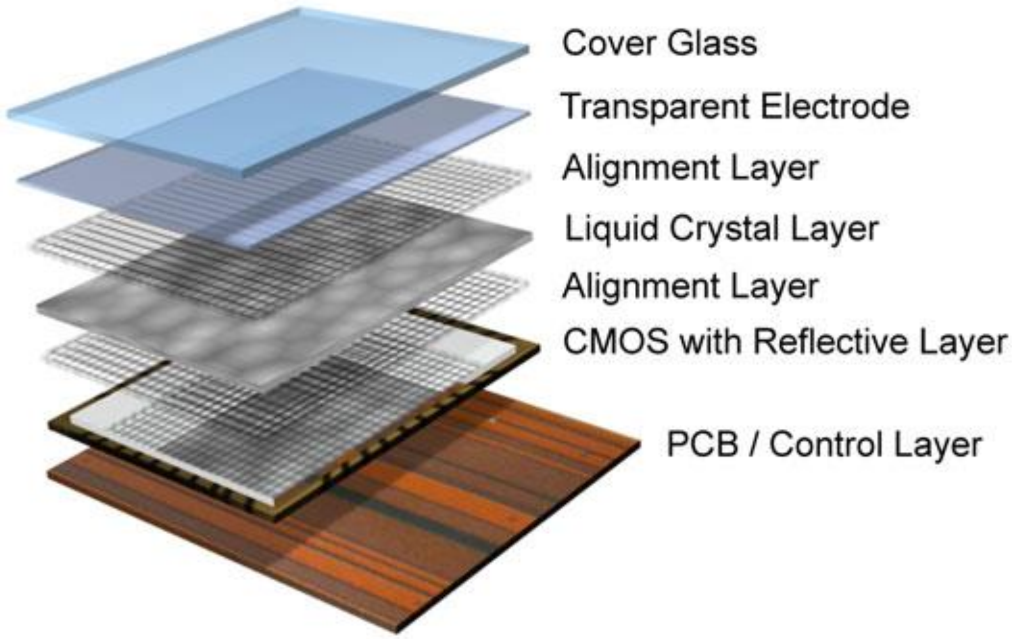

Figure 1.8. The cross-sectional view of an LCOS display [16].

As the LCOS chips are work in reflective mode, an external illumination that consists of three main colors (red, green, blue) must be used. The light source can be LEDs or lasers depending on the application. In its typical application three main colors are conditioned and combined into a single beam using dichroic mirrors, which is reflected towards the LCOS chip using a beam splitter. RGB light sources are turned-on time sequentially to provide full color images. The modulated light is reflected back and projected out using additional optical components as illustrated in Figure 1.10.

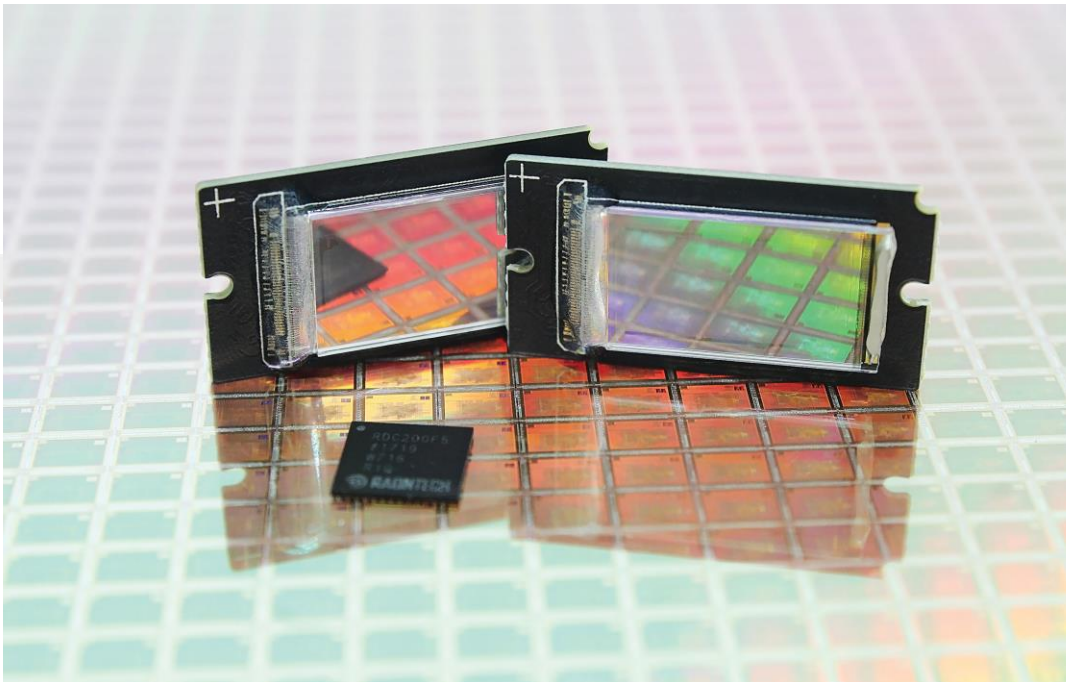

Figure 1.9. An example of an LCOS microdisplay [17].

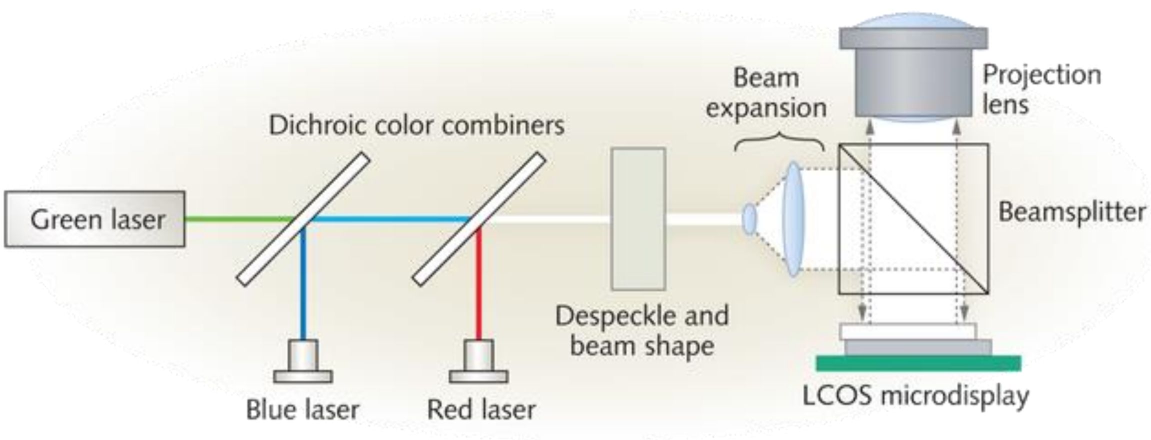

Figure 1.10. Typical optical setup for color displays using LCOS [18].

A similar alternative to LCOS displays is the Digital Micromirror Device (DMD) as seen in Figure 1.12. DMD chips consist of millions of micromirrors that can tilt to two binary positions. Each micromirror is a pixel of the display that can have two digital positions: if the pixel is on, the mirror is tilted in one direction reflecting the light out; if it is off the mirror tilts in the other direction, reflecting the light to an absorber as shown in Figure 1.11. Typical pixel size is about 5μm and the mirrors tilt about ±10° depending on the chip model. The analog pixel values are displayed by pulse with modulation by rapidly switching the mirrors. DMDs also require external light sources that are triggered time sequentially to display full color image.

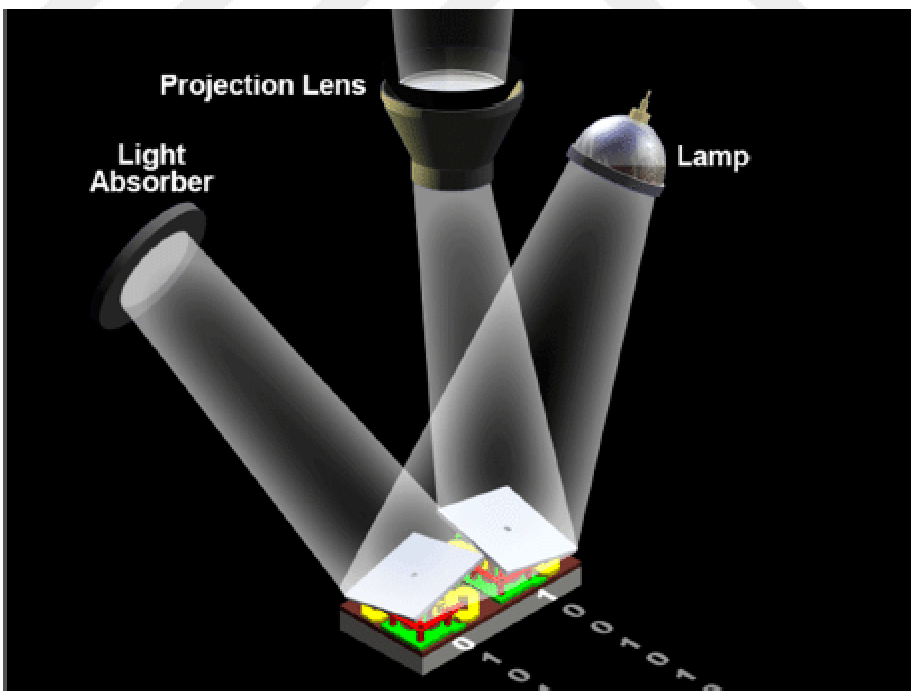

Figure 1.11. DMD pixels in on and off states [19].

Figure 1.12. An photograph of a DMD chip [20].

OLED microdisplays consist of organic LEDs as pixels, which are self-emissive. This means they do not need external light sources and eliminate relatively complicated illumination optics. This reduces the number of components (hence the weight) and occupies less space on the head, which is a major advantage compared to LCOS and DMD displays for head-worn displays. As the off pixels do not emit any light their contrast is excellent (100.000:1) and they have very fast response time (<0.01ms) [22]. Similar to DMDs, OLED displays can only have amplitude modulation.

Figure 1.13. A OLED microdisplay [21].

Laser scanning pico-projectors can also be used in head-worn displays, either as an image source that projects at an intermediate image plane or directly to the retina. They provide low-power and miniaturized solutions thanks to MEMS technology and provide bright images with great color saturation.

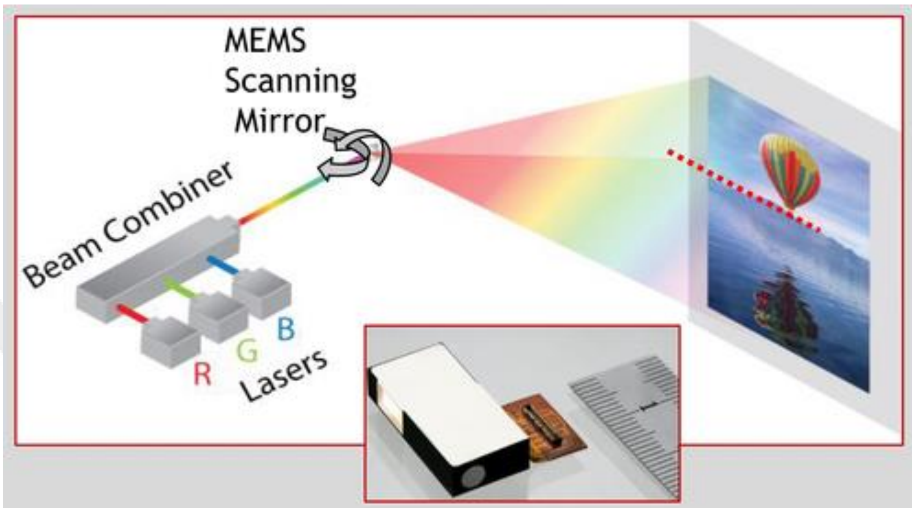

Figure 1.14. Laser scanning pico-projector [23].

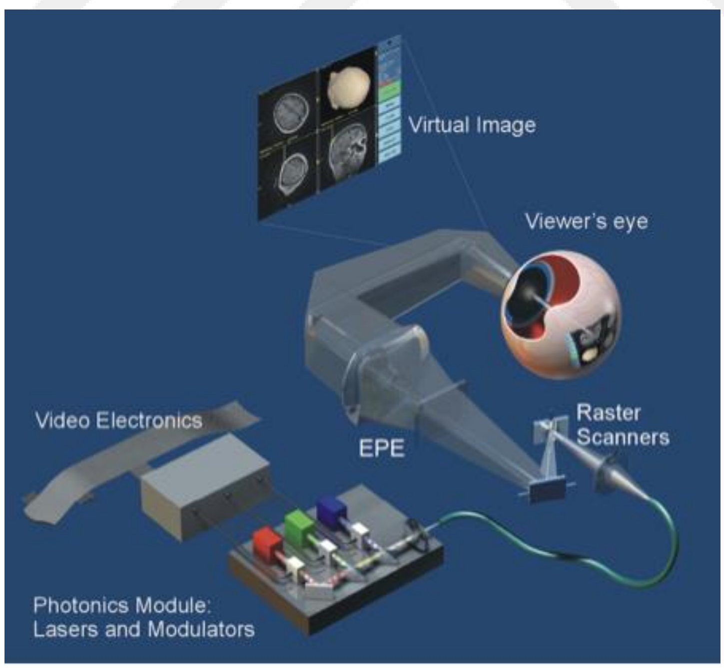

Figure 1.15 Microvision's laser pico-projector used in a retinal scanning display [24].

1.3 Holographic Head-Worn Displays

Holographic head-worn display is the ultimate technology that can offer true 3D. Holography creates images by the interference of the pattern written on the SLM, each pixel introduces some phase shift and the total interference pattern of all the pixels on the display produces the image at the required depth. Interference requires coherent illumination; therefore LEDs or lasers are used as the light source. This means OLED displays are not suitable in holographic displays because individual pixels emit light, which is not coherent. Typically LCOS chips that modulate the phase of the illumination are used.

Holography eliminates the accommodation-vergence conflict by providing a single binocular vision with correct depth cues, providing a comfortable augmented/mixed reality experience. Figure 1.16 illustrates the holographic head-worn display dream. A transparent SLM is illuminated by a point source (RGB LEDs) and a hologram that is calculated for the desired 3D virtual scene is displayed on the SLM. When the hologram is illuminated the observer sees the virtual objects in the 3D scene along with the real world objects. The SLM has large FOV and large eyebox.

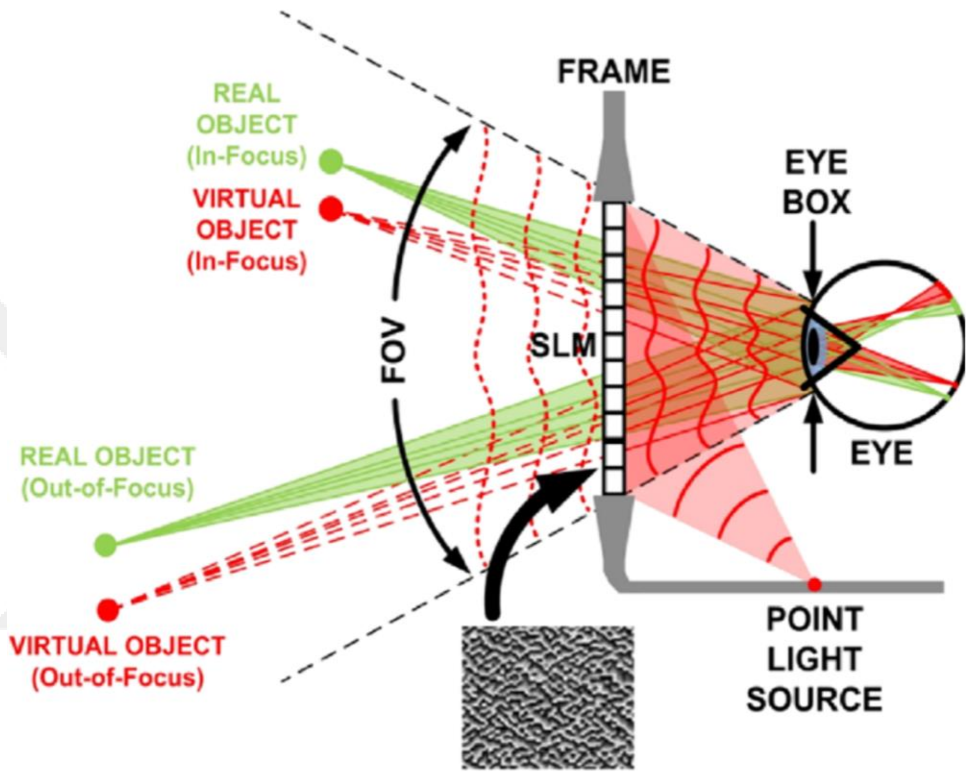

Figure 1.16. The holographic head-worn display concept. The hologram on the SLM creates virtual objects to the eye [68].

Currently, the real implementations of this concept are far from this dream. As the SLM sizes are small the typical achievable FOV is about 10°, which is very small compared to the human visual system. The large pixel size means the eyebox size is small, which means correct alignment with the display is difficult and handling the rotation of the eye is problematic. Large pixel size also means that the SLM does not have high optical bandwidth to bend the rays from side of the eyeglass frame towards the eye, as shown in Figure 1.16; therefore additional lens systems are needed to bend and focus the rays, which means AR glasses with sleek designs is not possible in the near future. Placing the SLM in front of the eye is also challenging due to low transparency of SLMs and their diffraction grating effects, which separate the color of the objects seen through it and create multiple replica images of them. Calculating the appropriate holograms is another challenge. Storing and rendering a 3D model of the virtual objects is computationally demanding and iterative hologram computation algorithms take too long time to display real-time holographic images.

4f-Fourier filtering is commonly used to remove the unwanted diffraction orders of the illumination beam and the replicas of the eyebox, as shown in Figure 1.17. The SLM is typically illuminated by collimated light and gets focused by a Fourier lens. The focused image is filtered with a band-pass filter that is placed at the Fourier plane, which blocks all the light except the eyebox. The filtered image is converted to real domain by a secondary Fourier lens and the light is focused to the pupil plane by an eyepiece lens.

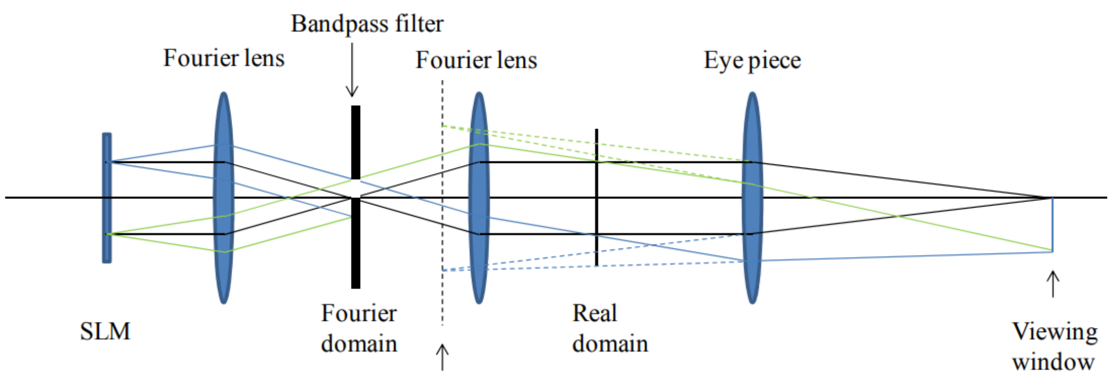

Figure 1.17. 4f-Fourier filtering the diffraction orders [24].

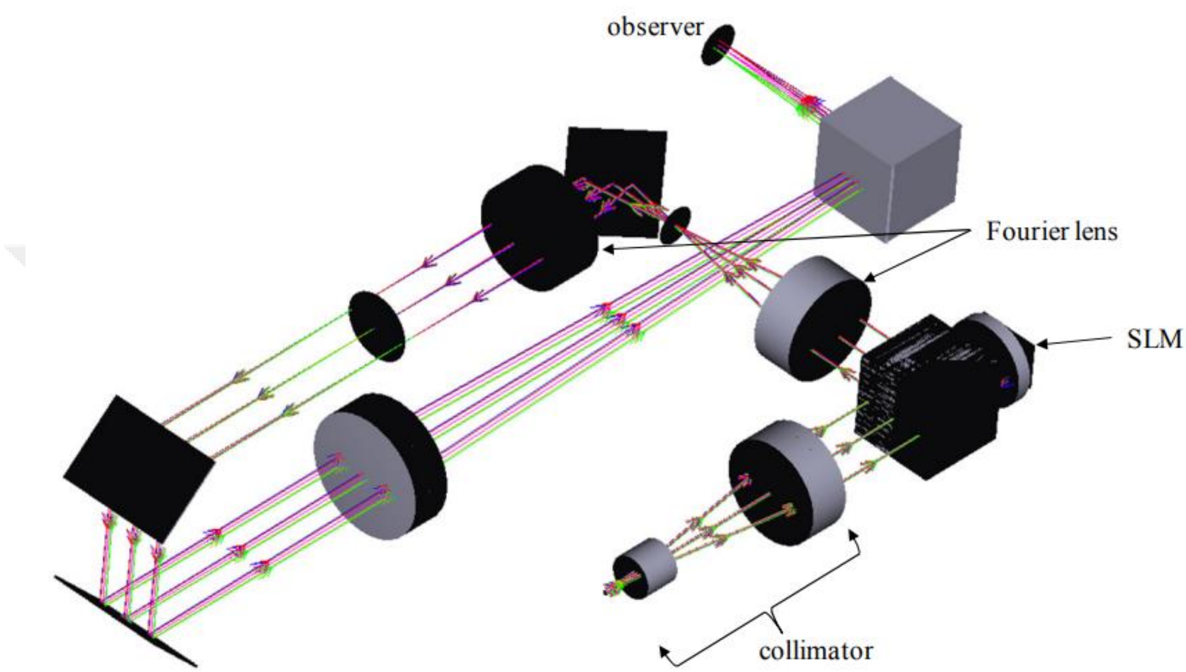

Figure 1.18. An holographic head-worn display design with 4f-Fourier filtering [24].

There are various implementations of the holographic head-worn displays in the literature. Figure 1.18 shows an implementation of holographic display with 4f-Fourier filtering [24]. RGB LEDs are coupled to an optical fiber. The SLM is illuminated by the collimated fiber output and the modulated light is fed into a 4f system using a beam splitter. The filtered image is relayed to the eye using folding mirrors and focused by a lens. The experimental holographic images for RGB wavelengths can be seen in Figure 1.19.

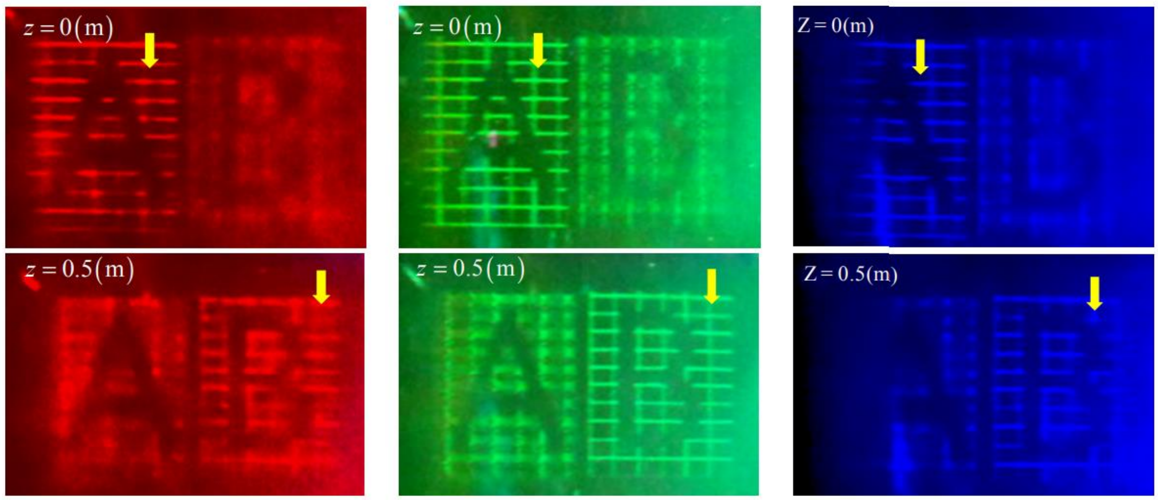

Figure 1.19. Experimental holographic images for RGB colors [24].

As illustrated in Figure 1.20, an alternative to 4f filtering is using the eye pupil as the filter itself [26]. In this implementation the SLM is illuminated by a diverging beam. The reflected light is focused to the pupil to create the Fourier plane. The eye pupil filters out the diffraction orders and the eyebox replicas. 61.9° FOV is demonstrated but at the cost of only having a 1mm eyebox. The small eyebox means the ability to display depth is hindered due to high depth of field. A monochrome experimental holographic image is seen in Figure 1.21. Since the diffraction orders are very close to each other, the zeroth order of the illumination beam leaks into eyebox, which reduces the contrast of the holographic image.

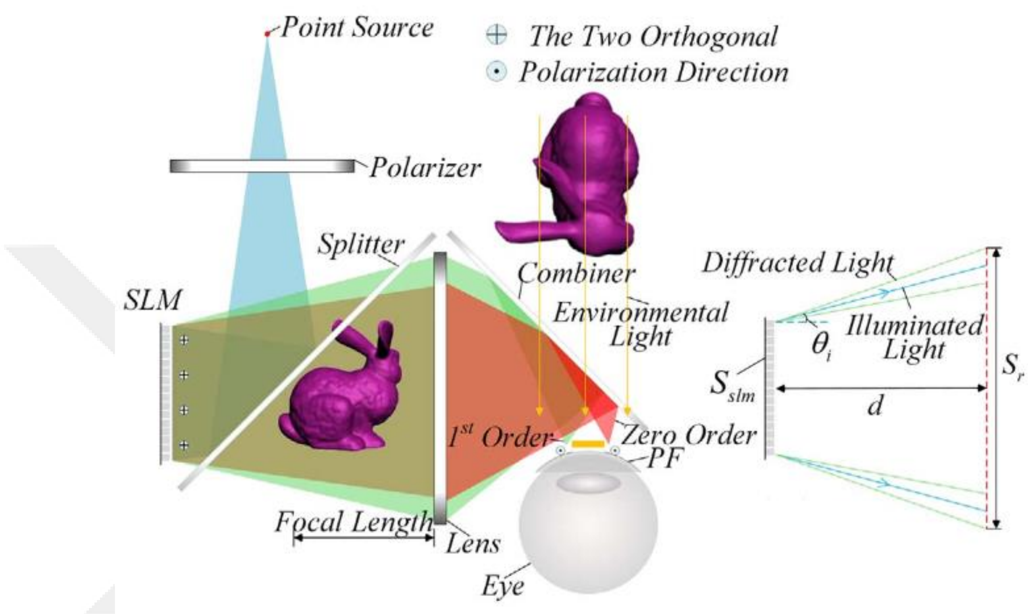

Figure 1.20. Holographic setup with pupil filtering. The FOV is 61.9° and the eyebox size is 1mm [26].

Figure 1.21. The holographic image with the pupil filter [26].

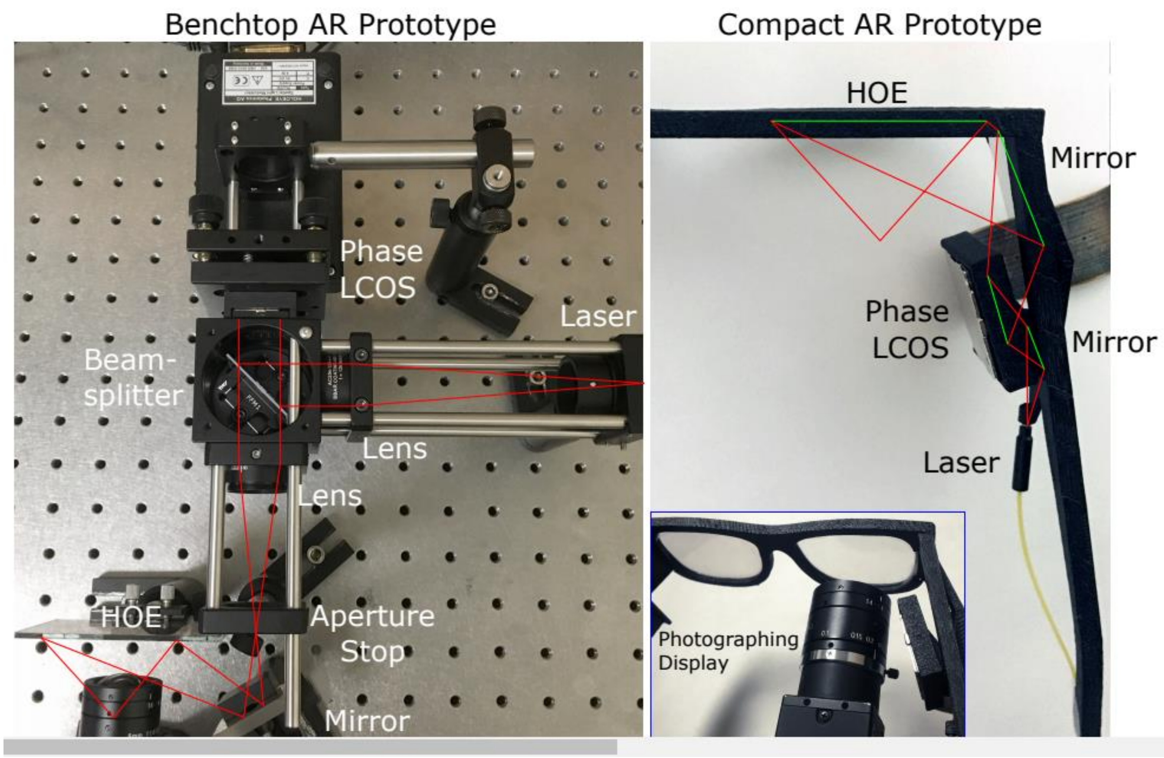

Figure 1.22. The holographic AR head-worn display using a holographic optical element as the combiner surface [76].

Microsoft Research demonstrated their holographic AR glasses as seen in Figure 1.22 [76]. On the left the system on the optical bench is shown. A collimated laser beam illuminates the LCOS SLM and the reflected light is focused and filtered at the aperture stop. The light passing through the aperture stop is relayed and focused by the help of a mirror and an holographic optical element (HOE). On the right image the AR display with a compact eyeglass format is shown. In this prototype the RGB laser light is fed into the optical system using an optical fiber and the fiber output directly illuminates the SLM with a diverging beam. With the help of a mirror the modulated beam is relayed on the HOE, which focuses the incident light to the eye pupil plane. The system is built highly off- axis for a compact architecture. In the prototype Holoeye Pluto is used as the SLM (1920x1080 pixels with 8μm pixel pitch). The optical system provides 80° FOV but suffers from small eyebox size. Figure 1.23 shows the full color experimental holographic image.

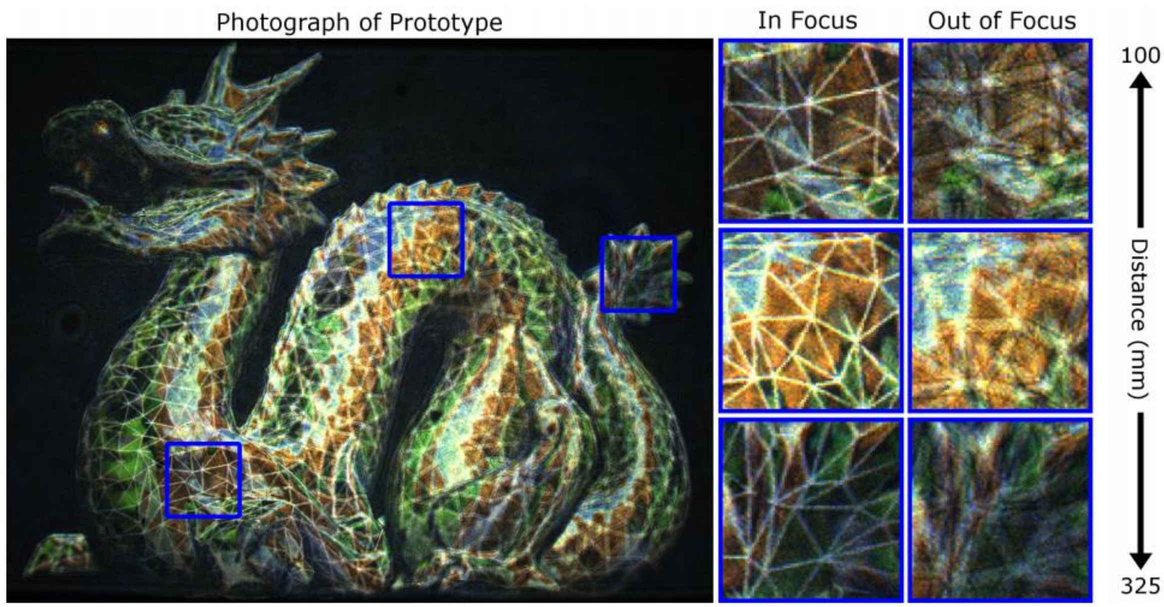

Figure 1.23 The holographic image acquired by the camera [76].

Kazempourradi et. al. demonstrated various holographic head-worn display architectures that illuminates the SLM with converging and diverging beams [68]. Speckle reduction and full color demonstration at multiple depths have been demonstrated as seen in Figure 1.24 to Figure 1.26.

Figure 1.24. Holographic display with 4x4mm eyebox size and 16.7° FOV [68].

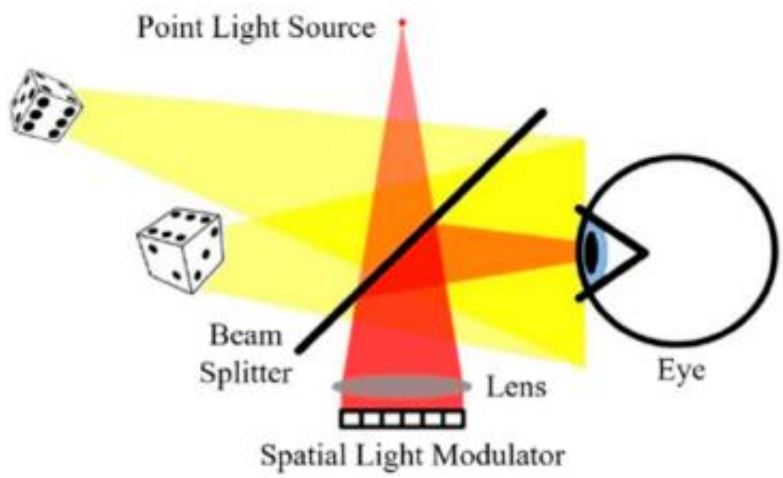

Figure 1.25. The experimental setup for Figure 1.24 [68].

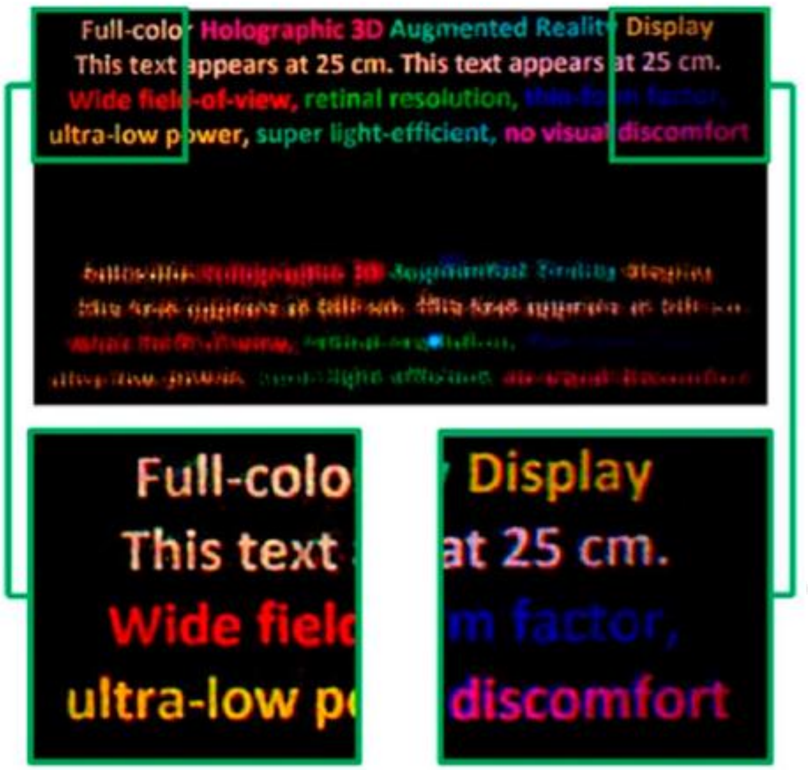

Figure 1.26. Full color holographic demonstration with two depths [68].

1.4 SLM Space-Bandwidth Product Limitations

In essence near-eye displays relay a magnified image of the image source (i.e. a microdisplay) to the field-of-view (FOV) of the user. To achieve high resolution, the pixel size of the microdisplay should be small. Considering the typical pixel size is about 5μm, a full HD microdisplay is roughly 10x5mm in size, which is quite small. To provide large FOV with such a small microdisplay, large magnification optics is required, which means the apparent pixel size is increased, hence the maximum spatial resolution that can be displayed is reduced, as illustrated in Figure 1.27. This phenomenon is known as the resolution-FOV invariant [3].

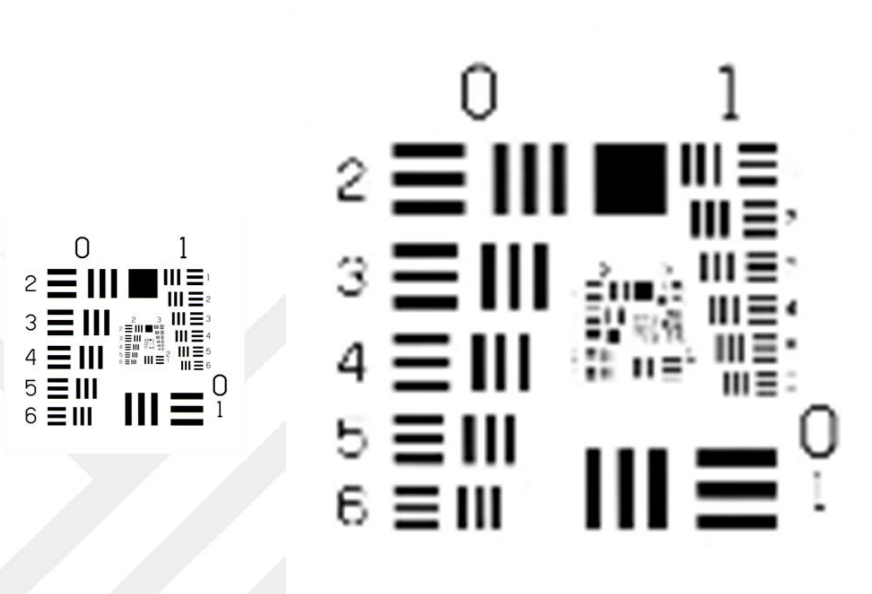

Figure 1.27. Resolution-FOV invariant. For a given microdisplay the resolution decreases with increased magnification.

With holographic displays the image is created by the interference of pixels, therefore the SLM pixel size does not directly correlate with the pixel size of the displayed image. As illustrated in Figure 1.16, the SLM synthesizes the wavefront from the input wave, as if it is coming from a real object at a certain distance from the viewer. Therefore to increase the FOV the eye can be placed closer to the SLM and the SLM would generate the wavefront for that eye position. The problem is that as the eye gets closer to the SLM the diffraction order spot size grows, reducing the eyebox size, as shown in the Zemax simulations in Figure 1.28. Therefore in holographic displays the resolution-FOV invariant transforms in to what is known as the space-bandwidth product of the SLM.

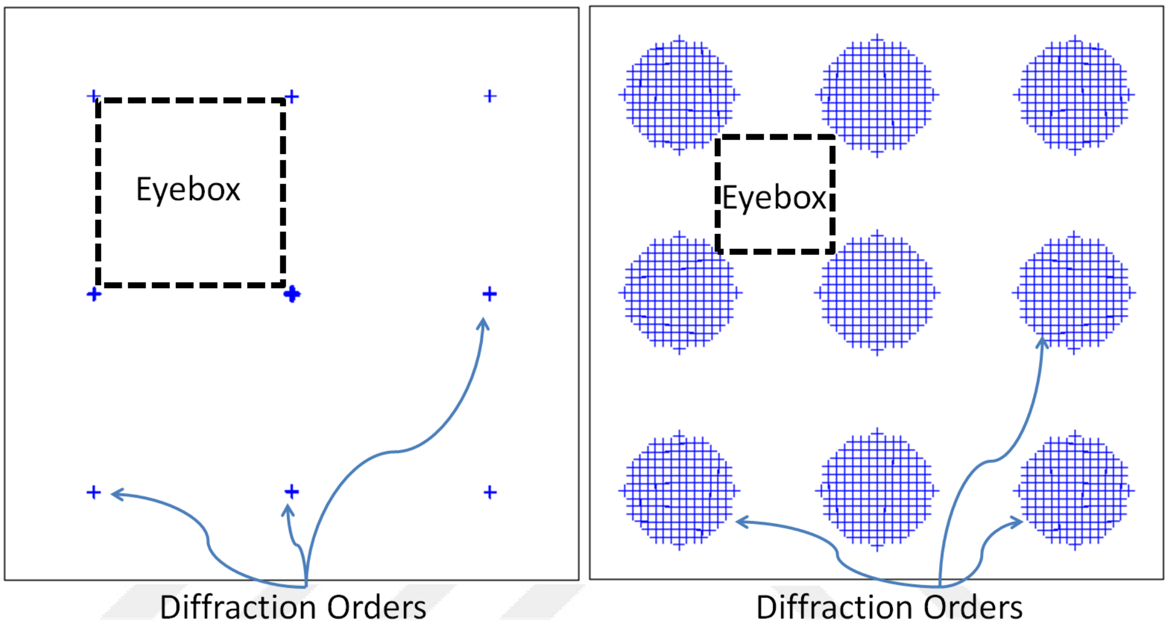

Figure 1.28. On the left the eyebox is large when the pupil is at the focus plane. On the right the pupil is placed closer to the SLM. The eyebox size is reduced due to increased spot size of the diffraction orders.

The space-bandwidth product is the product of the bandwidth and the size of the display. If we think in one dimension, the size of the SLM is $N.\Lambda$, where N is the number of pixels and Λ is the pixel pitch. Bandwidth of the SLM is equal to λ/Λ, where λ is the illumination wavelength. In the space-bandwidth multiplication the pixel pitch Λ cancel out and it is equal to $\lambda.N$, which means the space-bandwidth product depends on the number of pixels for a given wavelength.

Currently typical pixel size for LCOS SLMs on the market is in the range of 8µm to 3.74µm and resolutions vary from full HD to 4K [27]. Holoeye GAEA-2 has the highest performance figures, combining 3.74µm pixel pitch with 4K (4160x2464 pixels) resolution

[28]. As described above, the number of pixels in an SLM determines a constant space-bandwidth product, which means the product of FOV and eyebox is a constant for a given SLM. For GAEA the space-bandwidth product is about 100 deg.mm in the horizontal direction. This means the holographic display can have 10° FOV with 10mm eyebox or 50° FOV with 2mm eyebox.

For comfortable operation large FOV with large eyebox is desired. Large FOV is necessary to provide ability to address a greater portion of the perceived view. Large eyebox is necessary for easy alignment of the eye with the display. Large eyebox is also necessary to achieve sufficiently small depth of field to provide depth information. With small eyebox displays the depth of field becomes large and objects at all depths appear sharp, impairing the ability to provide correct focus blur.

1.5 Foveated Displays

The receptor cell distribution in the human retina is spatially non-uniform. The highest density is in the region called fovea and it sharply decreases towards the periphery, as shown in Figure 1.29 [60]. Fovea is the region on the retina that is responsible for our central vision, which has an angular extend of about 10°. The non-uniform distribution of sensory cells means that the perceived image at the central vision is sharp whereas the peripheral vision is blurred as seen in Figure 1.30.

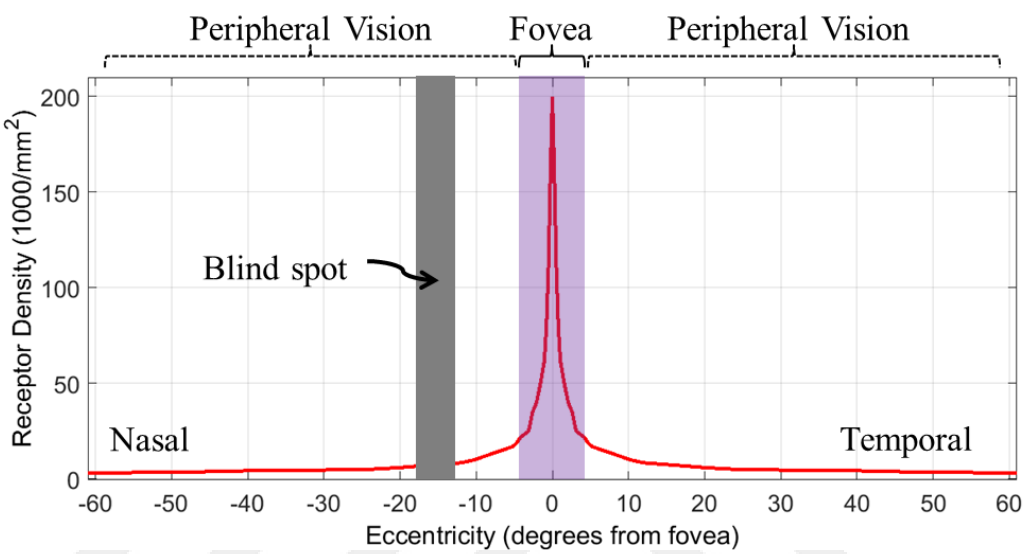

Figure 1.29. The distribution of receptor cells in the retina. The cell density hence the visual acuity drops rapidly outside the fovea.

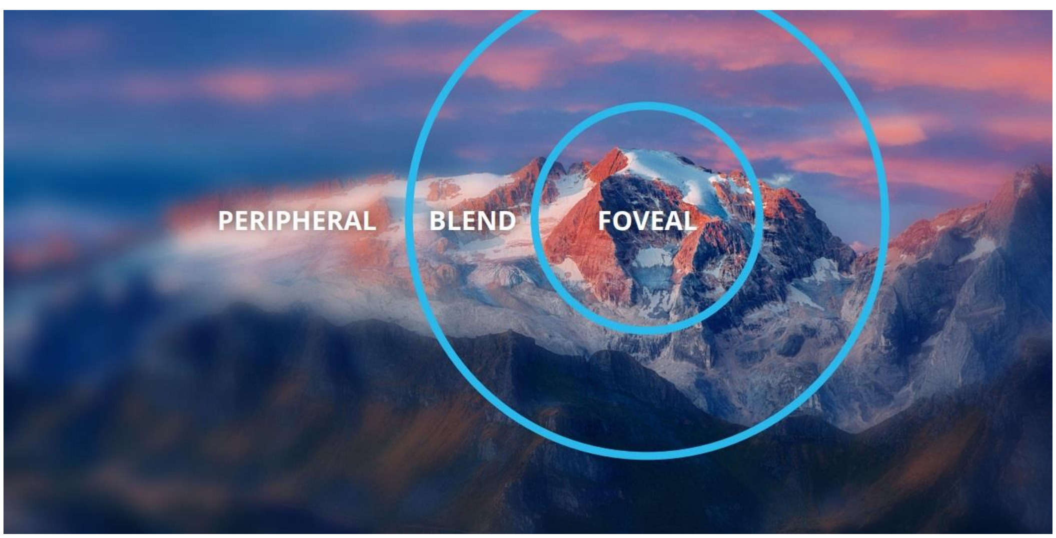

Figure 1.30. Foveated image with high resolution image at the center and low resolution at the periphery. [29].

Considering that only a small portion of our FOV (10°) is seen sharp and the rest of it is seen blurred, providing high resolution images to the entire retina is wasteful. Display architectures that exploit this feature of the human eye are called foveated displays [59]. Foveated displays show a high resolution image only to the fovea region and the peripheral vision is provided by a large pixel, low resolution display. The rotations of the eye must be measured in real-time by a pupil tracker and the high resolution inset should be shifted using a closed-loop system within the low resolution peripheral image, such that it falls on to the fovea at all times. Shifting the high resolution content requires the physical movement of either the SLM itself or some other optical components that shift the virtual image of the SLM [63].

Although foveated displays are complex systems, currently they are the only option to overcome the space-bandwidth limitation of the SLMs.

1.6 Contributions of the Thesis

Currently the space-bandwidth product of SLMs is small for head-worn display applications and it will not change dramatically in the foreseeable future. Therefore, to develop large FOV and large eyebox displays with the limited SLMs, novel optical architectures exploiting additional technologies is required. In this thesis we present three different foveated head-worn display architectures that overcome eyebox and FOV limitations of current SLMs.

The diagram in Figure 1.31 shows the basic building blocks of the head-worn display architectures that are presented in this thesis. In all of our solutions the pupil tracker is at the heart of our systems. The pupil position is monitored continuously in real-time to be able to provide the high resolution image to the fovea and to turn-on appropriate LEDs to extend the eyebox. We developed our fast and efficient algorithm that works real-time on computers with limited resources such as BeagleBone Black. In Chapter 2 the details of the algorithm is presented along with the experimental measurements of its accuracy and repeatability.

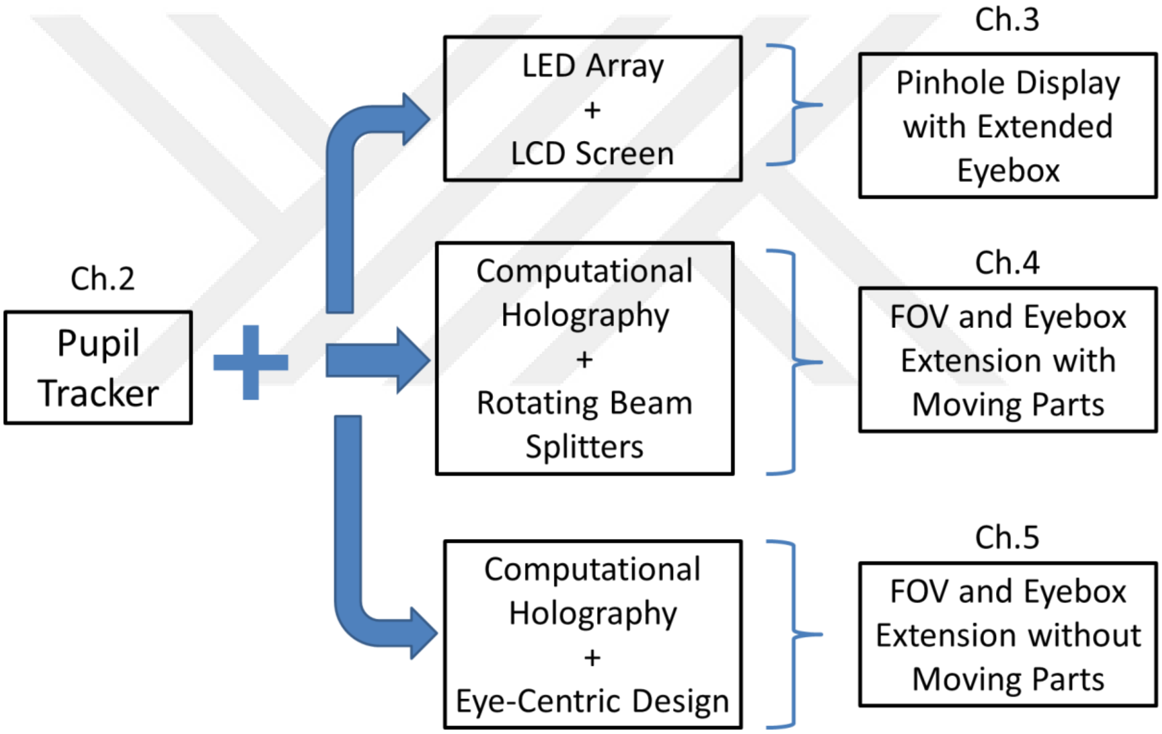

Figure 1.31. Diagram of the foveated display architectures presented in this thesis.

In Chapter 3 we present an architecture using an LCD and LED array backlight to achieve pinhole imaging principle. In our pinhole display the light source is focused to the eye pupil, which creates an eyebox 1mm in size and presents an image that is always in focus. Considering the eye pupil is about 3mm in diameter, with just 1.5mm rotation of the pupil the light gets blocked by the iris, so the image is lost. We solved the problem by using an LED array that can create multiple eyeboxes 1mm in size within a 14x10 mm area with 2mm spacing. This means for all positions of the pupil an LED can be turned-on. The LED array works in sync with the pupil tracker so that a continuous experience is provided to the viewer.

In Chapter 4, we present our foveated holographic head-worn display with rotating beam splitters, which is one of our solutions to the limited space-bandwidth product of SLMs. The SLM is relayed to the eye using two bean splitters that shift the virtual image of the SLM as they rotate. The controller receives the pupil position from our pupil tracker software and based on our optical simulations it rotates the two beam splitters, such that the holographic image always follows the central vision of the eye, perpendicular to the viewing direction. The SLM we used can only provide a static 7x4° FOV but using our rotating beam splitters approach we achieved 37x4° extended FOV. So far this is the only holographic foveated head-worn display in the literature that is demonstrated with a pupil tracker as a closed-loop system.

In Chapter 5, we present our foveated holographic head-worn display, which does not need any moving parts. Our patented optical architecture, which we call the eye-centric design, images the center of the SLM to the rotation center of the eye. This means the SLM is automatically aligned with the central vision of the viewer without any moving parts. The hologram on the SLM is updated based on the pupil position so that the holographic image is created on the fovea. We implemented the eye-centric design using a section of a custom designed and fabricated ellipsoid and we achieved 28x28° instantaneous FOV and 60x40° extended FOV using a Holoeye GAEA-2 SLM. This is the first demonstration of a holographic foveated head-worn display without any moving parts in the literature.

2 PUPIL TRACKING

2.1 Introduction

All of our optical architectures in the following sections utilize the pupil position information of the user to overcome some of the limitations of the SLMs, such as the limited eyebox size or small FOV that can be provided by the SLM. Furthermore, pupil position data is crucial to update the displayed image or computer generated hologram on the SLM. Therefore, the pupil tracker algorithm plays an important role in our display technologies.

By its nature the eye pupil has rapid and random movements. For our applications the algorithm must run fast and accurate enough so that our displays run as intended with no perceived delay by the user. The delay is especially important with our pinhole display because the human eye is very sensitive to blinking light, predominantly at the peripheral vision. Smallest time delay between switching light sources is perceivable and distracting.

Switching light sources in real-time is not possible with algorithms that are running on Linux or Windows computers. The algorithm running on those machines might be calculating the pupil location vary fast but communicating that data to outside world to do something (i.e. switch a light source) in real-time is not possible. There is a random delay of up to 100ms, which varies with the operation system load, in communicating the pupil location with an external microcontroller over the serial port. To overcome this problem we used a BeagleBone Black, which has a special processor architecture that incorporates a microprocessor with two programmable real-time units (PRUs) on the same memory space. This architecture enables us to run the pupil tracking algorithm on the Linux space and do the outside world things using the PRUs in real time.

Majority of the algorithms in the literature are based on image processing of the acquired pupil images under IR illumination [98]. *Swirsky et al*. developed an algorithm that detects the coarse pupil location with Haar-like feature detector, performs k-means clustering to refine the data and finally fits an ellipse to detect the pupil [99]. *Iannizzotto et. al* demonstrate pupil detection using circular Hough transform [100]. *Wood et al.* and *Başak et. al* also demonstrate their pupil tracker algorithms based on fitting ellipse to the pupil using least-squares [101], [102]. *Kumar et. al.* developed an algorithm which consists of a series of complex filtering operations like Radial Symmetry Detection, edge detection, glint removal, Delaunay Triangulation and ellipse fitting to find the pupil position [102]. *Lee et. al.* developed an algorithm that computes the gaze based on analyzing the Purkinje images, which are the specular reflections of the surrounding from different layers of the eye structure [104].

2.2 Thresholded Center-of-Mass Based Pupil Tracker Algorithm

In this research we developed an algorithm based on thresholded center of mass. The problem with BeagleBone Black is that it is primarily a pocket computer with very limited microprocessor resources to run relatively complex image processing algorithms. Most of the pupil tracker algorithms in the literature are too heavy to run on BeagleBone Black. To overcome this problem, we implemented a simple algorithm using Python programming language which calculates the pupil position in about 1ms for VGA resolution images. Later on we implemented this algorithm in C programming language, which successfully runs on BeagleBone Black.

The tracker setup requires an IR illumination LED and a modified camera with its IR blocker filter replaced with a visible blocker filter. The position of the IR illumination LED is adjusted such that its reflection from the cornea appears roughly at the pupil position as seen in Figure 2.1. For eye safety reasons the energy at the eye plane due to IR illumination LED should be less than 100 W/m^2 [105], [106].

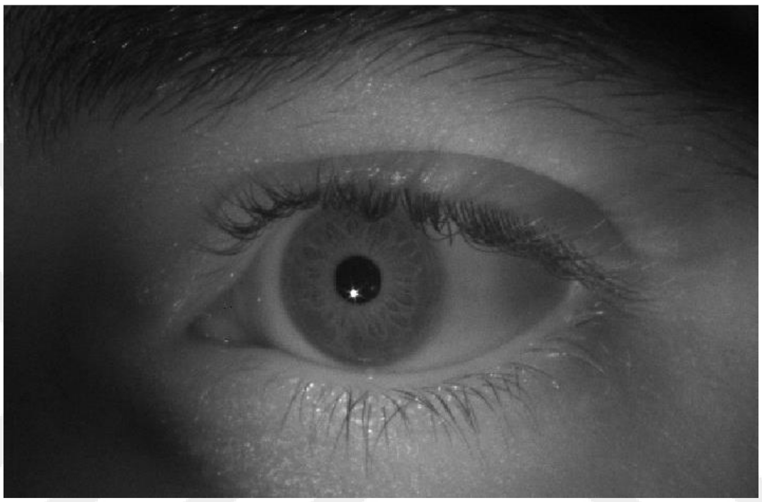

Figure 2.1. The captured image of the eye under IR illumination using a camera with its IR light blocker filter replaced by a visible light blocker.

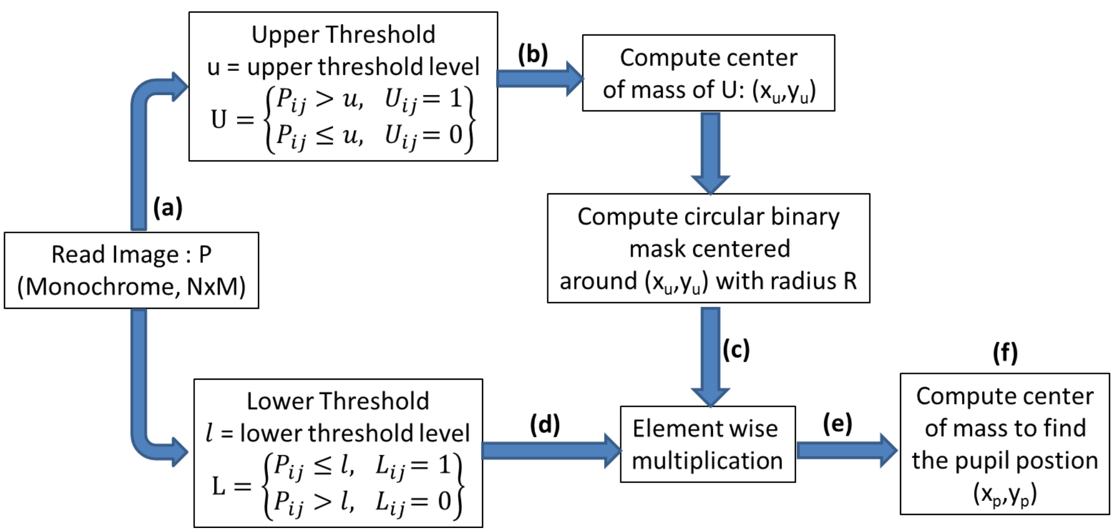

Figure 2.2. The block diagram of our pupil tracker algorithm.

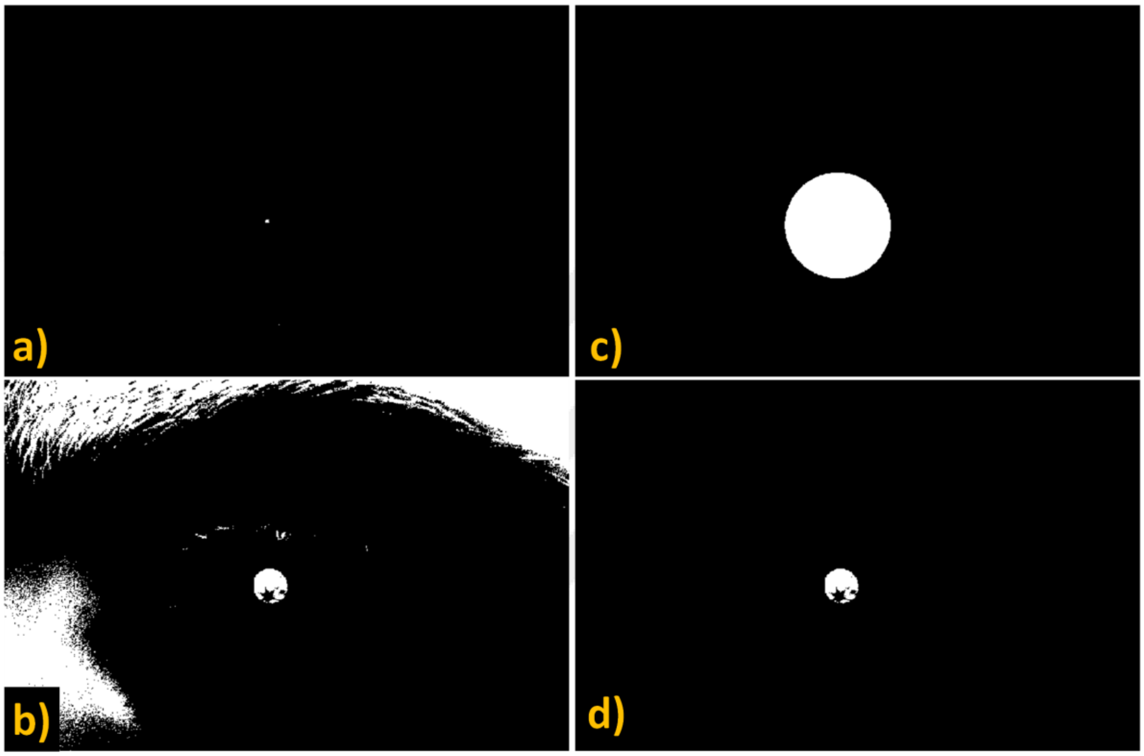

Figure 2.3. a) Upper thresholded image reveals the corneal reflection of the IR illumination LED. b) Lower thresholding creates a binary mask of dark pixels such as the pupil, eye lashes and eyebrows. c) The region of interest is selected as a circular mask that is centered at the center of mass of the image in a). d) Masking the image in b) filters out the undesired pixels and only the pupil pixels remain.

The algorithm works on IR illuminated pupil images and its block diagram is illustrated in Figure 2.2 and Figure 2.3. First, the position of the bright LED reflection is calculated by upper thresholding the acquired image and calculating the center of mass of the pixels above the threshold level. Then a binary circular mask is created centered around the calculated bright spot, which defines the region of interest. In parallel a lower threshold image is calculated from the acquired camera image. The lower thresholded image is masked by the circular mask and the center of mass in the resulting image is calculated, which gives the pupil position as shown in Figure 2.4. Defining a region of interest by upper thresholding brings immunity to undesired dark regions such as eyebrows, eyelashes and the edges of the eyelid as shown in Figure 2.3b.

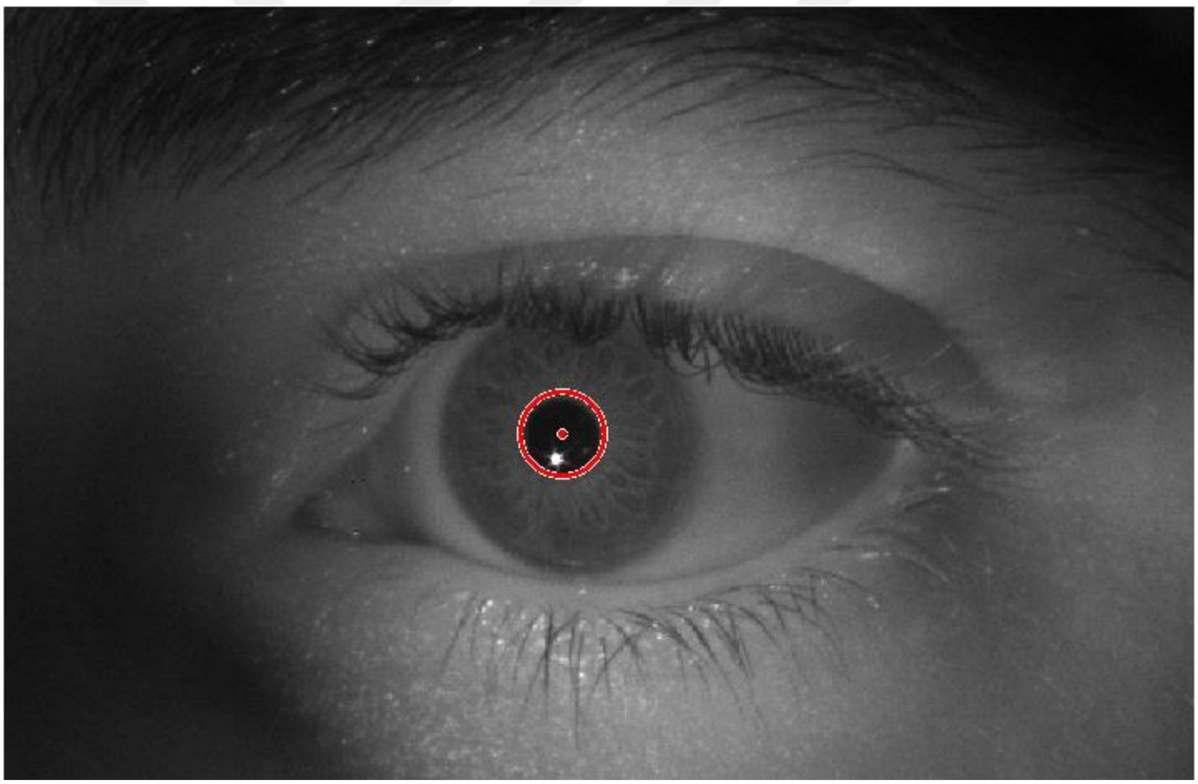

Figure 2.4. Calculating the center of mass of the pixel locations in Figure 2.3d yields the pupil position, which is denoted as a red circle on the original captured image.

We quantified the performance of our algorithm with two different experiments. First we showed two marked points to the user, which correspond to 0° and 20° gaze angles for a fixed head position. We asked the user to look at one of the marked points steadily and recorded the video of their eye. Then we run our pupil tracker algorithm on the videos and calculated the deviation of our algorithm as a function of time. Figure 2.5 shows the deviation plots for two gaze angles. The standard deviation for 0° and 20° gaze angles are 0.1° and 0.08°, respectively.

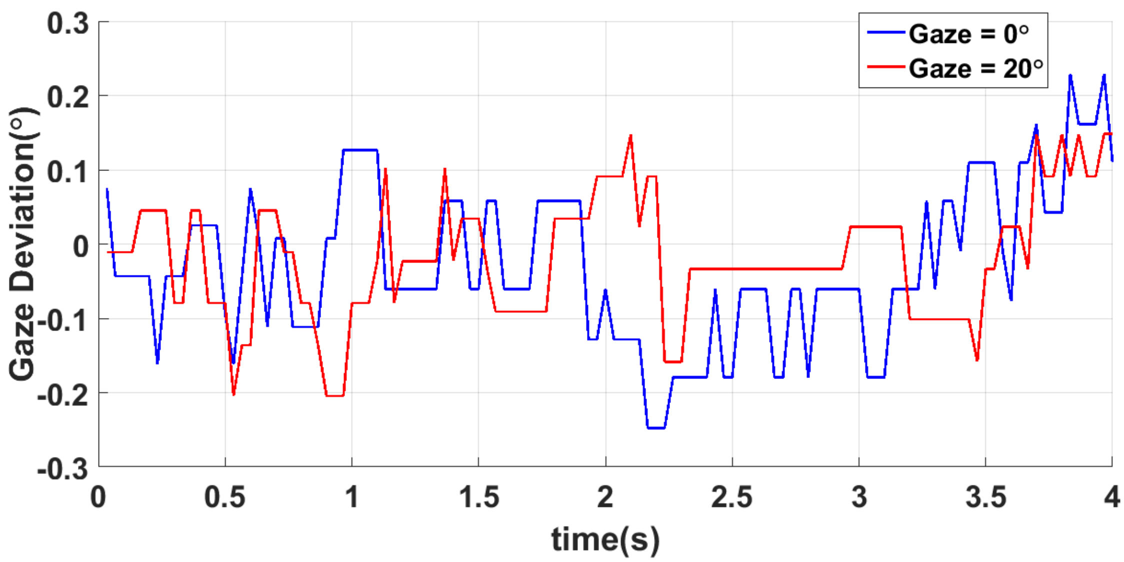

Figure 2.5. Noise analysis of our algorithm for two gaze points. Two videos are recorded while looking steadily at two marked point for gaze angles 0° and 20°, respectively. The videos are given to our algorithm as inputs and the gaze deviation data are extracted.

The second experiment quantifies the repeatability of our algorithm. We showed a rectangular grid of marked points from -20° to 20° horizontal and -10° to 10° vertical gaze angles with 10° step size, as shown in Figure 2.6 with brown squares. The user gazed at those points with an ‘S’ pattern from top left corner to the bottom right corner. This sequence is repeated five times and for each point the measured gaze angle is recorded, as shown with asterisks in Figure 2.6. The standard deviation for each gaze point is calculated and the average standard deviation of all gaze points is 1.07°.

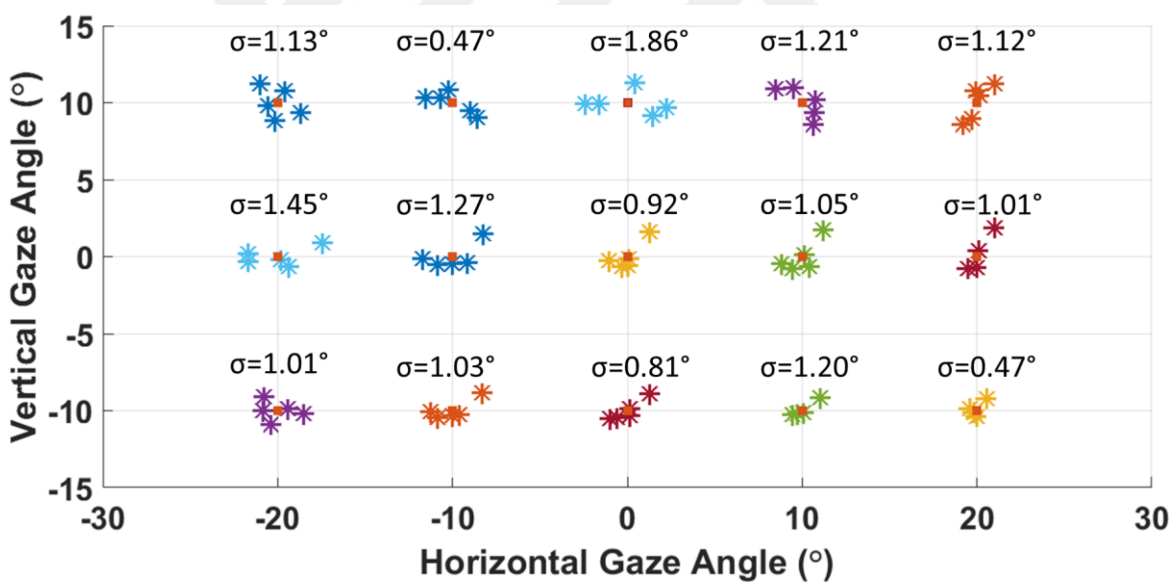

Figure 2.6. Repeatability measurement of our algorithm by moving the gaze across the field in a raster fashion 5 times. The average standard deviation for all gaze points is 1.07°.

3 LIGHT EFFICIENT DISPLAY USING PINHOLE IMAGING

Displays consume the largest amount of power in smart devices but only <0.1% of the display light actually enters through the viewer's pupil and nearly all the light is wasted. Similarly, for AR/VR headsets, light efficiency is extremely poor [3]. Another challenge in AR/VR headsets is the requirement for complicated optics and magnifier lenses to relay images from the microdisplay to the retina due to the limited refractive power of the human eye [30]-[32]. Maintaining large field-of-view and large eye-box using conventional optics is a major challenge [33]-[35]. As an alternative, microlens array [36], [37] and pinhole array based [38] light field displays have been demonstrated. Such solutions provide compactness but they suffer in terms of light efficiency.

To increase the light efficiency, what is known as the Maxwellian view has been used by many groups [39]. In this configuration, since the light source is imaged at the pupil, most of the light is captured by the eye, leading to a more light efficient display. Many variations of this technique have been demonstrated over the years. *Inami et. al* [40] showed a stereoscopic AR display using birdbath optics. High brightness potential of the Maxwellian view is demonstrated by *Beer et. al.* [41]. The main disadvantage of the Maxwellian view is that it has a small eyebox. If the eye rotates slightly, the focus spot is blocked by the iris and no light is delivered to retina. To extend the eyebox, *Takahashi et. al.* focused the light source to the rotation center of the eye at the cost of reduced FOV, solving the small eyebox problem [42].

If one can create a small eye-box that is also steerable, the display system would be extremely light efficient while providing a large eyebox. In holographic displays the eyebox can be steered by computing an appropriate hologram and multiple eyeboxes can be produced using HOEs but the image quality and FOV is limited [43]. *Travis et. al.* suggested a waveguide based display which steers the eyebox, the drawback is that it requires mechanical motion [44].

In Maxwellian view, the light source is focused onto the eye pupil and the display is optically imaged by the eye lens onto the retina. This means the display should be placed further than the near-point of the eye or it should be re-imaged to an appropriate distance for the eye to accommodate. This is a challenge for compact optical designs that is required for head-mounted displays. In this work, we developed a method to achieve a large eyebox display by adapting the well-known pinhole camera principle [45].

3.1 Pinhole Imaging

Unlike the Maxwellian view, the pinhole camera does not require any imaging components to create a sharp image at the retina as shown in Figure 3.1. An image on a microdisplay that is closer than the near point becomes resolvable to the eye and, therefore, complicated relay optics are not required. This is illustrated in Figure 3.2, where far objects can be focused onto the retina but objects closer than the near-point cannot form a sharp image. A sufficiently small pinhole aperture limits the extent of the rays and creates a sharp image at the back plane. By employing this principle, we can create sharp images at the retina even if the display is closer than the near-point of the eye.

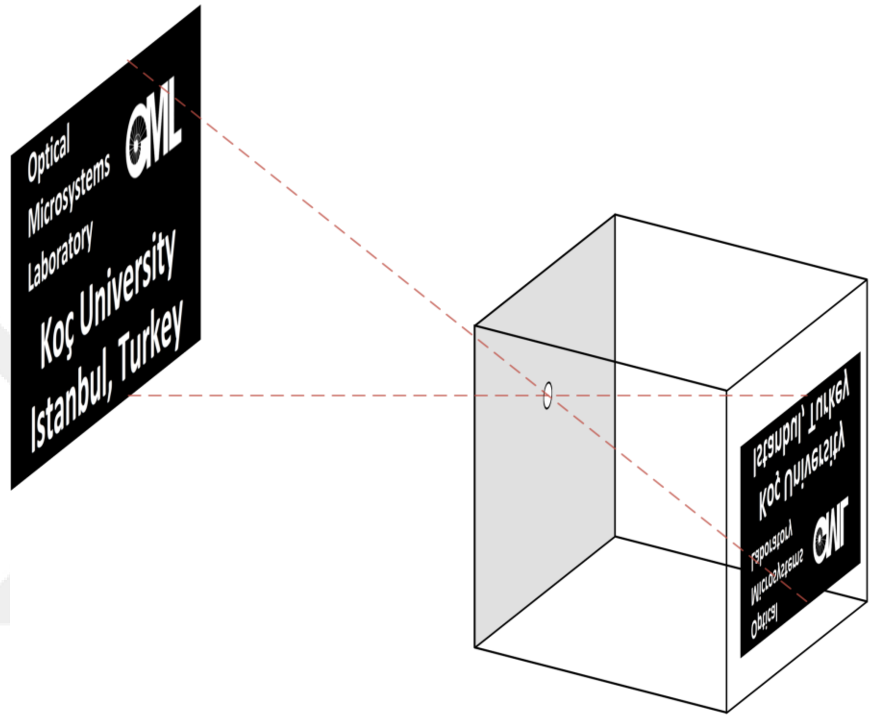

Figure 3.1. Pinhole camera does not need any optical elements to create a sharp image, which forms the basis of our head-worn display.

Small eyebox provide focus-free images but it is also a limitation. Assuming the pinhole is initially aligned with the center of the pupil, if the eye rotates more than half the pupil size, the iris blocks all the light, prohibiting image formation on the retina. In the following sections we discuss how to create a pinhole display using single LED illumination and how to steer the eyebox to follow the pupil as it rotates without any moving parts. This is the first report of low-latency, real-time pupil follower display system.

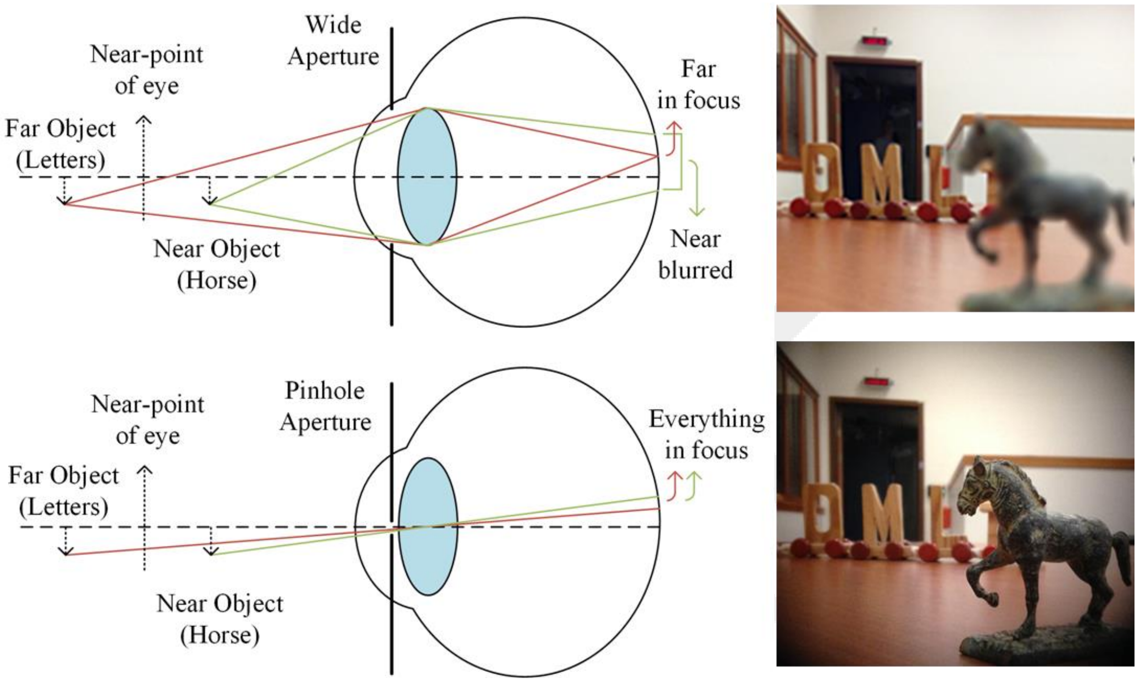

Figure 3.2. Due to the limited refractive power of the human eye, objects closer than the near-point of the eye cannot be viewed sharp. Pinhole imaging does not depend on the refractive power therefore objects at all depths appear always in focus.

3.2 Extended Eyebox using the Pupil Follower

We propose to achieve pinhole effect in an HMD configuration by using a point light source that is imaged on the viewer’s pupil. Since a very small portion of the eye lens is used, effective aperture is reduced and the depth of field is extended. Due to this large depth of field, everything is in focus regardless of the accommodation distance of the eye. Figure 3.3 illustrates our proposed system. A transparent microdisplay can be placed anywhere on the converging beam path and a sharp image forms on the retina even though there is no magnifier lens between the microdisplay and the eye.

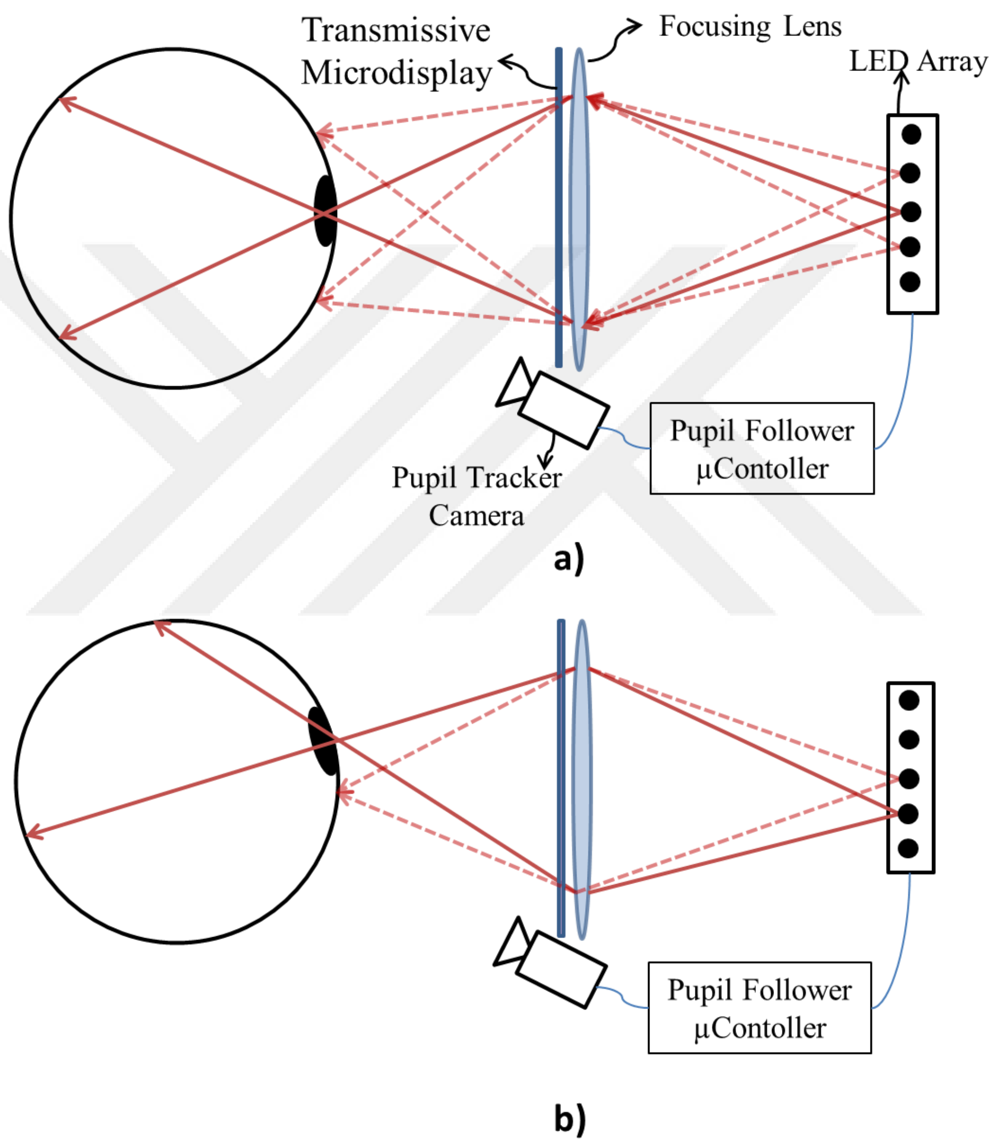

Figure 3.3. To implement pinhole imaging without an actual pinhole in front of the eye, we focus the illumination beam at the pupil.

The focus point is the eyebox of this system, thus the system has a very small eyebox. If the eye moves more than half the pupil size in any direction, the focused point is blocked by the iris, which means the image is lost. To extend the eyebox, light sources at different positions should be turned-on according to the pupil position at a given time. To do this we use an array of LEDs that is driven synchronously with a pupil tracker. The pupil tracker algorithm calculates the pupil position using image processing and turns-on the appropriate LED as illustrated in Figure 3.3.

Traditional backlit displays diffuse the light on the entire hemisphere but the eye captures only a small portion of it, so most of the light is wasted. In our proposed system, only a single LED is turned-on at a given time and the eye captures almost all the light emanating from it, making the system very light efficient. As this architecture is compact and energy efficient, it is suitable for HMDs.

Since the pupil position is monitored continuously in our system, the content on the LCD can be shifted based on the gaze direction. The dynamic shift of the content can be used to give binocular disparity and depth cues to the user for 3D perception.

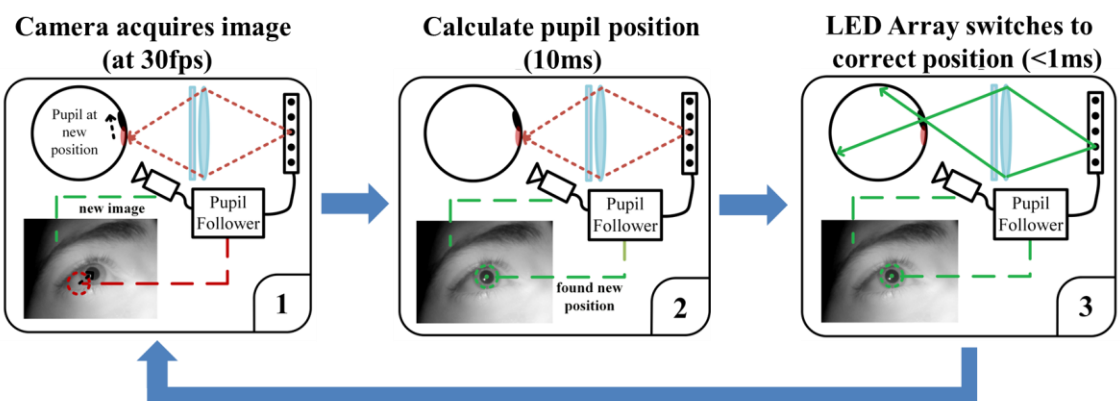

Figure 3.4. We synchronize the array of light sources with a pupil tracker and turn on only the required source so that the display can be seen in an extended eyebox.

Since we need very fast switching of LEDs according to the pupil tracker output we implemented our tracker algorithm on Beaglebone Black, which incorporates real time processor units. We implemented the algorithm using C programming language and run on Beaglebone Black and used the programmable real time units (PRU) on board to do the LED switching [46]. Similar pupil following schemes can be built using laser scanning pico-projector based displays but mechanical motion is needed to follow the pupil, which is much slower compared to turning-on an LED using real-time computing units. As a result, motion to photon latency is minimized in our system by utilizing PRUs.

Figure 3.4 illustrates the timing diagram of the pupil follower system. The pupil tracker algorithm running on Beaglebone is implemented using C language and it finds the pupil position in 10ms after the frame is captured. The tracker program sends this information to PRUs, which turn-on the appropriate LED within 1ms. In other words the whole operation takes about 11ms, which means the pupil follower system has the potential to run at 90fps. In our setup the camera speed was 30fps so it is camera limited. Figure 3.5 shows the pupil tracker camera images for two different pupil positions. The red dot at the pupil center shows the calculated pupil position and a red circle representing the pupil is drawn. On the right the corresponding LED is turned-on in real time by the PRU.

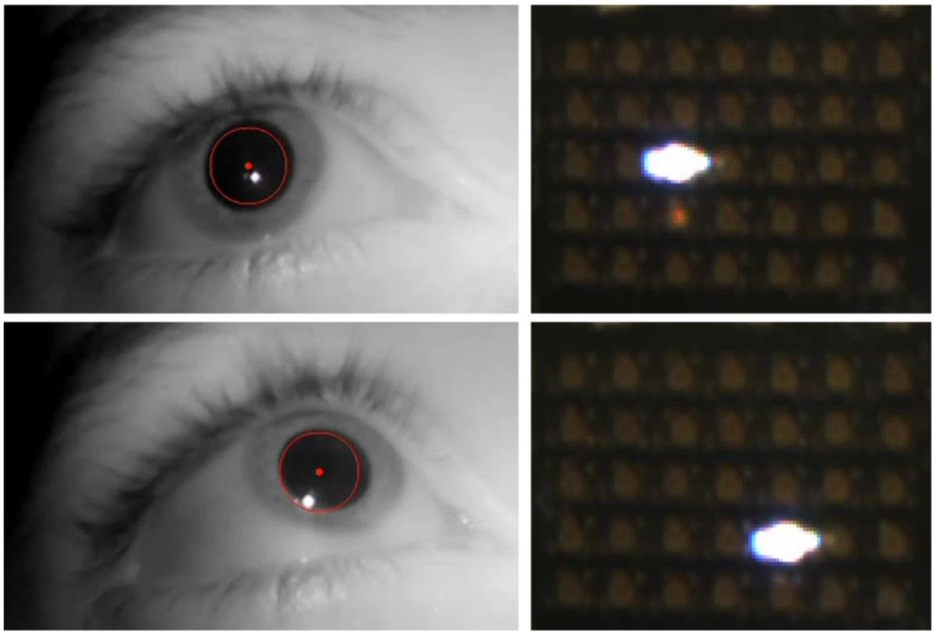

Figure 3.5. The LED array is synchronized with the camera based pupil tracker software and turn on only the required LED so that the display can be seen in an extended eyebox. We call this system the pupil follower display. The system use 5x7 array of RGB LED triads.

3.3 System Design

On the LED array, we use Lumex QuasarBrite-0404 LEDs as the light source because it has three colors (RGB) and small size (1 mm x 1mm). Due to the physical limitations, LEDs can be placed 2mm apart in each direction. The array consists of 5 rows and 7 columns of RGB LEDs, so there are 105 LEDs at 35 different locations.

The LED array is imaged at the pupil plane with unit magnification; therefore the instantaneous eyebox size is 1mm when the information content in the image is low-pass. Assuming typical pupil size is about 3mm in diameter, the distance between the images of the LEDs should be less than 3mm so that all pupil positions can be addressed without dark transition regions between the LEDs. The optical system that images the LED array is designed using Zemax software. Figure 3.6 shows the Zemax model of the system. Light from the LED array is collimated using a 75mm-focal length lens and then it is reflected from a 45-degree folding mirror. The reflected light is focused by a 75mm-focal length lens, which is relayed to the pupil plane using a beam splitter to make it function as an augmented reality display. The aperture of the focusing lens determines the field of view of the display. In the setup we used a 2-inch diameter lens, which gives about 37° FOV.

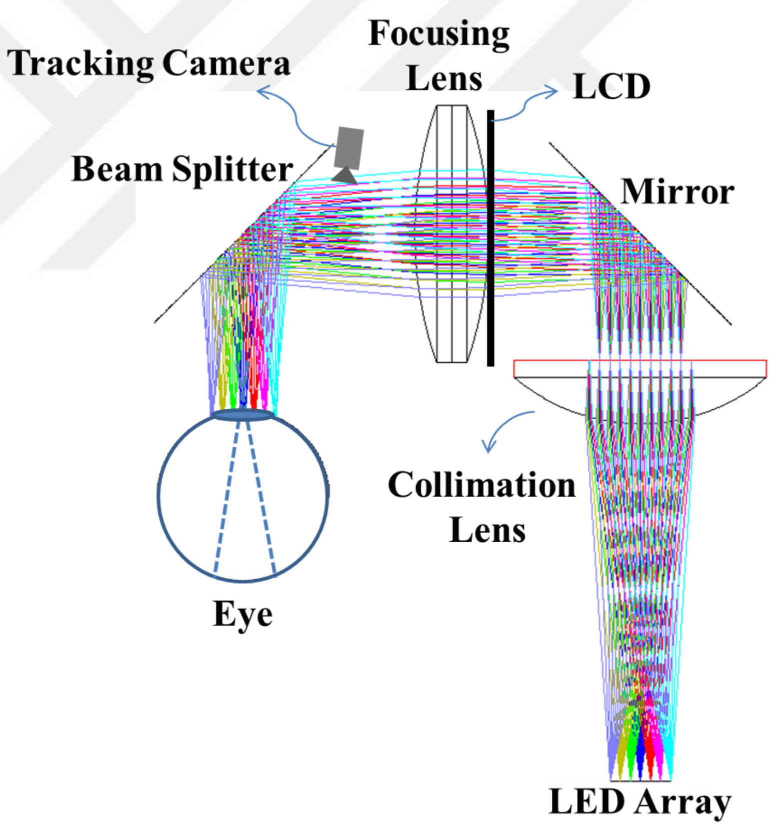

Figure 3.6. Zemax model of the optical system. LED array is imaged on the pupil plane with unit magnification. The LED spacing is set on the PCB such that their images are 2mm apart at the pupil plane.

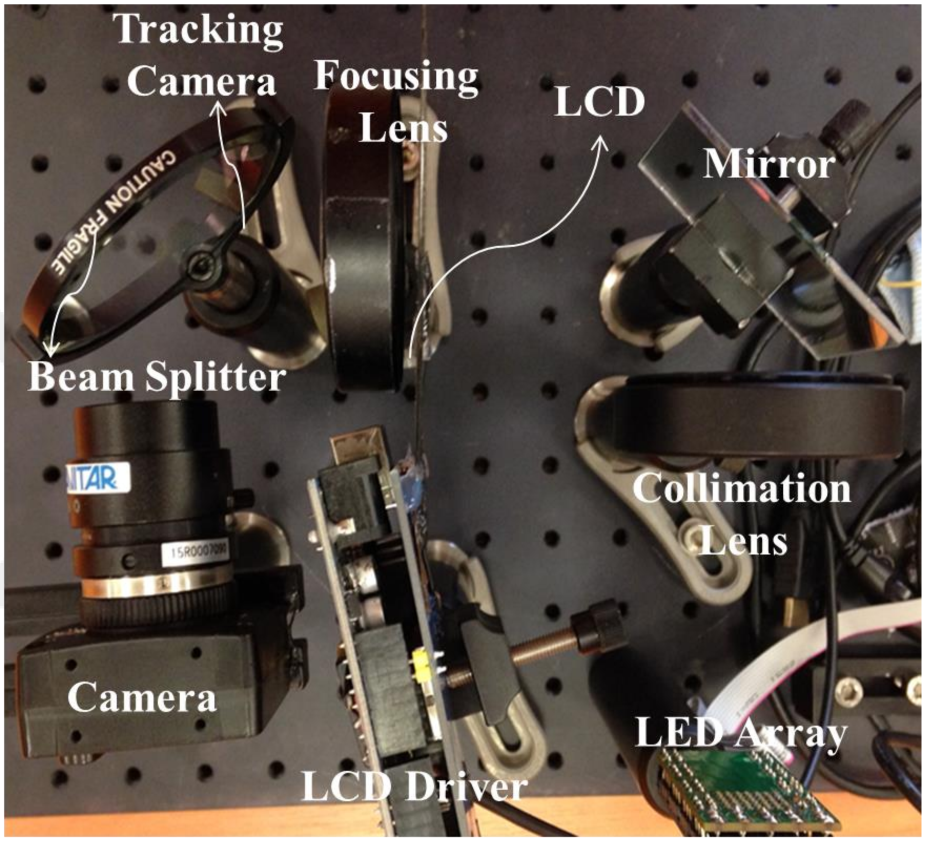

Figure 3.7. The optical setup on the bench.

Figure 3.7 shows the optical setup on the bench. The transmissive microdisplay is positioned right before the focusing lens. The setup is built for the right eye, which looks into the beam splitter. The beam splitter and the mirror fold the whole system towards the ear, which gives the natural shape of eye glasses. Figure 3.8 shows the LED array. LEDs are 1x1mm in size and they are placed 2mm apart in each direction and each LED unit have RGB LEDs in them. Figure 3.9 shows the image of the LED array at the pupil plane, with all LEDs turned-on to show the extended eyebox. The distance between the images of the LEDs is measured as 2mm, which results in an extended eyebox size of 14x10mm.

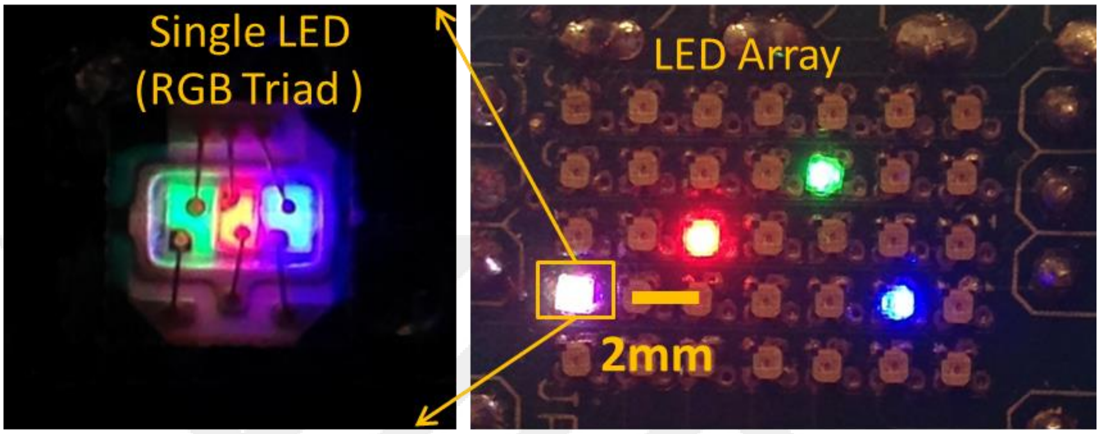

Figure 3.8. Image of a single LED unit on the left. Each unit has individually addressable RGB LEDs in them. The LED array on the right. LED units are 1x1mm in size and are placed 2mm apart in each direction

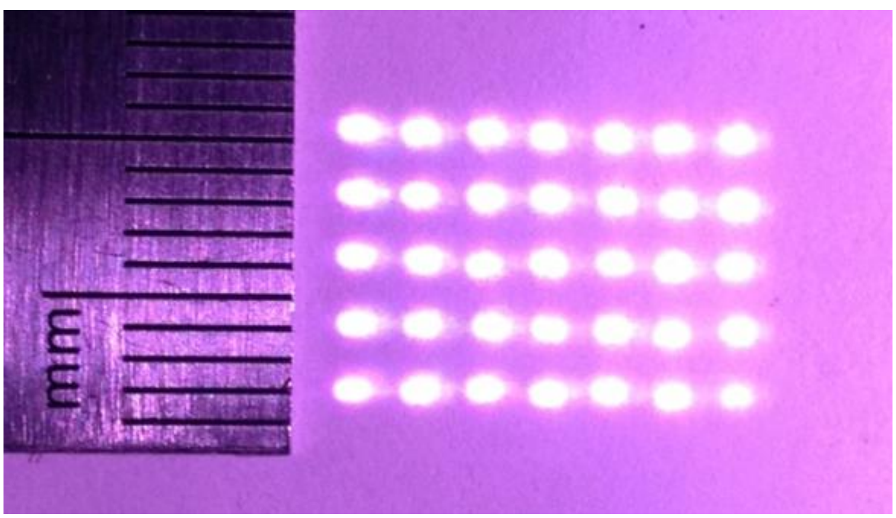

Figure 3.9. Image of the LEDs at the pupil plane when all of them are turned on. In actual operation only one RGB triad is turned on at a time. The images of the LEDs are 2mm apart by design.

There are various liquid crystal displays available on the market. Selecting the one with minimum pixel size to achieve maximum resolution seems intuitive in the beginning. To select the optimum pixel size, we ran physical optics simulations based on the angular spectrum approach [47]. We simulated pixel sizes from 60μm to 800μm and calculated the resulting spot size at the retina. As seen in Figure 3.10a, for small pixel sizes we see diffraction spread and for large pixel sizes the spot size converges to values predicted by geometrical optics, which increases linearly with pixel size.

According to our simulations 250μm pixel size yields the smallest spot size at the retina, hence the best resolution. The typical spot size criterion is the point where the encircled energy reaches 0.865 of the normalized encircled energy, which corresponds to $1/e^2$ diameter for Gaussian beams. We used full-width at half-maximum intensity (FWHM) as the spot criterion as it defines a smoother view with denser pixel count [48], [49]. Figure 3.10b shows the simulated cross-section of the spot at the retina for 250μm pixel size.

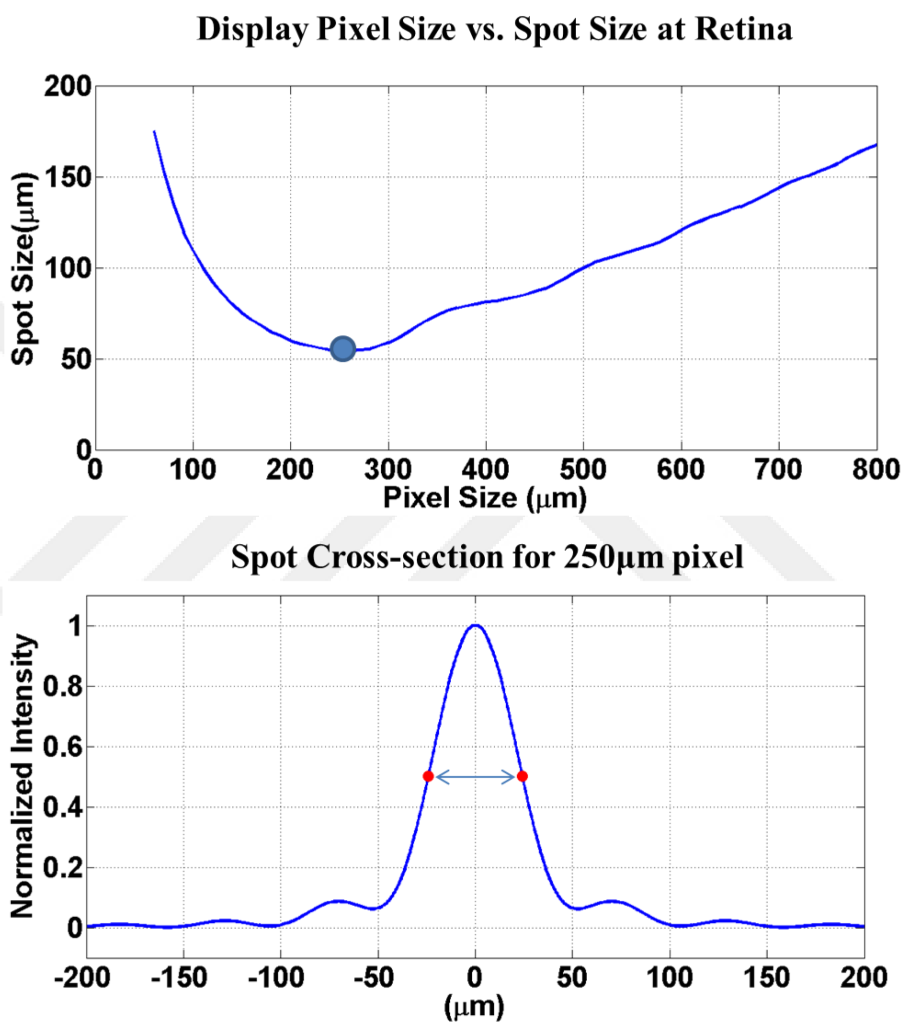

Figure 3.10 a) Physical optics simulations show the optimal pixel size for the LCD. Different pixel sizes are simulated using the angular spectrum method and the FWHM spot size at the retina is calculated. b) Cross-section of the smallest spot size at the retina for a 250μm pixel size, where the red dots mark the FWHM beam diameter.

3.4 Experimental Results

Having calculated the optimum pixel size for our LCD, we used a back-lit LCD module that has the closest pixel size to 250µm. We removed the back light unit along with diffuser films to get the bare LCD. We placed this bare LCD almost touching to the focusing lens to maximize our FOV and demonstrated our pinhole imaging display. Figure 3.11 and Figure 3.12 show the experimental results under bright ambient light. The image in Figure 3.11 is captured outside in a moderately sunny day. The prototype we built has a measured luminance of 360 cd/m^2 using an LED with 0.42 lumen total output. Due to the super-efficient nature of our display we can show bright images with a single low power LED even in outdoor settings.

Figure 3.11 Demonstration of the system outdoors. We can show bright images with a single low power LED as all the light is captured by the eye. FOV is roughly circular and 37^o.

Figure 3.12. Demonstration of the system for an indoor navigation scenario.

Since the effective aperture is very small, resolution of the display is reduced.

To quantify this degradation in resolution we simulated and experimentally verified the modulation transfer function (MTF) of the system as seen in Figure 3.14. The LCD we used has 200µm pixel pitch and is placed 75mm away from the eye, which means the maximum frequency that can be displayed with this LCD is 3.3 cyc/deg. Using the angular spectrum approach, we simulated a range of spatial frequencies that can be represented by integer number of pixels of our LCD as marked in the figure. Fringe contrast gives the

MTF value at that frequency. To obtain the continuous MTF curve, third order polynomials are fit between the simulated data points. To verify the simulations, we displayed the simulated frequencies on the LCD and captured the images with a camera, as shown in Figure 3.13. Although some modulation is visible for the highest frequency, which is marked as 1 in the figure, we can say that the cut-off frequency is about 2 cyc/deg, which is good enough to display simple symbols that is required in AR applications.

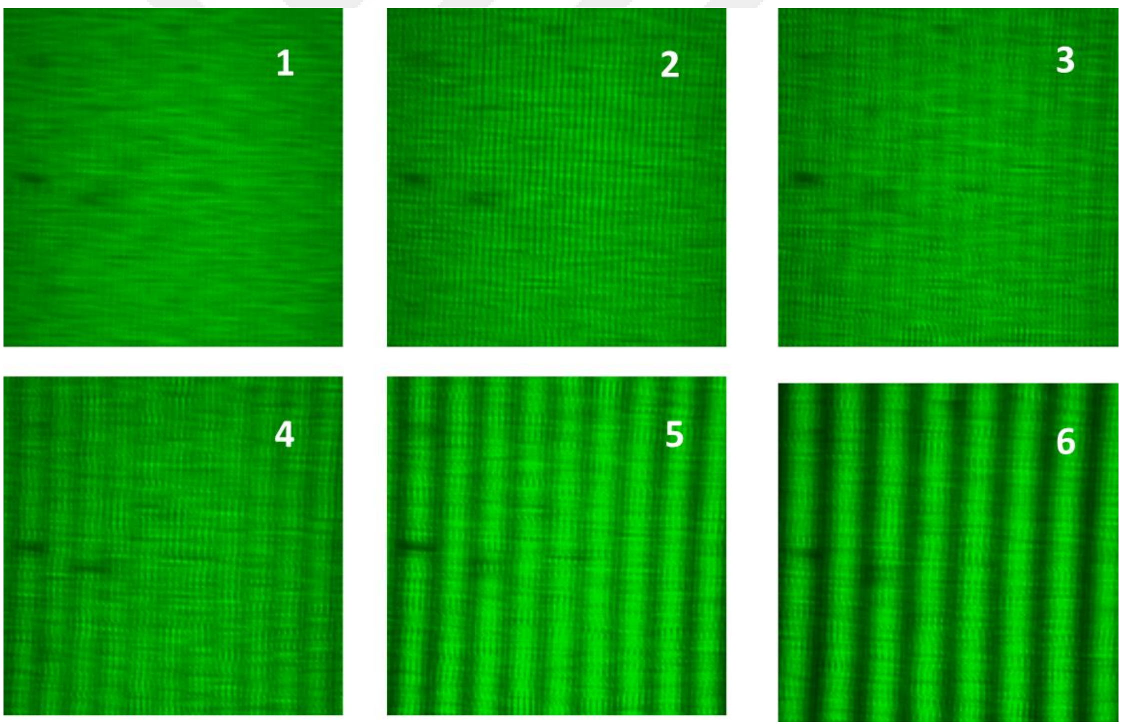

Figure 3.13. Experimental measurement of the MTF. Spatial frequencies marked on the MTF curve are displayed as bar patterns on the LCD and the images are taken by a camera. On the simulated MTF curve the cut-off frequency is calculated about 1 cyc/deg, which is confirmed by the experimental results.

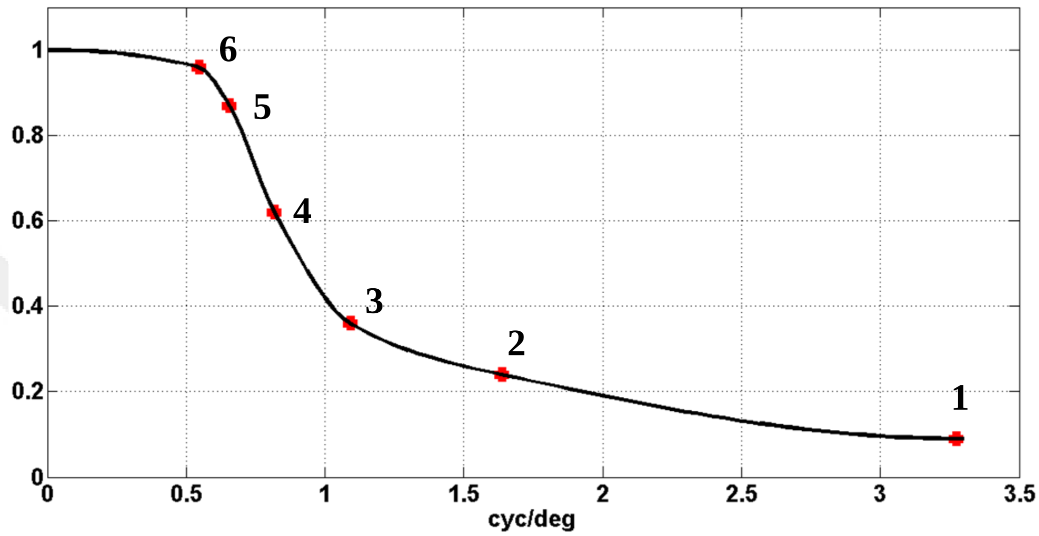

Figure 3.14 Simulated MTF of the pinhole display. Marked points denote the frequencies in Figure 3.13.

The frequency response of the system seems deficient but the reason is not just pinhole imaging. There is a transmissive LCD on the optical path, which behaves as a diffraction grating. The grating effect creates replicas of the LED, which degrades the resolution considerably. As seen in Figure 3.15 multiple diffraction orders enter the pupil. To verify this effect we placed an analog resolution chart as the image source, as seen in Figure 3.16, and focused the camera to 20cm distance. Since the resolution chart is not pixelated, it does not create any diffraction orders. It is clear that the pinhole imaging creates a sharp image despite the resolution chart is closer than the near point of the eye. To quantify the resolution degradation using an analog image we used the slanted edge technique [50]. The slanted edge is implemented by placing a razor at the display plane. The cut-off frequency is measured as 7cyc/deg, which is significantly larger than the cut-off frequency for the LCD case.

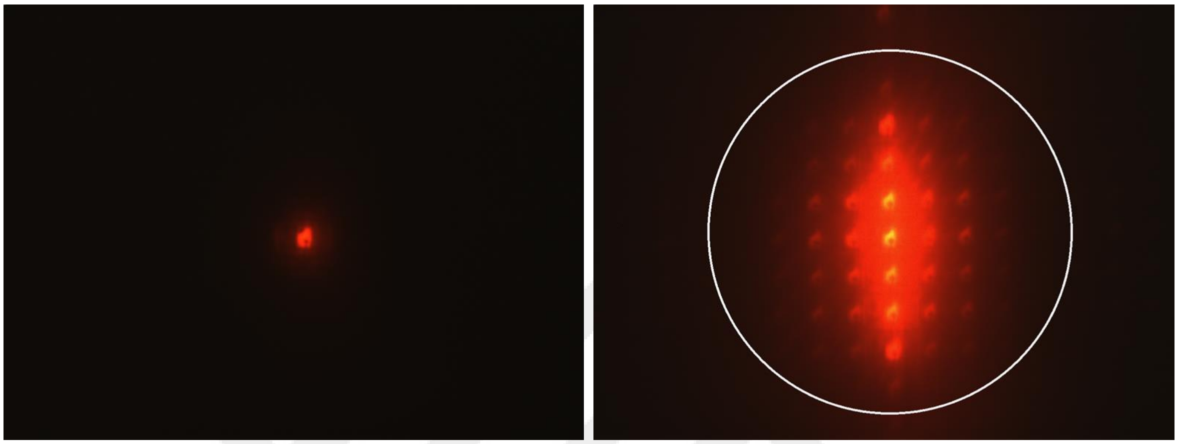

Figure 3.15. The image of the eyebox with no LCD on the optical path (left). The image of the eyebox with LCD on the optical path (right). The white circle shows the 3mm pupil.

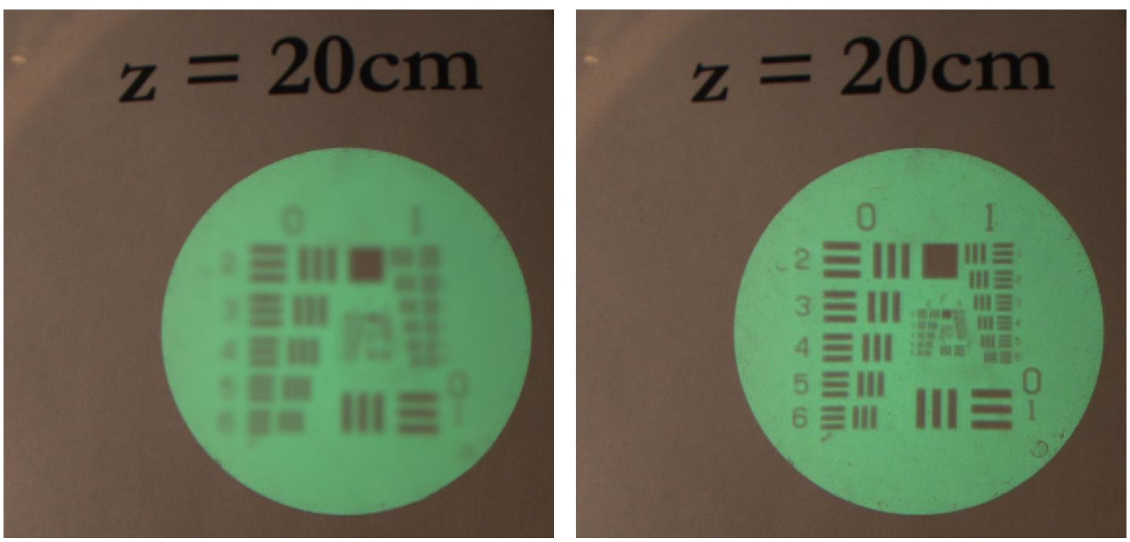

Figure 3.16. The camera is focused at 20cm. The resolution chart is placed directly in front of the eye, closer than the near point of the eye (left). The resolution chart is placed on the converging beam that creates the pinhole effect (right).

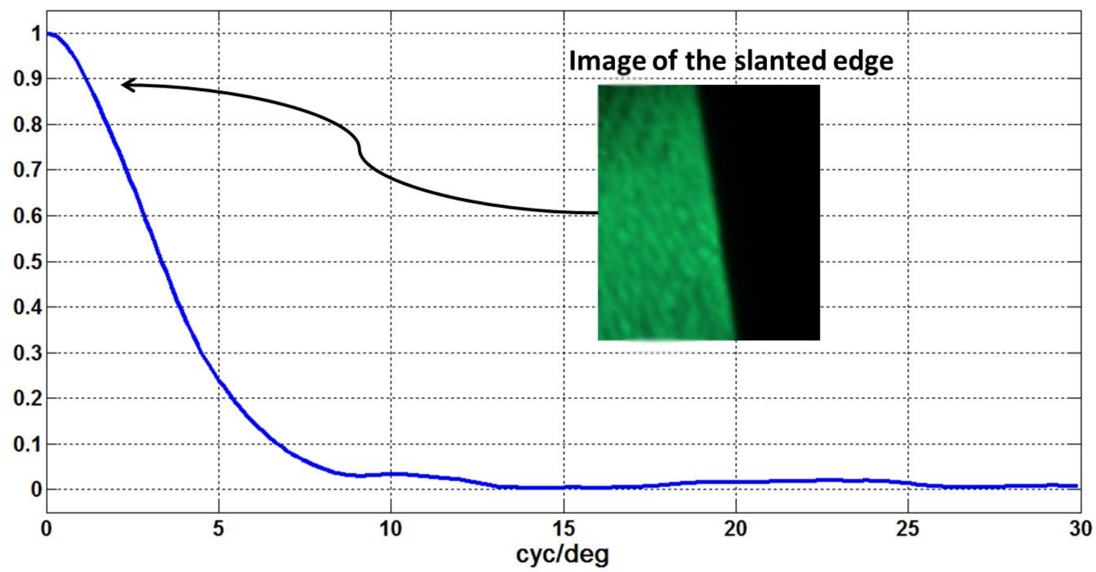

Figure 3.17. The MTF of the analog display is measured using the slanted edge technique.

3.5 Conclusion

We successfully demonstrated a new head-mounted, near-to-eye display architecture based on the well-known pinhole imaging principle. This architecture alleviates the problem of the human eye being unable to directly resolve near-to-eye displays. The proposed system counters the small eyebox problem arising from the pinhole imaging approach by extending the effective eyebox with a pupil follower with only 11msec motion-to-photon latency. The pupil follower also creates a super light efficient display since nearly all light emanating from the source enters the eye, making it suitable for mobile applications. The prototype achieved 37° circular FOV with a luminance of 360 cd/m^2 using an LED with only 0.42 lumen output. The MTF cutoff frequency for the display system was measured to be approximately 2 cyc/deg. Good quality experimental results for a real use case were observed on a prototype setup with visually undetectable motion-to-photon latency. Pupil follower concept can be applicable to other HMD architectures such as holographic displays and foveated displays, therefore it will be of interest to a broader audience.

4 FOVEATED HOLOGRAPHIC NEAR-EYE DISPLAY USING ROTATING BEAM SPLITTERS

4.1 Foveated Displays

In essence near-eye displays relay a magnified image of the image source (i.e. a microdisplay) to the field-of-view (FOV) of the user. To achieve high resolution, the pixel size of the microdisplay should be small. Considering the typical pixel size is about 5μm, a full HD microdisplay is roughly 10x5mm in size, which is quite small. To provide large FOV with such a small microdisplay, large magnification optics is required, which means the apparent pixel size is increased, hence the maximum spatial resolution that can be displayed is reduced as illustrated in Figure 1.27. This phenomenon is known as the resolution-FOV invariant [3].

As a solution high-resolution area of interest, partial binocular overlap, optical tiling and dichoptic area of interest have been suggested by Melzer [51]. Optical tiling is considered to be the most scalable of these approaches [52] Many different tiling based HMDs were developed by different groups over the years. Melzer et. al. developed a compact optical unit and tried to overcome seam artifacts in their tiled virtual reality display [53]. Hua et. al developed a compact and transparent free-form optical component that is suitable for tiling. They demonstrated their tiled augmented reality HMDs using their novel free-form prism [54]-[56]. Similarly, Wang et. al demonstrated their tiled display with spherical components and discuss the design parameters of tiled HMDs in detail [57]. Recently Zheng et. al. demonstrated a holographic tiled display using two SLMs per eye [58].

As discussed by *Hua et. al*. optical tiling has some major disadvantages [52]. For instance the seams at the transition regions of the tiled displays are visible to the eye. If tiled on a plane, the magnification becomes non-uniform across the FOV. Tiling large number of displays increases the overall weight and size and they usually lack see-through capability. Moreover, driving many displays simultaneously is a major challenge in terms of electrical power and computational load.

To overcome the limitations of tiled displays, we used what is known as the foveated display concept [59]. Sensory cells at the retina of the human eye are distributed non-uniformly, with highest density in the fovea and rapidly decreasing towards the periphery as shown in Figure 1.29 [60]. This results in a non-uniform spatial resolution in the perceived vision. We see the central part of our vision with high resolution and the peripheral vision seems blurred as illustrated in Figure 4.1. The angular extent of this high resolution region of the eye is about 10 degrees [61], [62]. Therefore, providing high resolution images to the peripheral vision is wasteful. More efficient and simpler optical architectures can be developed to provide high resolution content to the fovea and a simple low resolution display can be utilized to provide the peripheral vision. This requires a pupil tracker and a suitable optical system to dynamically deliver the high resolution image to the fovea and efficient computational resources to operate without noticeable lag.

Figure 4.1. Image with constant spatial resolution on the left. Foveated image that is simulated based on the receptor distribution in Figure 1.29 on the right. Due to the non-uniform distribution of receptor cells in the retina the spatial resolution varies across the perceived image. Fovea has the highest resolution and it rapidly decreases towards the periphery, which means the perceived image at the central vision is sharp whereas peripheral vision is blurred.

Recently *Kim et. al.*demonstrated their foveated AR display using a micro OLED display, which translates in two axis to follow the fovea and moves in the third axis to adjust the image depth [63]. They demonstrated their closed-loop system with bulky bench-top linear actuators to move the OLED in 3D space. In our approach the image source is static but its image is relayed to the eye using two beam splitters. Rotation of the beam splitters changes the location and orientation of the virtual image of the display; thus running the system with a pupil tracker as close-loop system results in a dynamic foveated display. As we use a phase-only SLM as the image source, our system delivers holographic images.

4.2 Rotating Beam Splitter Approach

We designed our system to provide a high resolution holographic image to the fovea as illustrated in Figure 4.2. A collimated LED illuminates the phase only spatial light modulator (SLM). Reflected light is modulated according to the hologram on the SLM and gets focused by a lens to the pupil plane to create the Fourier plane. To extend the FOV two beam splitters in the optical setup are rotated according to the pupil position such that the image of the SLM appears directly in front of the eye, perpendicular to the gaze direction. To achieve this, the beam splitters are mounted on miniature servo motors which are driven based on the pupil position that is calculated from the tracker camera images.

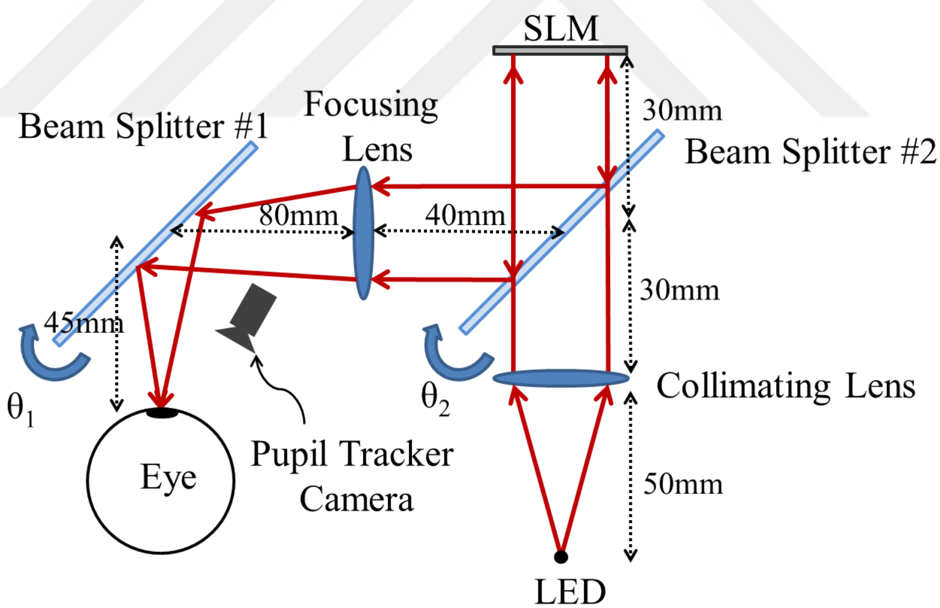

Figure 4.2. Conceptual drawing of our foveated AR display. The SLM is illuminated by a collimated LED and the reflected light is focused by a lens to the pupil plane. The beam splitters are rotated in sync with the pupil tracker to steer the FOV based on the gaze direction.

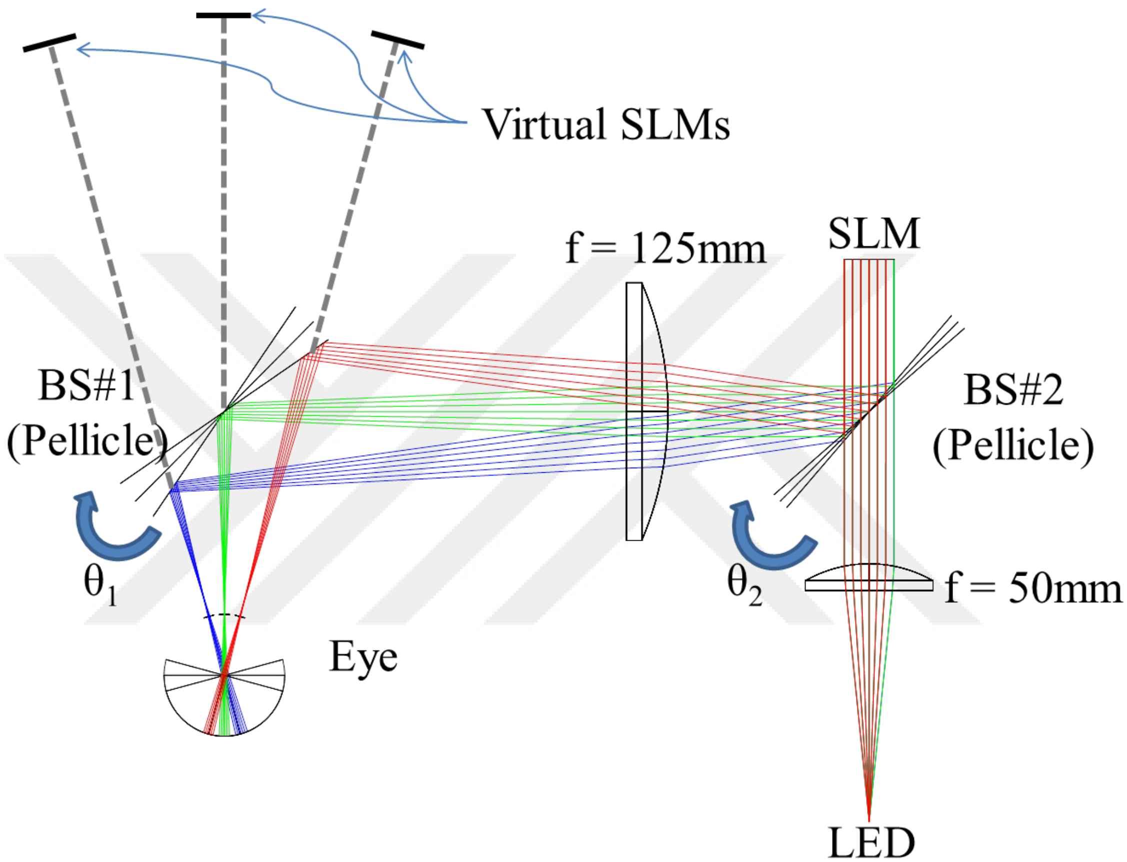

Figure 4.3. Zemax model of our foveated display. The beam splitters are rotated in the same direction based on the pupil position such that the SLM always appears perpendicular to the viewing direction.

We modeled the optical system in Zemax as seen in Figure 4.3. The SLM we used in the setup was Holoeye Pluto, with a resolution of 1920x1080 pixels and 8μm pixel pitch. The focusing lens has a focal length of 125mm, which means the SLM can provide 4x7 degrees of static field of view (FOV). The choice of beam splitters is 2-inch diameter pellicle beam splitters for their light weight and ghost-free properties. Different colors in the simulation show different rotation angles of the eye. As seen in the Zemax model, the size of the beam splitter in front of the eye limits the range of gaze angles that can be handled. In our current setup the virtual image of the SLM can be steered by ±15 degrees in the horizontal direction. Considering the SLM has 7 degrees horizontal FOV, the total FOV can be extended to 37 degrees in the horizontal direction.

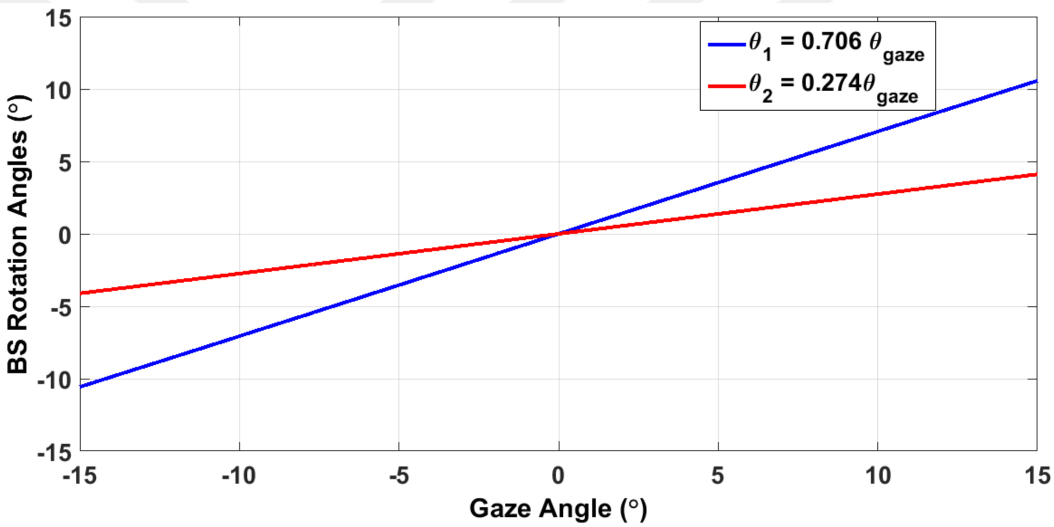

Figure 4.4. The plot of the rotations angles of the beam splitters based on Zemax optimizations. Both of the beam splitters rotate in the same direction as a linear function of the gaze angle.

To determine the rotations angles for the beam splitters we wrote a merit function such that the ray hitting the center of the SLM enters the eye pupil from its center and hits the retina at 90 degrees, which ensures that the virtual SLM is perpendicular to the viewing direction. We also wrote a Zemax macro that sweeps the viewing direction and optimize the rotation angles based on the merit function described above and records the rotation angles in a file. Figure 4.4 shows the plots of the rotation angles of the two beam splitters with respect to the gaze angle in the horizontal direction. The rotations are symmetric about 0 degrees gaze angle and two beam splitters move in the same direction. The beam splitter in front of the eye rotates more than the other one and there seems to be a fixed rate between them, which is about 2.57. For ±15 degrees rotation of the eye the beam splitter #1 and #2 rotates ±10.59 and ±4.11 degrees, respectively.

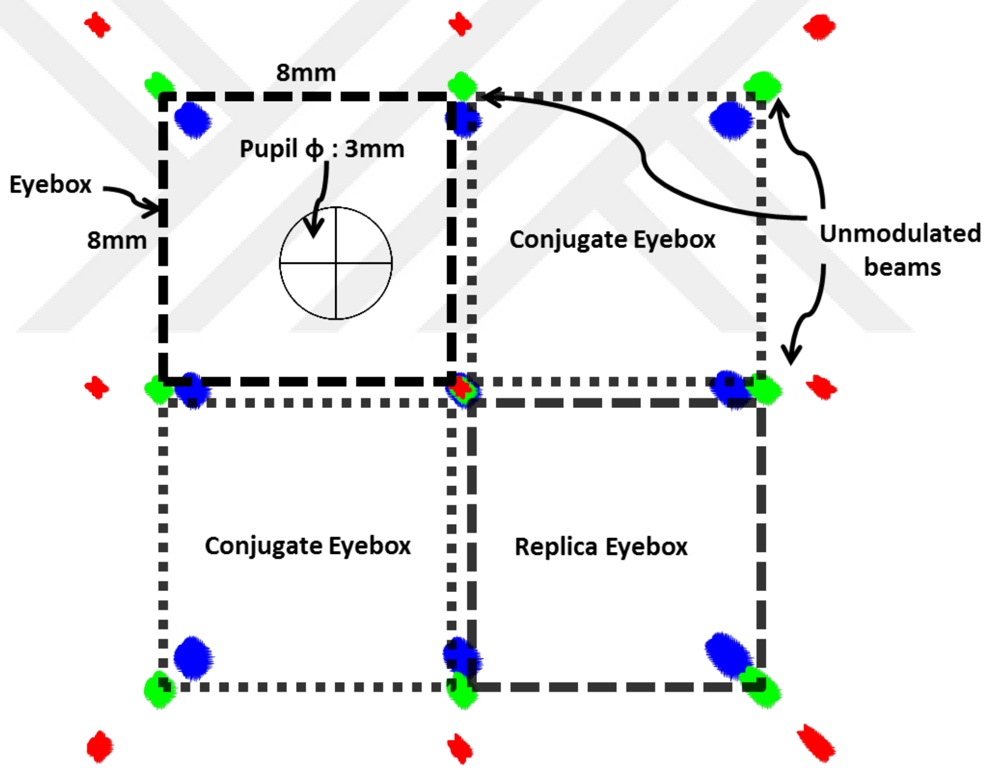

Figure 4.5. Simulation of the diffraction orders of the illumination beam for RGB wavelengths. Pixellated structure of the SLM creates periodic diffraction orders which should not enter the eye. Simulation confims that there is a safe margin between the orders and the 3mm eye pupil.

Since the SLM has a pixelated structure it creates diffraction orders. Diffraction orders due to the illumination beam should not enter the eye as they are disturbing bright spots with no information. The SLM is modeled as a diffraction grating in Zemax and the diffraction order distribution at the pupil plane is simulated. As seen in Figure 4.5, a pupil with 3mm diameter can be positioned between the diffraction orders with a safe margin. The space between the diffraction orders defines the eyebox, which is 8x8mm in our setup for 525nm wavelength. The red and blue wavelengths are also included in the simulation to show the full color eyebox.

4.3 Servo Motor with Optical Feedback

To rotate the beam-splitters servo motors are used. Initially we used commercially available servo motors but their accuracy and repeatability were not satisfactorily, therefore we decided to build our own servos. We designed a unique optical aperture that rotates with the motor shaft, as shown in Figure 4.6. The aperture is designed such that the light intensity that passes through it changes linearly with the rotation angle. By placing the aperture in between a stationary LED and a photodiode, the rotation of the motor shaft can be measured very accurately. We used this sensor to build a closed-loop control system that rotates the beam-splitters mounted on the motors. The servo motor system is shown in Figure 4.7.

Figure 4.6. Calculated aperture pattern which transmits the light intensity linearly as a function of rotation angle.

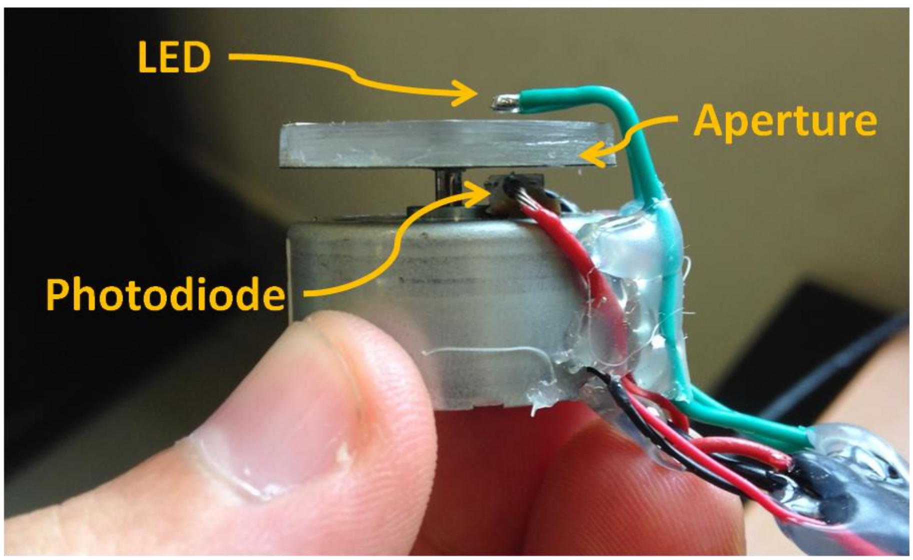

Figure 4.7. The servo motor architecture. The binary pattern is attached to the rotor of the motor, which rotates between a stationary LED and a photodiode.

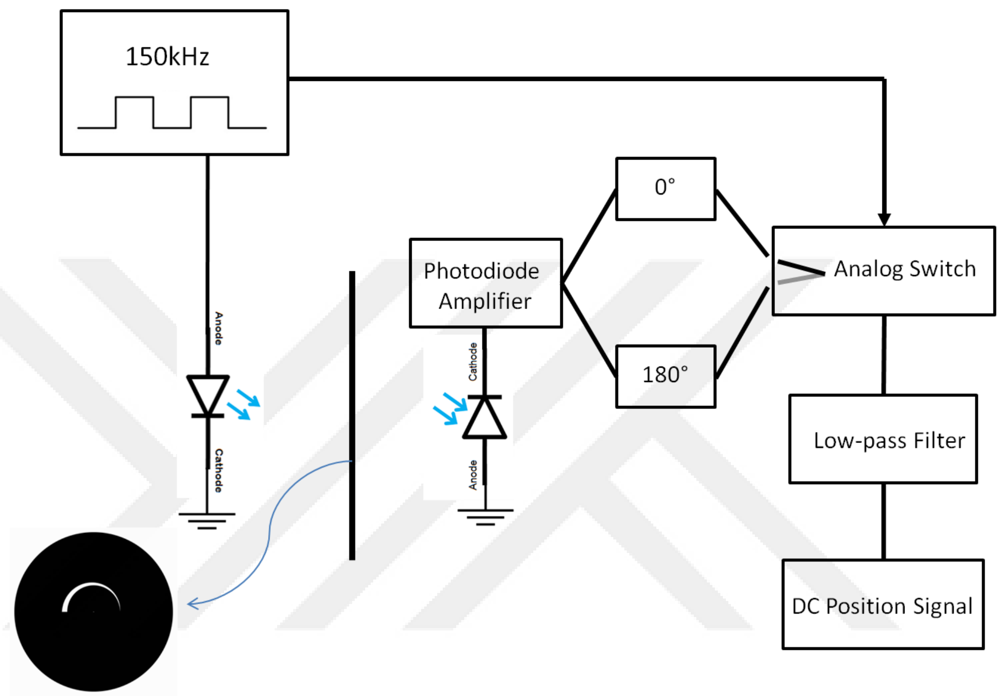

Figure 4.8. The block diagram of the electronics of our rotation sensor.

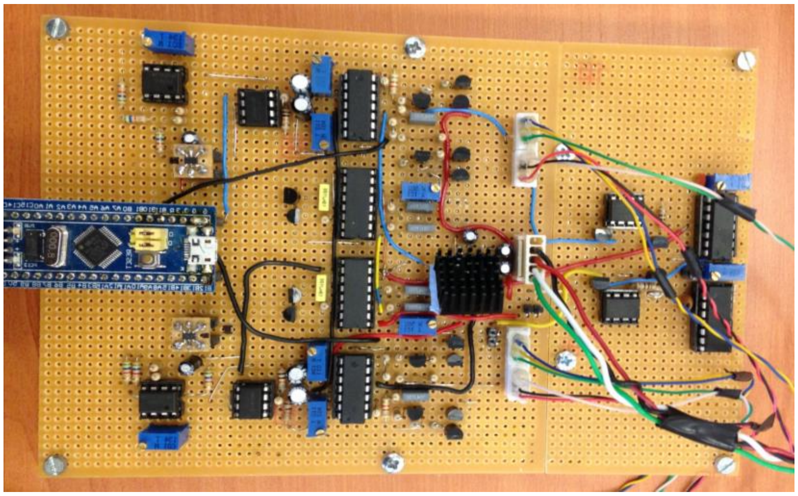

Figure 4.9. Implementation of the electronic circuit for two servo motors including PID controllers.

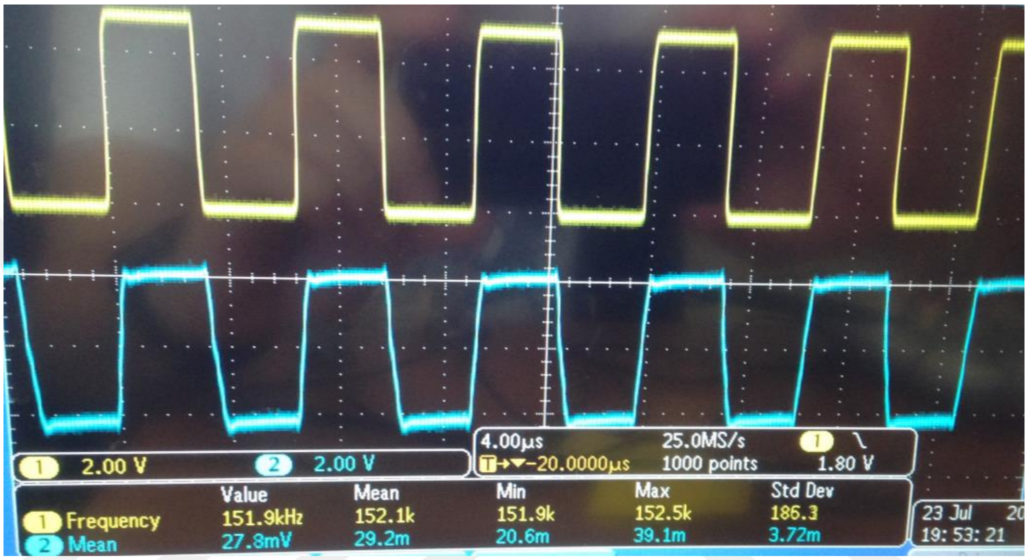

Figure 4.10. The in phase amplified signal.

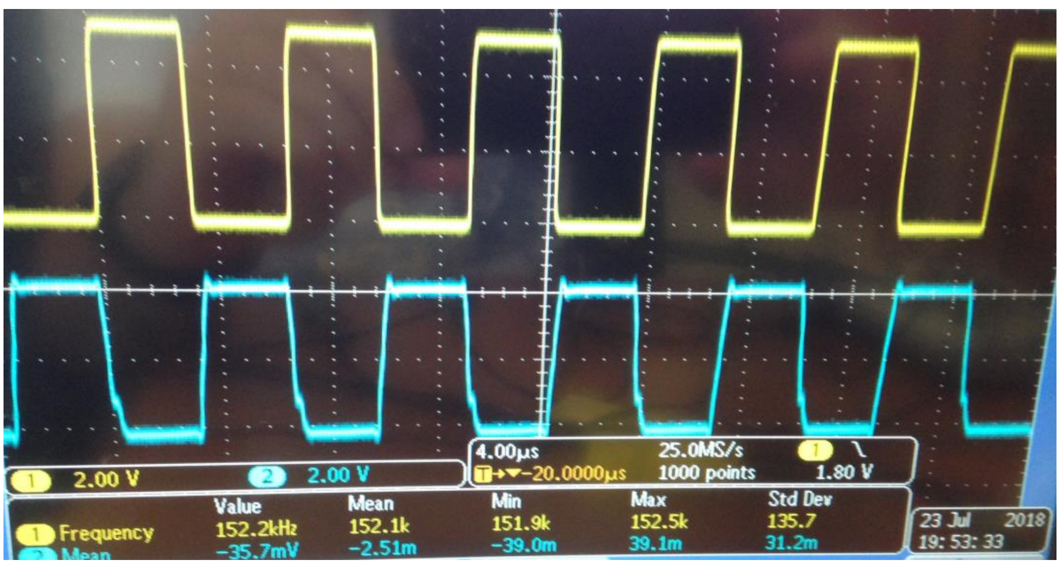

Figure 4.11. 180° shifted amplified signal.

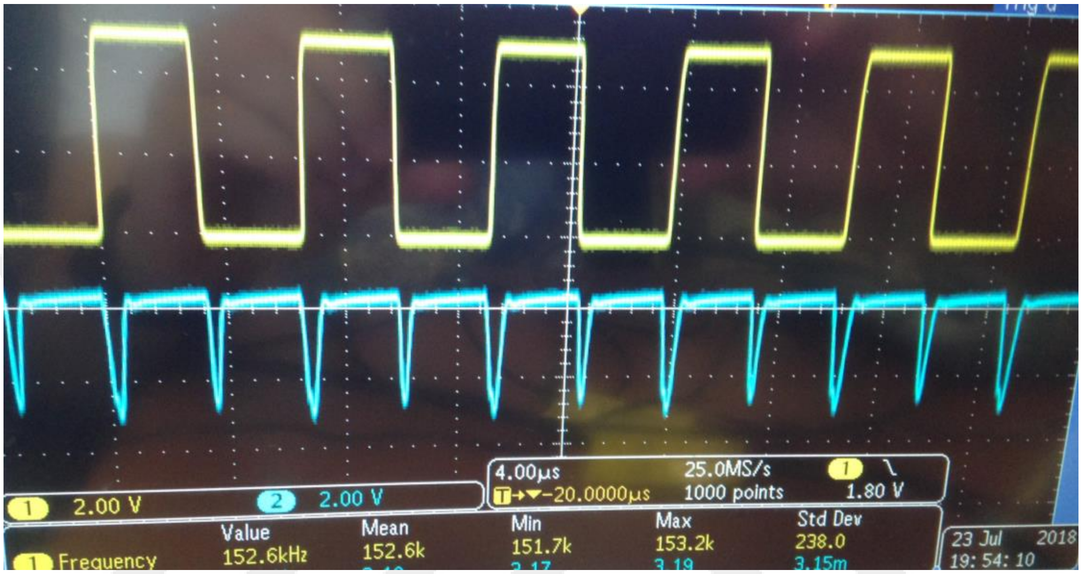

Figure 4.12. Output signal of the analog switch stage.

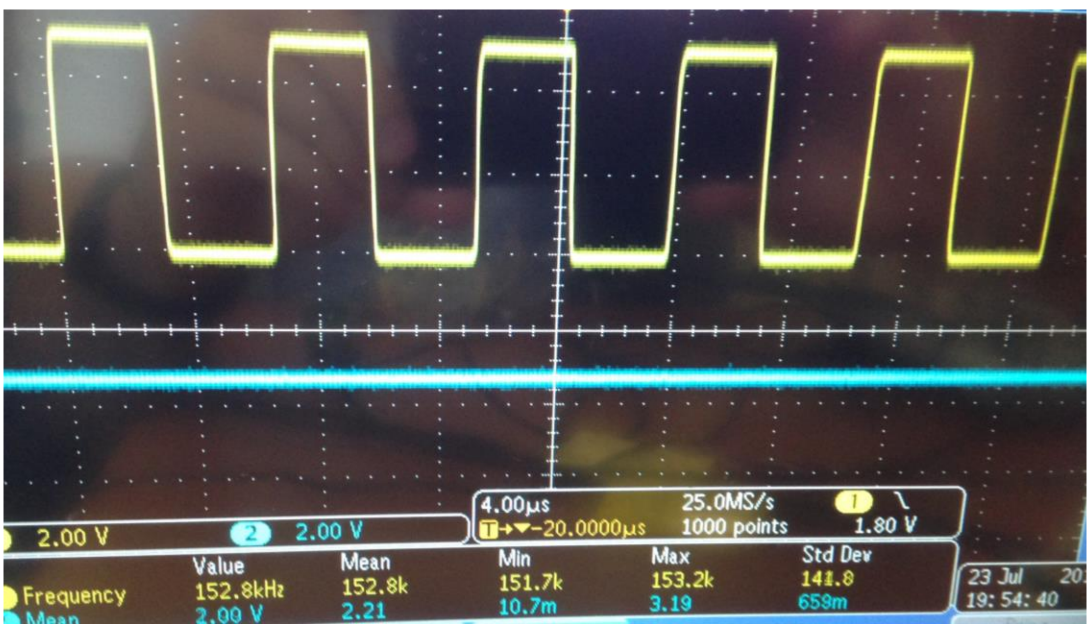

Figure 4.13. Output signal of the low-pass filtered signal.

To measure the transmitted light accurately and to provide background and noise immunity we implemented an analog homodyne detection circuit as illustrated in Figure 4.8. The LED is modulated at 150kHz and the photodiode amplifier circuit chops the signal with the modulation signal. This mixing operation modulates the low frequency background and noise signals to high frequency and demodulates the high frequency LED signal. Simple low-pass filtering eliminates all the undesired signals and the detector signal is obtained as a clean DC signal for a fixed angle. In essence the circuit implements a square wave lock-in amplifier which only measures the 150 kHz modulation signal. Figure 4.10 to Figure 4.13 show the outputs of the relevant blocks in Figure 4.8.

The rotation sensor output is obtained as an analog voltage, it is converted to a digital value using a 12-bit 1MSPS ADC that is embedded in a STM32F103 microcontroller. The microcontroller receives the set points for the motors through USB and performs digital PID control. The digital control outputs are converted to analog signals using DACs and the signals are conditioned to drive the motor coils. The implementation of the circuit can be seen in Figure 4.9.

4.4 Hologram Computation

To deliver holographic content, appropriate holograms should be calculated and displayed on the SLM. There are many different hologram computation techniques in the literature [64]-[68]. Most of these methods compute the full-complex hologram for a given input image. Since our SLM is a phase-only device we used an iterative Fourier transform based algorithm [69], which computes the phase-only holograms. Due to the iterative nature of the algorithm real time computation is not possible; therefore we pre-calculated the holograms for our set of input images and update them in real time based on the gaze direction.

A generalized and simplified explanation of the algorithm is as follows: The SLM projects an image at a certain depth through some optical components and free-space propagations. Initially the desired image to be projected is placed at the projection distance as an amplitude image with random phase. The complex field is back propagated to the SLM through the optical system and the resulting complex field at the SLM plane is cropped by the SLM aperture. The amplitude of the complex field is discarded and remaining phase is placed on the SLM. This time the phase only field is propagated to the desired image plane. At the image plane the amplitude of the field is replaced by the desired image and the phase is left as is. The resulting complex field is back propagated to the SLM plane and the amplitude is discarded at that plane. This process is iterated many times and in the end the phase only hologram that gives the desired image at the image plane is obtained. As an example, Figure 4.14 shows the desired image and Figure 4.15 shows its calculated phase only hologram which is coded as an 8-bit image.

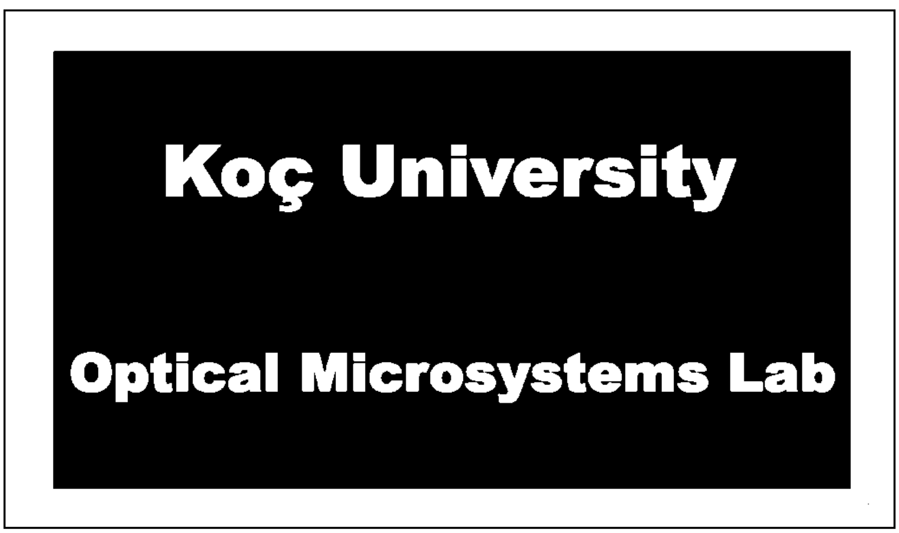

Figure 4.14. Input image.

Figure 4.15. Calculated hologram.

4.5 Experimental Results

After building the servo motors and computing the phase-only holograms, we built the simulated system in Figure 4.3 using a 3D printed part, as seen in Figure 4.16. First, we exported the CAD model of the system from Zemax and designed an appropriate closure and holders for the components. Second, we integrated the pupil tracker to the mechanical system. The SLM is illuminated by a collimated green LED and the reflected light is relayed towards the eye using two beam-splitters. The focusing lens in between the beam-splitters create the eyebox for the viewer. The beam-splitters are rotated individually to track the pupil position so that the holographic image is perpendicular to the viewing direction all the time.

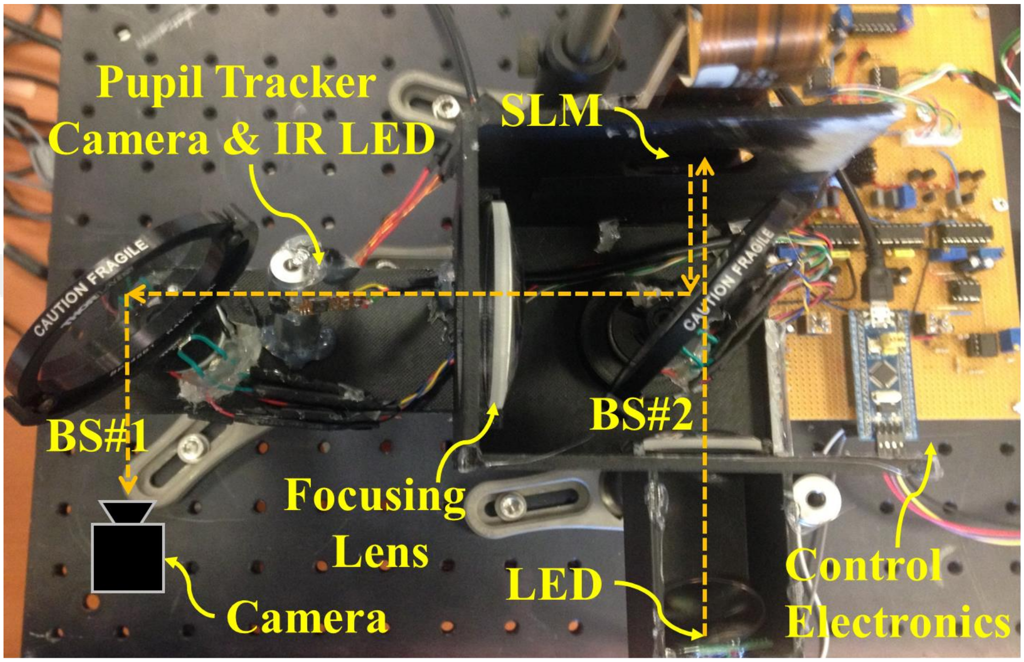

Figure 4.16. The experimental setup.

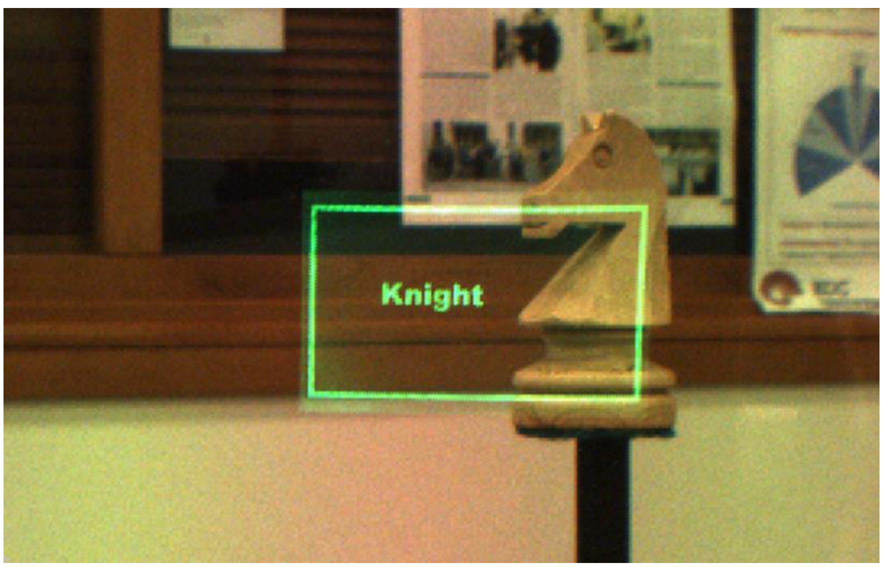

Figure 4.17. Holographic image for gaze angle = 15°.

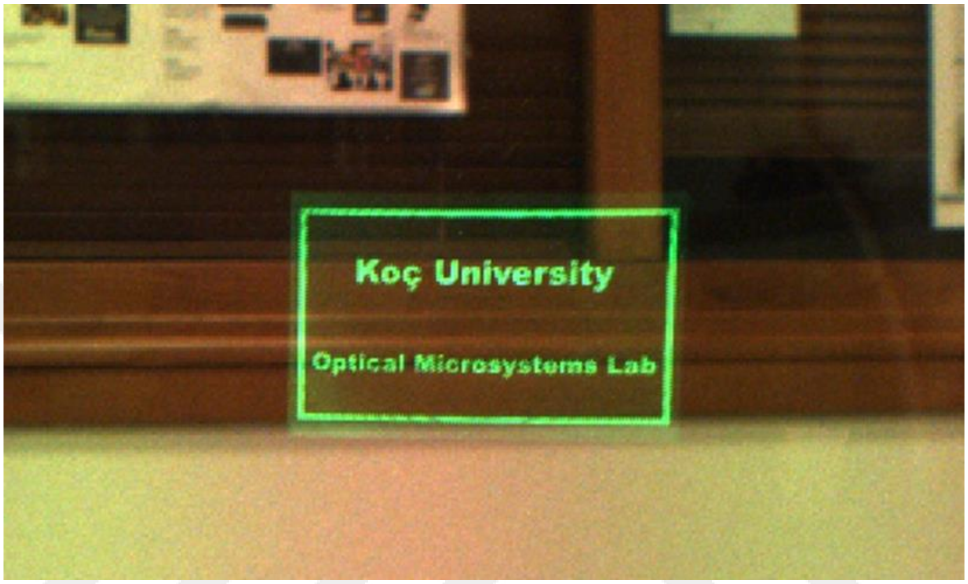

Figure 4.18. Holographic image for gaze angle = 0°.

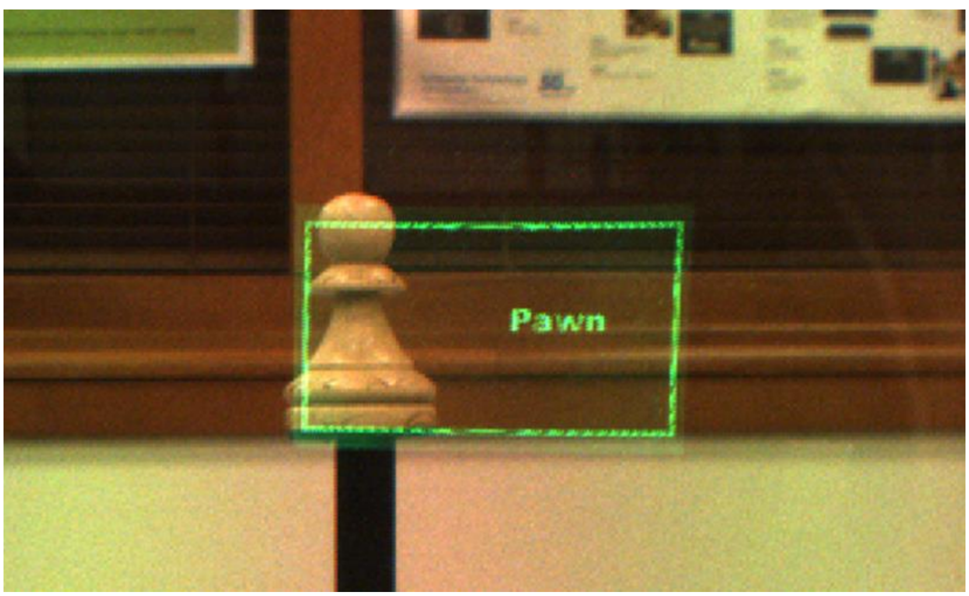

Figure 4.19 Holographic image for gaze angle = -15°.

As the viewer looks at different directions some chess pieces enter the FOV. The name of the chess piece is displayed according to the gaze direction. Figure 4.17, Figure 4.18 and Figure 4.19 show the holographic images for gaze angles 15°, 0° and -15°, respectively. The green rectangular box denotes the instantaneous FOV of 7x4°, which is extended to 37x4° using the rotating beam splitters.

4.6 Conclusion

We successfully demonstrated a foveated holographic near eye display that dynamically steers the limited FOV of a small SLM within the larger FOV of the user, always aligning it to the central vision to provide a high resolution image to the fovea. With this architecture we were able to extend the FOV of the holographic display to 37x4° with an SLM that can provide only 7x4°.The system utilizes two fast- response servo motors that rotate the beam-splitters mounted on them according to the gaze information provided by a low latency pupil tracker. This ensures the holographic view is always perpendicular to the viewing direction of the user. To our knowledge this is the first demonstration of a foveated display in the literature together with a pupil tracker.

5 FOVEATED HOLOGRAPHIC NEAR-EYE DISPLAY USING THE EYE-CENTRIC ARCHITECTURE

Holographic display is the only technology that can offer true 3D with all the required depth cues. Holographic near-eye displays (HNED) can provide continuous depth planes with the correct stereoscopic disparity for a comfortable 3D experience. Existing approaches for HNEDs have small field-of-view and small exit pupil size, which are limited by the number of pixels on the spatial light modulator. As an example, conventional holographic head-worn display architectures are limited to about 20x10 degrees FOV using a 4K resolution SLM panel and have fixed FOV.

Dynamic foveated displays with a steerable FOV across the visual field are desired. Proposed architectures require multiple moving components, which are not practical for head-worn displays due to speed, size, and power requirements. We present a new optical architecture that can overcome those limitations and substantially extend the FOV supported by the SLM. Our architecture automatically follows the gaze of the viewer's pupil without any moving parts. Moreover, it mimics human vision by providing varying resolution across the FOV resulting in better utilization of the available space-bandwidth product of the SLM.

We achieved 28x28 degrees instantaneous FOV within an extended FOV of 60x40 degrees using a 4K SLM, effectively providing a total enhancement of >3x in instantaneous FOV area, >10x in extended FOV area and the space-bandwidth product.

5.1 Eye-centric HMD Architecture

Head-worn displays (HWDs) have been gathering more and more attention over the last decade, especially due to the increasing popularity of augmented reality and virtual reality applications [70]. Majority of HWDs are fixed focus stereoscopic systems [71], [72], which results in a mismatch between the accommodation (focus) and vergence (rotation of the eyes to maintain single binocular vision) responses and inevitably leads to viewing discomfort [73], [74].

Holographic HWDs, on the other hand, show computer generated holograms (CGHs) with the correct perspective and all the natural depth cues to each eye by emulating the wavefront pattern that would be emitted from the displayed 3D objects [75], [76]. As a result, the user can focus directly on the gazed 3D object, eliminating the discomfort caused by the vergence-accommodation conflict. In holographic HWDs, CGHs are typically displayed on phase-only spatial light modulators (SLMs) [77]. The need for relay optics is not present for such displays, since the SLM can be imaged to an arbitrary distance away from the eye [68].

Despite their great potential, current holographic HWDs suffer from field-of-view and eyebox (exit pupil) limitations, due to the limited pixel counts of currently available SLMs. Total pixel count of the SLM puts an upper limit on the space-bandwidth product (SBP) of the system [78]-[81]. To alleviate the SBP limitations, holographic displays can utilize pupil tracking and deliver the object waves through two small eyeboxes around the eye pupil, which maximizes the FOV attainable from the system [82]. State-of-the-art SLMs can have resolutions of up to 4K (3840 horizontal and 2160 vertical pixels), a display designed with such an SLM would have a limited SBP (= product of FOV and eyebox size) of 100 deg.mm in the horizontal axis. As an example, one can obtain a FOV of 20 degrees and an eyebox size of 5 mm. A FOV of 20 degrees is small for a true AR experience and a 5 mm static eyebox is also small for a comfortable viewing experience using a binocular HWD [1]. In order to match human vision capabilities, one might desire a FOV of 80 degrees and an eyebox size of 15 mm, which will require an SLM with pixel count that is in the order of 50,000 pixels in the horizontal axis (more than gigapixels in total). Such an SLM is beyond the capabilities of current technology and would be overkill from the system design perspective. Various methods have been attempted to increase the eyebox size and the FOV simultaneously with state-of-the-art SLMs, including time multiplexing [83], [84] and using multiple SLMs for spatial multiplexing [85]-[87]. Despite their advantages over using a single SLM, these approaches result in complex and high-cost systems.

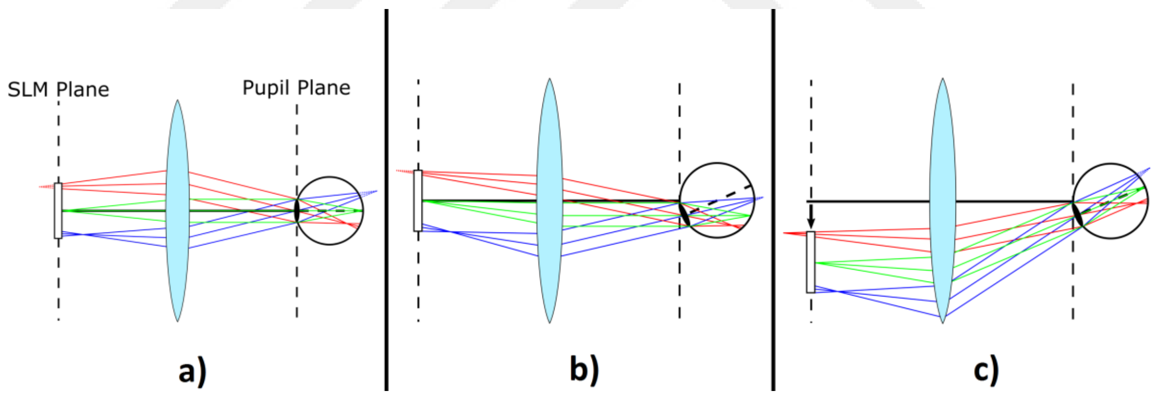

Figure 5.1 If the eye rotates, the SLM image shifts to the peripheral vision. SLM movement is required to shift the image back to fovea.

Since it is not currently possible to rival the FOV of human vision using holographic displays, one solution is to implement a foveated display where only the CGH for the gazed object is being generated and the peripheral image is displayed with a low-resolution microdisplay [81]. Another possibility is to combine a travelling microdisplay with a wide field-of-view peripheral display and enable natural focus depth using either a light field or a multifocal/varifocal approach [88]. Various methods have been attempted to steer the

FOV from one region to another, which generally involve utilizing motorized optical components. Such solutions suffer from actuator size and synchronization issues between multiple dynamic elements, as it is not possible to steer the FOV with a single dynamic component.

In conventional holographic displays, steering the FOV (i.e., keeping the image centered at the fovea as the eye rotates) is not possible by just changing the CGH. As illustrated in Figure 5.1, eye rotation causes the displayed image to shift towards the peripheral vision. SLM or lenses need to be moved mechanically to bring the image onto the fovea.

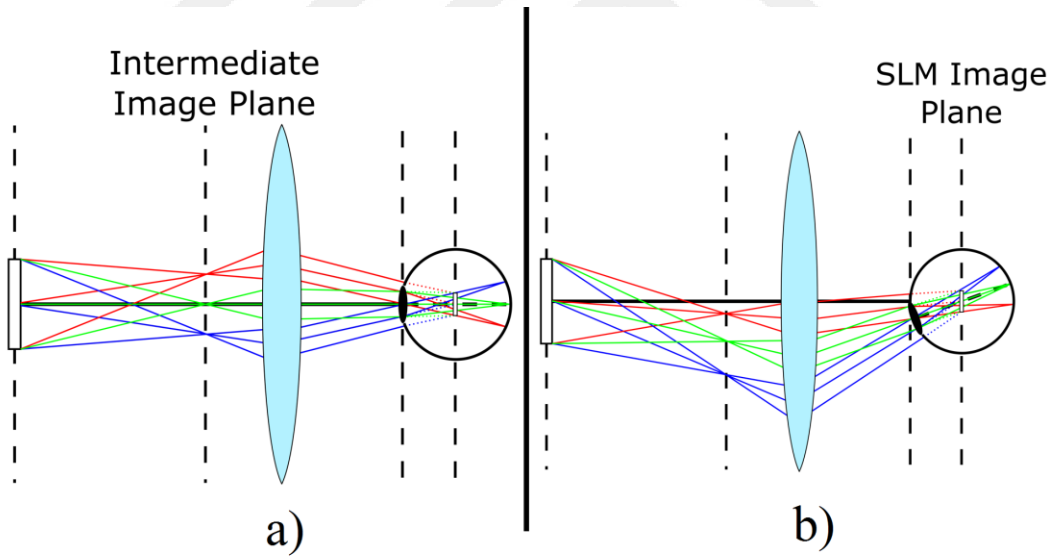

Figure 5.2. In our eye-centric design the SLM is imaged at the rotation center of the eye projects a holographic image to the retina. e) If the eye rotates, light from the SLM still enters through the pupil and always falls on the fovea.

Imaging the SLM at the rotation center of the eye, which we call the eye-centric design, is at the core of our proposed architecture. Since the SLM is imaged at the rotation center of the eye, changing gaze directions are handled by changing the direction of rays via CGH as illustrated in Figure 5.2. Direction of the rays is altered by adding diffractive lens terms and grating terms on the CGH without any moving components. In essence, a demagnified SLM image at the center of the eye projects the holographic image onto the fovea and the eye rotations are handled by adding tilt terms to the CGH.

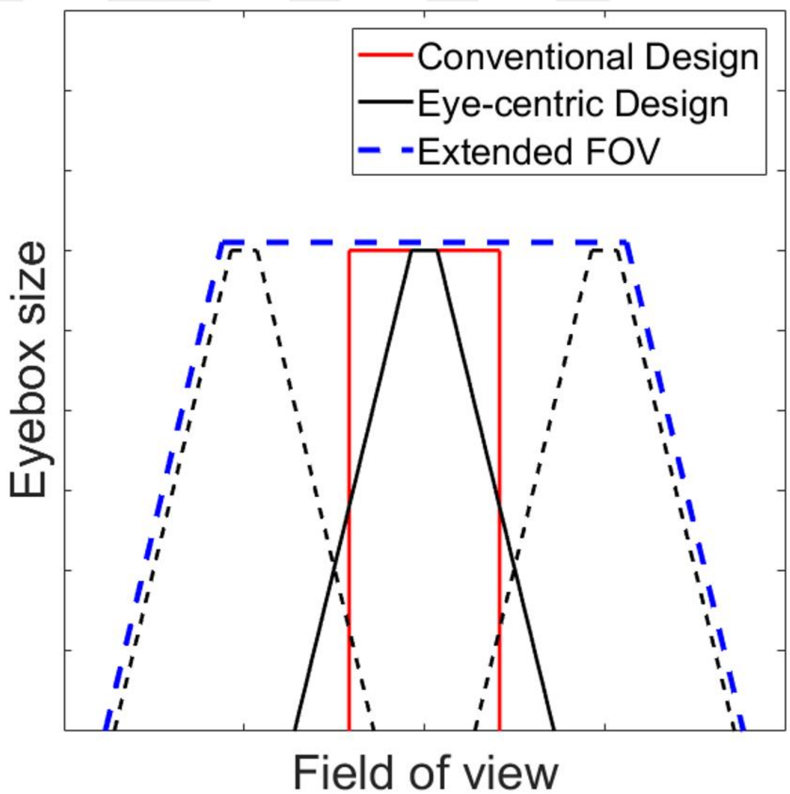

Figure 5.3. Eyebox size vs. FOV curve for conventional and eye-centric holographic displays.

Conventional displays have fixed FOV and eyebox size, therefore fixed spatial resolution across the FOV. In the eye-centric design, the eyebox size decreases towards the edges of the instantaneous FOV due to vignetting effects, which results in degrading resolution away from the foveal vision. As the instantaneous FOV follows the pupil, an extended FOV is achieved as shown in Figure 5.3.

The eye-centric design has two major advantages compared to conventional holographic HWD architectures: i) Instantaneous FOV can be digitally steered by only modifying the CGH to follow the gaze, providing a natural foveated display with no moving parts. ii) The extended FOV is much larger than what is achievable with conventional holographic HWDs.

5.2 Design and Simulations

The eye-centric design can be realized using different optical components, as illustrated from Figure 5.4 to Figure 5.6. The key point is to image the center of the SLM to the rotation center of the eye. This can be achieved by using a flat holographic optical element (HOE) in front of the eye that can be optimized for small form factor. With HOEs color correction is a challenge with wide FOV so achieving full color displays is difficult. Figure 5.5 shows an alternative design using a section of an ellipsoid as the combiner element. An SLM that is placed at one of the foci of the ellipsoid is imaged at the second focus of the ellipsoid. This is a simpler solution, but the magnification is not constant across the FOV. Additional imaging optics can be used to design a more compact system with balanced magnification as illustrated in Figure 5.6.

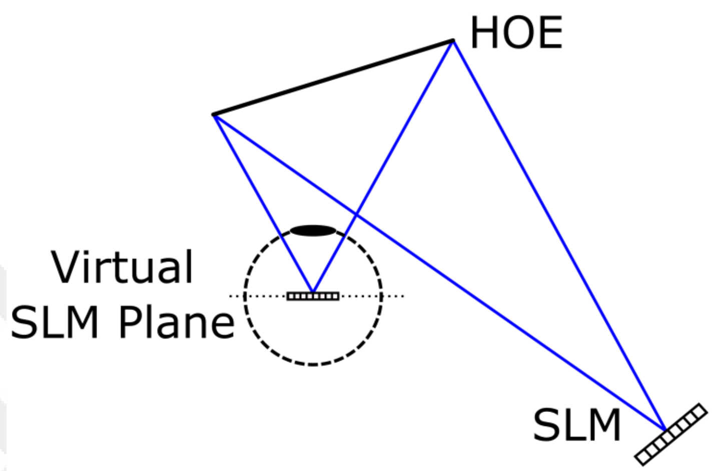

Figure 5.4. Eye-centric design can be implemented using a holographic optical element that images the SLM to the rotation center of the eye.

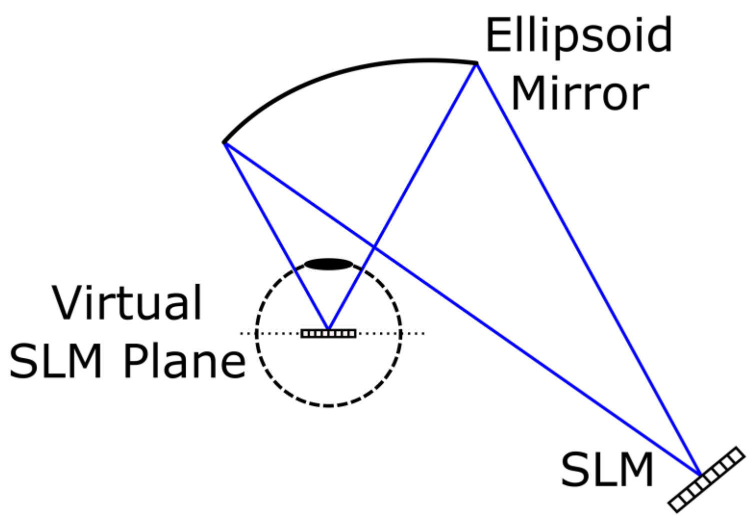

Figure 5.5. Using a section of a reflective ellipsoid is a simple alternative to HOEs, with no chromatic deviations in the design.

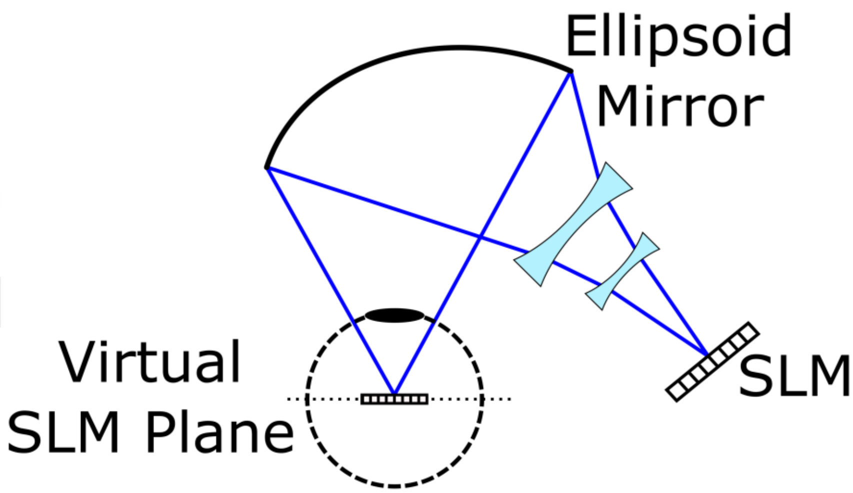

Figure 5.6. Additional optics can be used to balance the non-uniform magnification of the ellipsoid.

Magnification (M) is one of the key parameters of the ellipsoid for our display. Smaller magnification brings larger eyebox and FOV, but high enough magnification is needed for sufficient separation of the diffraction orders due to the pixelated structure of the SLM, which results in a small eyebox and small FOV. Therefore, an optimum point should be selected for a given SLM and desired display parameters. In our design we chose M = 4. Te magnification is defined as the inverse of the ratio of the distance from the eye center to the ellipsoid in y-direction (50mm) and from that point to the distance to center of the SLM (200mm) in Figure 5.7. The a,b,c parameters of the ellipsoid are 125mm, 86.96mm and 86.96mm, respectively.

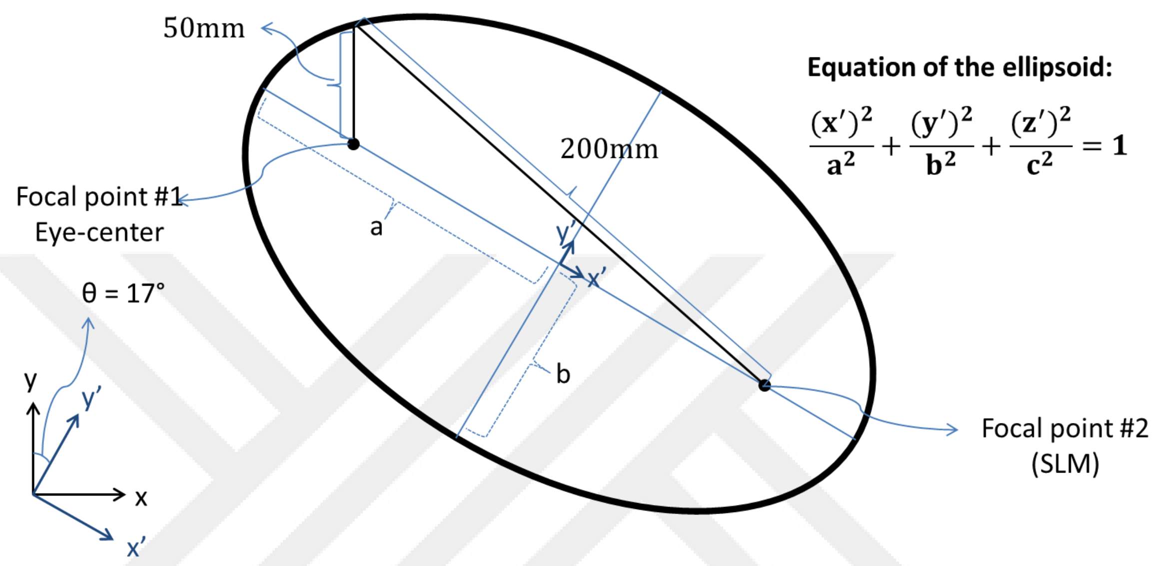

Figure 5.7. Ellipsoid parameters of our design.

We modeled and simulated the ellipsoid described above in Zemax as seen in Figure 5.8 to Figure 5.10. Different gaze angles from -25° to 25° are simulated. The blue rays show the central vision, red and blue rays show the edges of the instantaneous FOV. Due to the non-uniform magnification across the aperture of the ellipsoid, the instantaneous FOV varies; getting larger from nasal to temporal FOV. The full color eyeboxes for each gaze angle is shown in the corresponding figures on the right. The colors show the actual color of the diffraction orders due to the pixelated structure of the SLM. The circle in the middle shows the eye pupil with 3mm diameter. As seen in the simulations the eyebox is sufficiently large and no diffraction orders enter the eye.

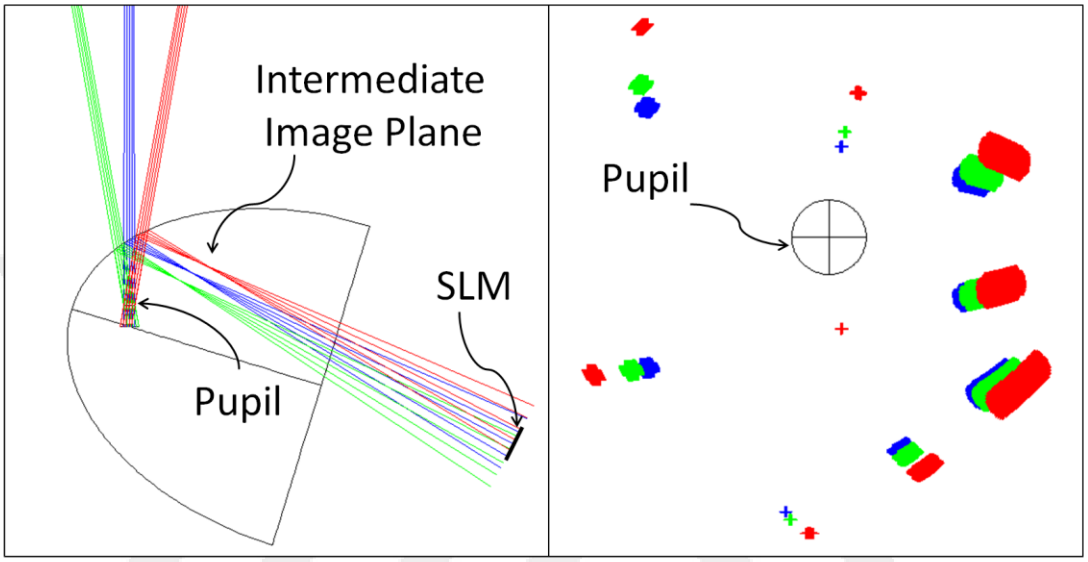

Figure 5.8. Zemax simulation of the ellipsoid as an eye-centric display implementation. On the left the rays reaching the SLM for different object points and the intermediate image plane are shown. On the right a 3mm pupil in the eyebox and the diffraction orders are seen for gaze = 0°.

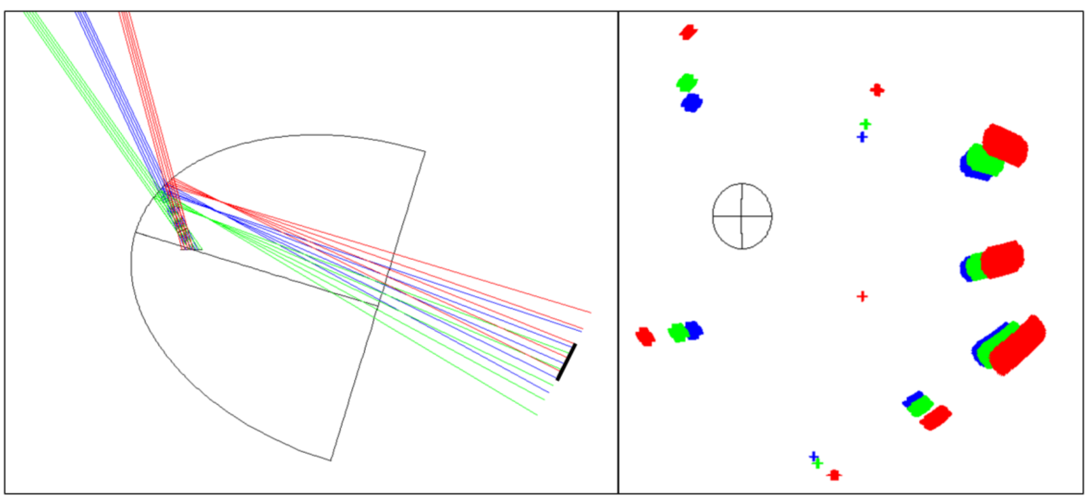

Figure 5.9. Zemax simulation for gaze = -25°.

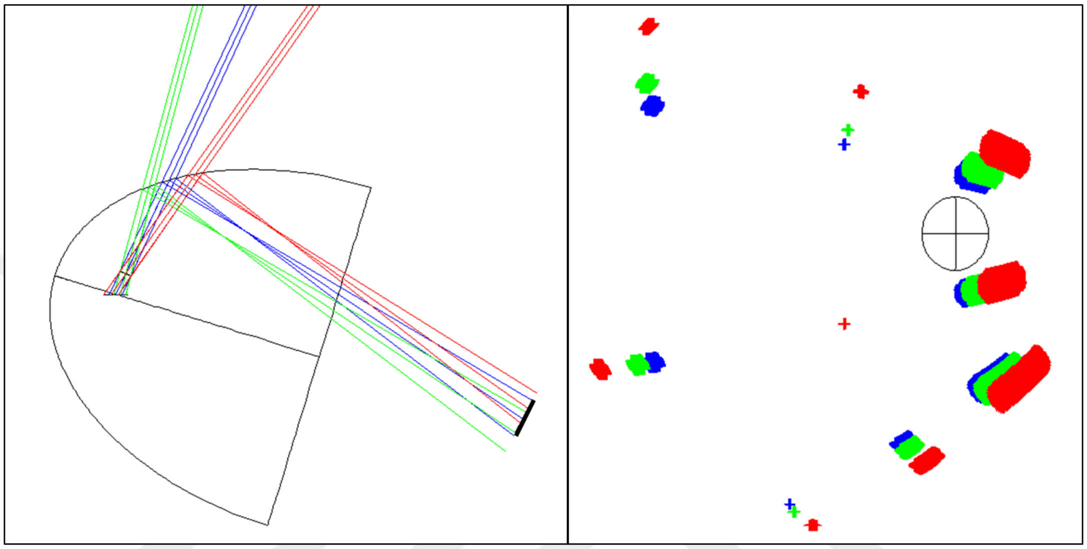

Figure 5.10. Zemax simulations for gaze = 25°.

5.3 Experimental Results

In our experiments, we used Holoeye GAEA as the SLM, which is a 4K (3840x2160 pixels) LCoS phase modulator chip with 3.74 µm pixel pitch. The light source is a LASOS MCS4 series 3 wavelength fiber coupled laser with wavelengths of 473 nm, 515 nm and 639 nm for blue, green and red colors, respectively. We cut a section of the ellipsoid that gives 60° horizontal and 40° vertical FOV. The part is fabricated using diamond turning on aluminum substrate, as shown in Figure 5.11.

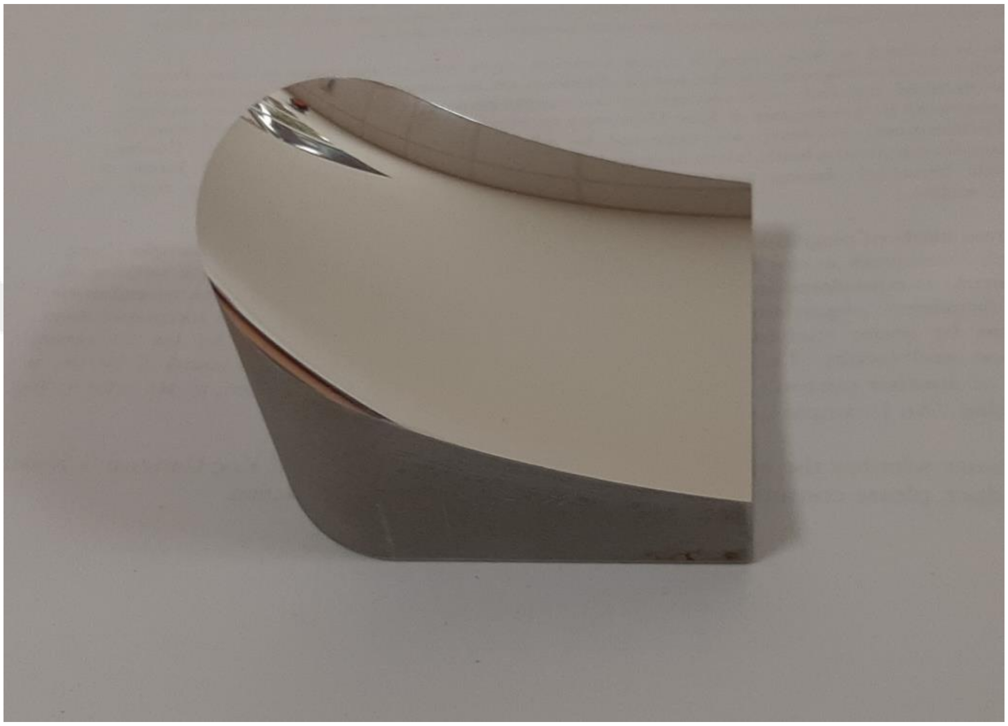

Figure 5.11. Fabricated ellipsoid mirror.

To compute the CGHs the 3D scene is modeled as a set of luminous points, similar to methods where 3D objects are represented by point clouds [91]-[93], and the hologram corresponding to the entire scene is generated by superposing the holograms for the individual points. The hologram for a single point is computed with an algorithm based on ray-tracing, which makes use of Zernike polynomials to estimate the wavefront exiting the SLM [94]-[96]. As a final step, the iterative Fourier transform algorithm is employed for phase encoding [69], [97].

Figure 5.12 illustrates the experimental setup. In the optical setup, the RGB laser beam out of a single mode fiber is collimated by a lens and the collimated beam is reflected towards the SLM by a pellicle beam splitter to avoid ghost images. The incident beam on the SLM is modulated by the CGH and reflected towards the ellipsoid. The ellipsoid creates the Fourier plane at the eye pupil plane and the diffraction orders are filtered-out by the pupil. The ellipsoid also images the SLM to the rotation center of the eye and a holographic image forms on the retina. A pupil tracker camera measures the pupil position and the CGH on the SLM is updated accordingly.

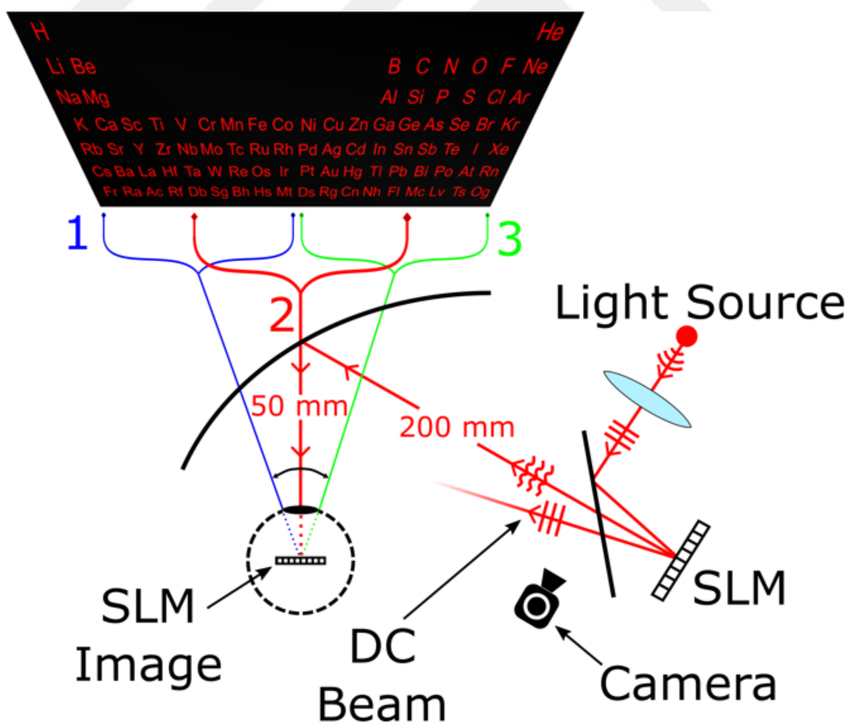

Figure 5.12. Illustration of the optical setup.

Figure 5.13 shows the experimental setup on the optical bench. As the fabricated ellipsoid is not transparent, a true augmented reality demonstration could not be made. In order to provide the peripheral image, we inserted a beam splitter between the eye and the ellipsoid and showed the low-resolution peripheral image on an LCD screen at 10 cm from the eye location without using any magnifier lenses.

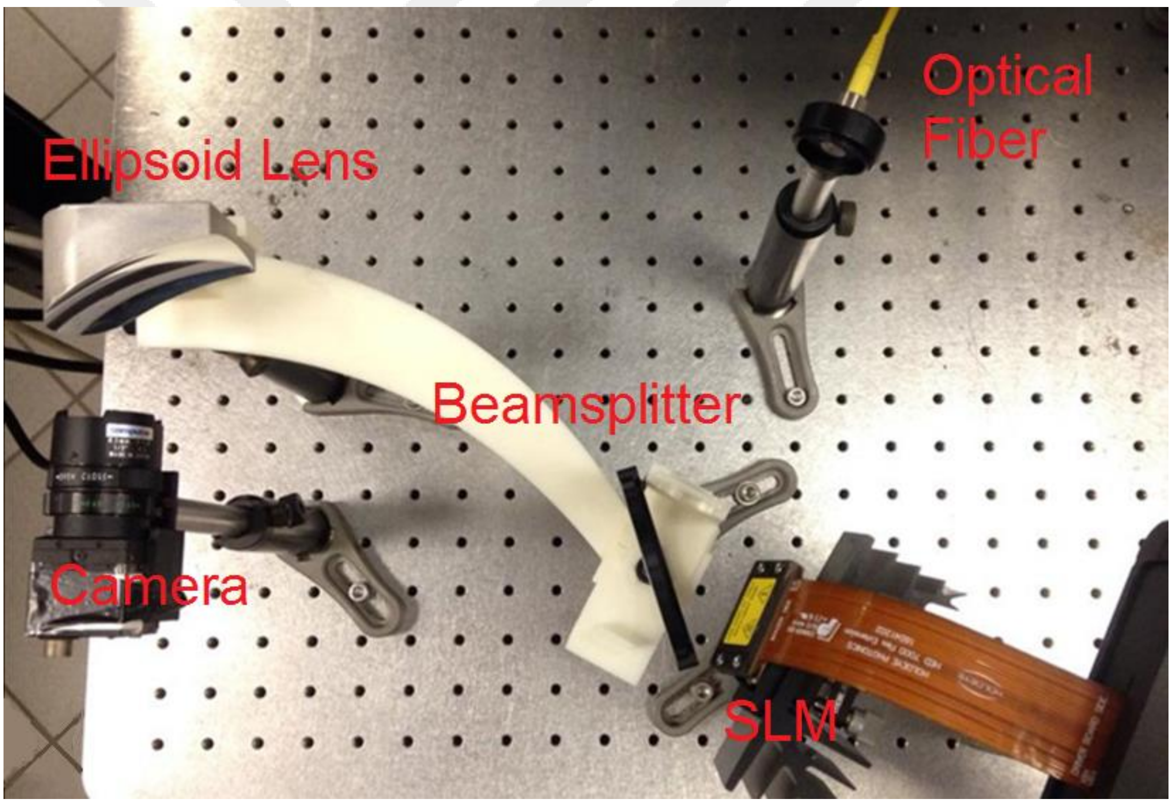

Figure 5.13. Experimental setup on the optical bench

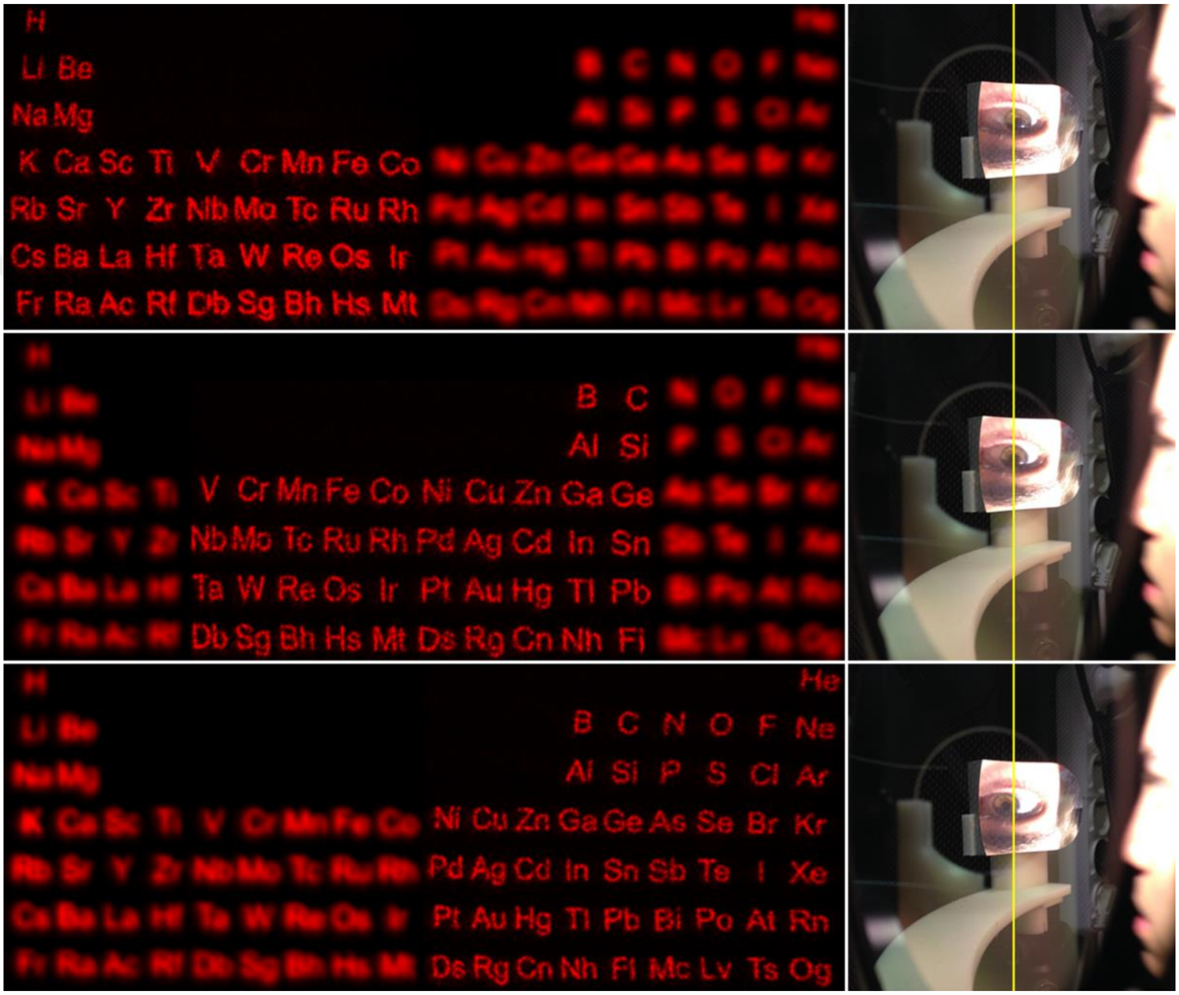

Figure 5.14. Experimental results of the eye-centric foveated holographic display. The periodic table is displayed by the SLM. As the eye rotates, a high-quality holographic view of different regions of the image is seen.

Figure 5.14 shows the experimental results for our foveated display with no moving parts. A low resolution image of the periodic table is displayed on the peripheral display at all times. The high resolution image of the viewed section is projected onto the fovea by updating the CGH on the SLM. The gaze angle is measured by a pupil tracker camera and the holograms are updated accordingly to steer the projected image. As the eye rotates, the image on the fovea remains high-resolution at all times and the rest of the image is blurred, mimicking human vision. Note the shift of pupil center with respect to the yellow reference line due to eye rotation. Despite the step change between high and low resolution regions, the human eye sees a continuous transition due to the receptor cell density variation on the retina.

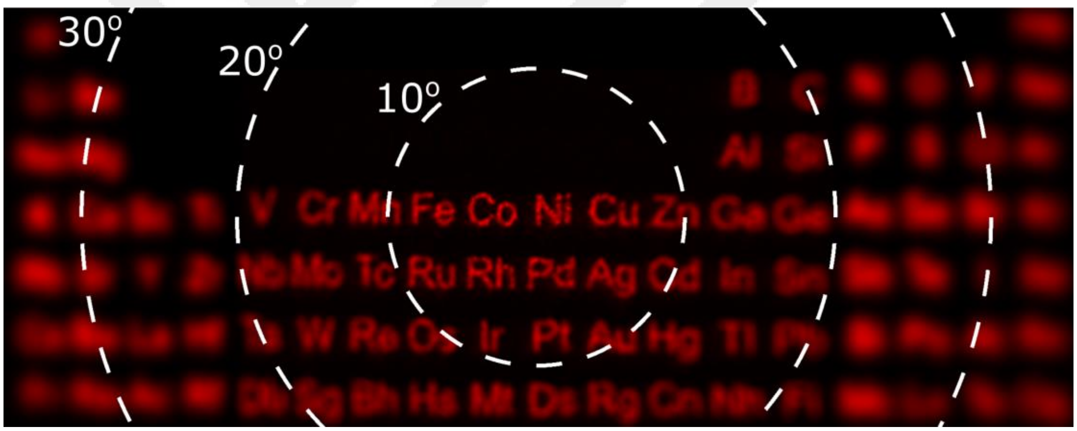

Figure 5.15. Simulation of the perceived image by the human eye. The white circles show the FOV of the eye.

Human vision was also simulated for one of the images to show the smooth transition between the high and low resolution regions, where only the resolution degradation of the human eye was taken into consideration as seen in Figure 5.15. The minimal resolvable angle size was assumed to be linearly increasing with eccentricity, which is a commonly used approximation in both vision and computer graphics [89], [90]. The simulation results show that the difference between the regions generated by the holographic and the peripheral displays is not completely eliminated, but it is not as severe as the difference observed in the camera images.

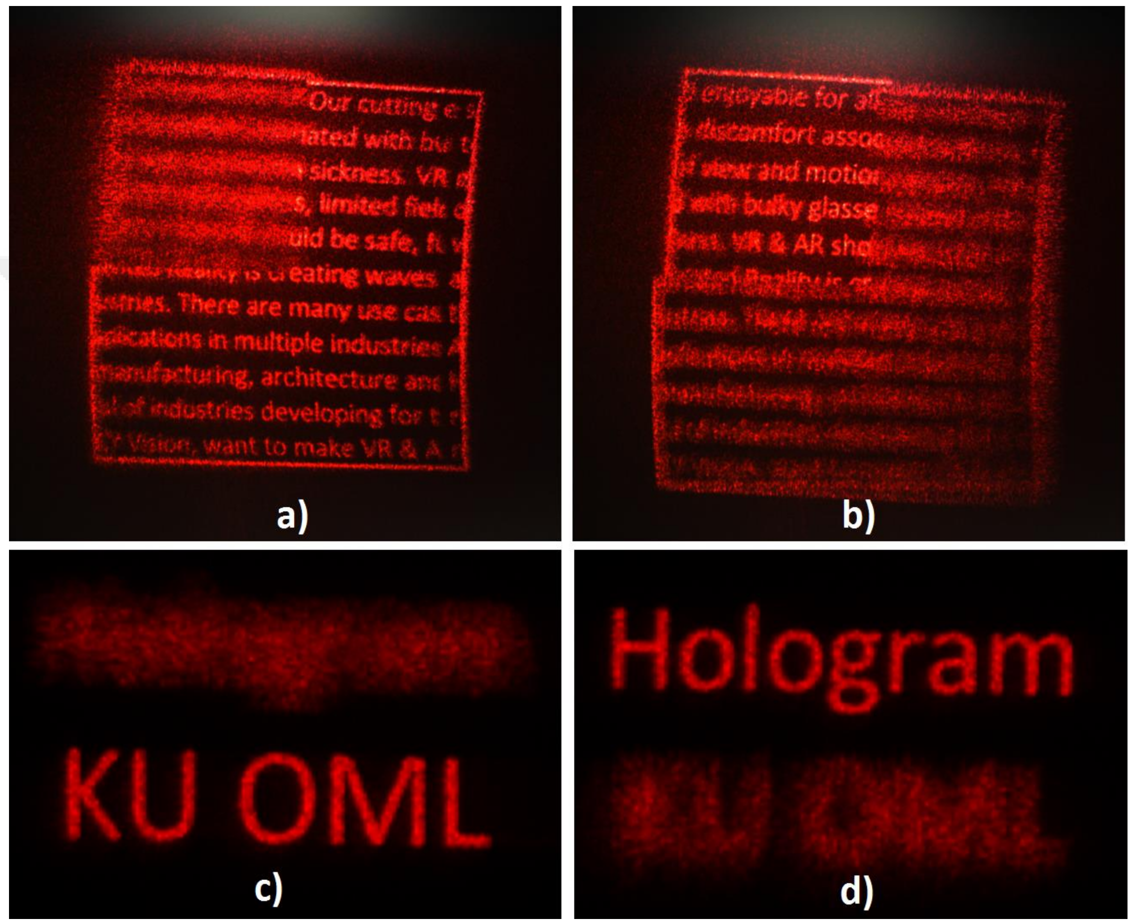

Figure 5.16. Our holographic foveated display provides continuous depth with correct focus blur.

Figure 5.16 demonstrates the capability of providing true depth information of our foveated holographic display. Objects are displayed at different depths so that only the gazed depth appears sharp, other depths appear blurred due to expected focus blur effect. Different sections of the text are displayed at different depths. In a) and b), the upper-left section of the text is displayed at 100 cm and the rest of the text is displayed at 25 cm. As the camera focus is changed, different regions appear sharp or blurred accordingly. Similarly in c) and d), top and bottom rows are displayed at 25 cm and 100 cm, respectively. Note that coherent blur appears sharper in camera images and smoother to the eye.

We can also display color holograms by time-sequentially updating the CGH on the SLM and turning on the correct light source as seen in Figure 5.17. Holographic images under monochromatic illumination of wavelengths 639 nm, 515 nm, 473 nm are shown in images a) to c), respectively. Full color image with time-sequential illumination of RGB wavelengths is shown in d).

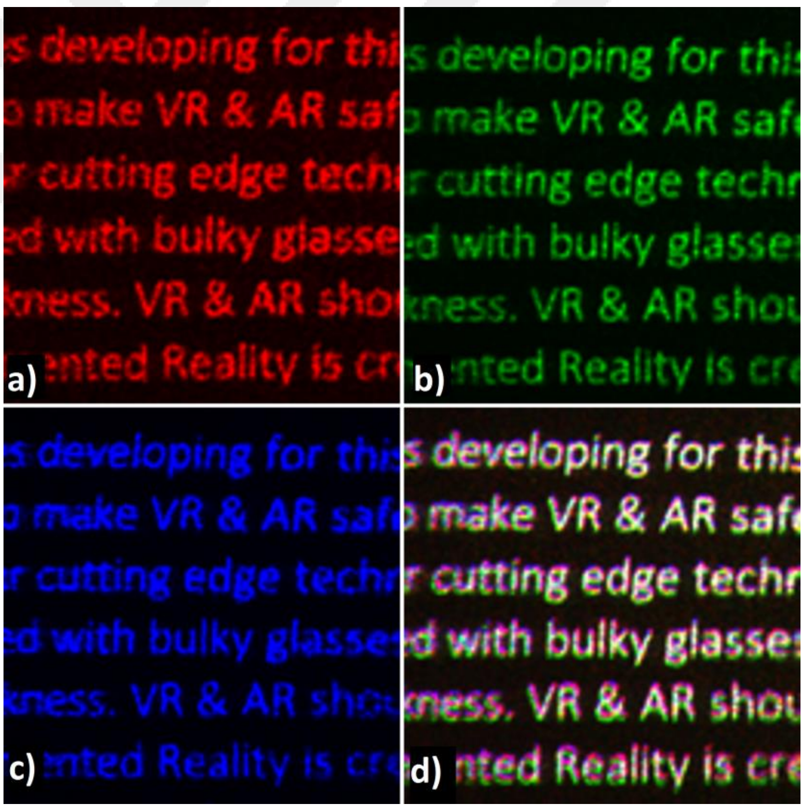

Figure 5.17. The full-color holographic demonstration.

5.4 Conclusion

In this work, we proposed the eye-centric approach for 3D holographic HWDs, which makes it possible to steer the instantaneous FOV within a larger extended FOV without using any moving parts or dynamic optical components. Given a reflective phase-only SLM, we have developed a design procedure for an eye-centric holographic HWD and described an algorithm to compute holograms for any optical setup as discussed in detail in the supplementary material. The experimental results verify that the proposed system is able to display 3D images in a wide, steerable FOV. We achieved 28° instantaneous FOV within an extended FOV of 60x40 degrees using a 4K SLM.

6 CONCLUSIONS and FUTURE WORK

In this thesis we present three different head-worn augmented reality display architectures to overcome the space-bandwidth product limitations of the SLMs. Our architectures exploit the spatial degradation of the natural human vision from central to peripheral vision. By tracking the pupil position in real time using our fast and reliable algorithm described in Chapter 2, high resolution images that can only be created with small FOV and small eyebox are provided over a large extended FOV and eyebox.

In Chapter 3, we presented our novel technique for extending the eyebox in head-worn displays using a pupil tracker and an array of light sources, which we call the pupil follower. We demonstrated the pupil follower concept with the pinhole imaging based head-worn AR display. Our architecture alleviates the problem of the human eye being unable to directly resolve near-to-eye displays. The proposed system counters the small eyebox problem arising from the pinhole imaging approach by extending the effective eyebox with a pupil follower with only 11msec motion-to-photon latency. The pupil follower also creates a super light efficient display since nearly all light emanating from the source enters the eye, making it suitable for mobile applications. The prototype achieved 37° circular FOV with a luminance of 360 cd/m^2 using an LED with only 0.42 lumen output. The MTF cutoff frequency for the display system was measured to be approximately 2 cyc/deg. Good quality experimental results for a real use case were observed on a prototype setup with visually undetectable motion-to-photon latency. Pupil follower concept can be applicable to other HMD architectures such as holographic displays and foveated displays; therefore it will be of interest to a broader audience.

In Chapter 4, we demonstrated a foveated holographic near eye display that dynamically steers the limited FOV of a small SLM within the larger FOV of the user, always aligning it to the central vision to provide a high resolution image to the fovea. With this architecture we were able to extend the FOV of the holographic display to 37x4° with an SLM that can provide only 7x4°.The system utilizes two fast- response servo motors that rotate the beam-splitters mounted on them according to the gaze information provided by a low latency pupil tracker. This ensures the holographic view is always perpendicular to the viewing direction of the user. To our knowledge this is the first demonstration of a foveated display with a pupil tracker in the literature.

In Chapter 5, we proposed the eye-centric approach for 3D holographic HWDs, which make it possible to steer the instantaneous FOV within a larger extended FOV without using any moving parts or dynamic optical components. Given a reflective phase-only SLM, we have developed a design procedure for an eye-centric holographic HWD and described an algorithm to compute holograms for any optical setup as discussed in detail in the supplementary material. The experimental results verify that the proposed system is able to display 3D images in a wide, steerable FOV.

In the future the pupil tracker algorithm can further be improved for increased reliability and speed. With our current configuration the algorithm should be able to yield 100 fps, but due to camera frame rate limitations we were able to demonstrate only 30 fps. To do this, faster cameras should be acquired and the necessary Linux camera drivers should be written for BeagleBone.

With the pinhole display the FOV can be improved by designing a custom focusing lens that has a shorter focal length and larger diameter. Proper LCD driving scheme is also necessary for updating the image in real time.

We demonstrated our rotating beam splitters setup with 1-axis actuators. 2-axis actuators should be developed to extend the FOV in two dimensions. Furthermore the optics can be built compacter by custom lens design. Moving parts in a display is not desirable, therefore reducing the number of actuators and elimination the rotating beam splitter in front of the eye should be eliminated. A full color holographic demonstration should also be considered for future work. In our demonstration a low-resolution peripheral display was missing, which can be included in the future.

With our eye-centric display demonstration the main drawback was the aluminum ellipsoid in front of the eye, so an augmented reality demonstration was not possible. A semi-reflective ellipsoid or an HOE should be fabricated in the future. In our setup the eyebox was stationary; it can be extended with an array of light sources as demonstrated in Chapter 3. Real-time hologram computation algorithms should also be further developed.

BIBLIOGRAPHY

[1] https://lumusvision.com/

[2] https://moverio.epson.com/

[3] Rolland, Jannick P., et al. "See-through head-worn display (HWD) architectures." Handbook of Visual Display Technology(2016): 1-32.

[4] https://www.kguttag.com/2018/10/22/magic-leap-hololens-and-lumus-resolution-shootout-ml1-review-part-3/

[5] https://www.epson.com.tr/products/see-through-mobile-viewer/moverio-bt-300

[6] https://hololens.reality.news/news/interview-microsoft-hololens-2-team-speaks-inside-specs-design-future-enterprise-augmented-reality-0194565/

[7] https://commons.wikimedia.org/wiki/File:Google_Glass_Front.jpg

[8] https://techcrunch.com/2017/07/18/miras-prism-is-a-99-headset-vying-to-become-the-google-daydream-of-augmented-reality/

[9] https://www.theverge.com/2017/7/18/15948700/mira-prism-iphone-augmented-reality-headset-hands-on-announce

[10] Wang, J., Liang, Y., & Xu, M. (2015). Design of a see-through head-mounted display with a freeform surface. Journal of the Optical Society of Korea, 19(6), 614-618.

[11] Wei, L., Li, Y., Jing, J., Feng, L., & Zhou, J. (2018). Design and fabrication of a compact off-axis see-through head-mounted display using a freeform surface. Optics express, 26(7), 8550-8565.

[12] Chen, B., & Herkommer, A. M. (2017). Alternate optical designs for head-mounted displays with a wide field of view. Applied optics, 56(4), 901-906.

[13] Arthur, J. T. J., Bailey, R. E., Williams, S. P., Prinzel, L. J., Shelton, K. J., Jones, D. R., & Houston, V. E. (2017). Review of head-worn displays for the next generation air transportation system. Optical Engineering, 56(5), 051405.

[14] Maimone, A., Lanman, D., Rathinavel, K., Keller, K., Luebke, D., & Fuchs, H. (2014, July). Pinlight displays: wide field of view augmented reality eyeglasses using defocused point light sources. In ACM SIGGRAPH 2014 Emerging Technologies (p. 20). ACM.

[15] http://www.holoeyesystems.com/lcos-microdisplays/

[16] http://holoeye.com/lcos-microdisplays/

[17] https://www.electronics-lab.com/5900ppi-full-hd-0-37-lcos-micro-display-measures-23-4x8-65mm/

[18] https://www.laserfocusworld.com/optics/article/16552226/picoprojection-displays-laserlcos-microdisplays-make-for-tiny-lowcost-picoprojectors

[19] https://www.researchgate.net/figure/Two-operational-states-of-the-DMD-chip-17_fig36_315669635

[20] https://www.digikey.in/product-detail/en/texas-instruments/DLP4710FQL/296-42272-5-ND/5320159#images

[21] http://en.olednet.com/microdisplay-emagin/

[22] https://www.sony-semicon.co.jp/e/products/microdisplay/oled/technology.html

[23] https://www.smart2zero.eu/news/lemoptix-pico-projector-excels/page/0/1

[24] Urey, H. (2003). Retinal scanning displays. Encyclopedia of Optical Engineering, 3, 2445-2457.

[25] Moon, E., Kim, M., Roh, J., Kim, H., & Hahn, J. (2014). Holographic head-mounted display with RGB light emitting diode light source. Optics express, 22(6), 6526-6534.

[26] Chen, Z., Lin, Q., Li, J., Yu, X., Gao, X., Yan, B., ... & Xie, S. (2017). A see-through holographic head-mounted display with the large viewing angle. Optics Communications, 384, 125-129.

[27] Makowski, M. (2019). Experimental Aspects of Holographic Projection with a Liquid-Crystal-on-Silicon Spatial Light Modulator. In Holographic Materials and Optical Systems. IntechOpen.

[28] https://holoeye.com/gaea-4k-phase-only-spatial-light-modulator/

[29] https://uploadvr.com/tobii-foveated-rendering/

[30] Koretz, Jane F., and George H. Handelman. "How the human eye focuses." Scientific American 259.1 (1988): 92-99.

[31] G. Wyszecki, W. Stiles, Color Science: Concepts and Methods, Quantitative Data and Formulae, John Wiley & Sons, New York, 1982

[32] Koretz, Jane F., and George H. Handelman. "Modeling age-related accomodative loss in the human eye." Mathematical modelling 7.5-8 (1986): 1003-1014.

[33] Yang, Jianming, et al. "Method of achieving a wide field-of-view head-mounted display with small distortion." Optics letters 38.12 (2013): 2035-2037.

[34] Song, Weitao, et al. "Design and assessment of a wide FOV and high-resolution optical tiled head-mounted display." Applied optics 54.28 (2015): E15-E22.

[35] Romanova, G. E., A. V. Bakholdin, and V. N. Vasilyev. "Optical schemes of the head-mounted displays." Optical Modeling and Performance Predictions IX. Vol. 10374. International Society for Optics and Photonics, 2017.

[36] Choi, Sungwon, Yuzuru Takashima, and Sung-Wook Min. "Improvement of fill factor in pinhole-type integral imaging display using a retroreflector." Optics Express 25.26 (2017): 33078-33087.

[37] Yao, Cheng, et al. "Design of an optical see-through light-field near-eye display using a discrete lenslet array." Optics express26.14 (2018): 18292-18301.

[38] Akşit, Kaan, Jan Kautz, and David Luebke. "Slim near-eye display using pinhole aperture arrays." Applied optics 54.11 (2015): 3422-3427.

[39] Westheimer, Gerald. "The Maxwellian View." Vision research 6.11-12 (1966): 669-682.

[40] Inami, Masahiko, et al. "A stereoscopic display with large field of view using Maxwellian optics." Proc. Int. Conf. Artificial Reality and Tele-Exsistance. 1997.

[41] Beer, R. Dirk, Donald IA MacLeod, and Timothy P. Miller. "The Extended Maxwellian View (BIGMAX): A high-intensity, high-saturation color display for clinical diagnosis and vision research." Behavior research methods 37.3 (2005): 513-521.

[42] Takahashi, Hideya, and Shun Hirooka. "Stereoscopic see-through retinal projection head-mounted display." Stereoscopic displays and applications XIX. Vol. 6803. International Society for Optics and Photonics, 2008.

[43] Park, Jae-Hyeung, and Seong-Bok Kim. "Optical see-through holographic near-eye-display with eyebox steering and depth of field control." Optics express 26.21 (2018): 27076-27088.

[44] Travis, Adrian RL, et al. "Wedge guides and pupil steering for mixed reality." Journal of the Society for Information Display 26.9 (2018): 526-533.

[45] Pedrotti, Frank L., and Leno S. Pedrotti. "Introduction to optics 3nd edition." Introduction to Optics 3nd Edition by Frank L. Pedrotti, SJ, Leno S. Pedrotti New Jersey: Prentice Hall, page 69 (1993).

[46] Coley, Gerald. "Beaglebone black system reference manual." Texas Instruments, Dallas (2013).

[47] Goodman, Joseph W. Introduction to Fourier optics. Roberts and Company Publishers, 2005.

[48] Siegman, Anthony E. "How to (maybe) measure laser beam quality." Diode Pumped Solid State Lasers: Applications and Issues. Optical Society of America, 1998.

[49] Smith, Warren J. Modern optical engineering. Tata McGraw-Hill Education, 1966.

[50] Hedili, M. K., Freeman, M. O., & Urey, H. (2013). Transmission characteristics of a bidirectional transparent screen based on reflective microlenses. Optics express, 21(21), 24636-24646.

[51] Melzer, J. E. (1998, August). Overcoming the field-of-view/resolution invariant in head-mounted displays. In Helmet-and Head-Mounted Displays III (Vol. 3362, pp. 284-294). International Society for Optics and Photonics.

[52] Cheng, D., Wang, Y., Hua, H., & Sasian, J. (2011). Design of a wide-angle, lightweight head-mounted display using free-form optics tiling. Optics letters, 36(11), 2098-2100.

[53] Hoppe, M., & Melzer, J. E. (1999, October). Optical tiling for wide-field-of-view head-mounted displays. In Current Developments in Optical Design and Optical Engineering VIII(Vol. 3779, pp. 146-154). International Society for Optics and Photonics.

[54] Cheng, D., Wang, Y., & Hua, H. (2010, June). Large field-of-view and high resolution free-form head-mounted display. In International Optical Design Conference (p. IMC4). Optical Society of America.

[55] Cheng, D., Wang, Y., Hua, H., & Talha, M. M. (2009). Design of an optical see-through head-mounted display with a low f-number and large field of view using a freeform prism. Applied optics, 48(14), 2655-2668.

[56] Wang, Q., Cheng, D., Wang, Y., Hua, H., & Jin, G. (2013). Design, tolerance, and fabrication of an optical see-through head-mounted display with free-form surface elements. Applied optics, 52(7), C88-C99

[57] Song, W., Cheng, D., Deng, Z., Liu, Y., & Wang, Y. (2015). Design and assessment of a wide FOV and high-resolution optical tiled head-mounted display. Applied optics, 54(28), E15-E22.

[58] Gao, H., Xu, F., Liu, J., Dai, Z., Zhou, W., Li, S. & Zheng, H. (2019). Holographic Three-Dimensional Virtual Reality and Augmented Reality Display Based on 4K-Spatial Light Modulators. Applied Sciences, 9(6), 1182.

[59] Karl Guttag, Varjo Foveated Display (Part 1), https://www.kguttag.com/2017/06/26/varjo-foveated-display-part-1/

[60] Curcio, C. A., Sloan, K. R., Kalina, R. E., & Hendrickson, A. E. (1990). Human photoreceptor topography. Journal of comparative neurology, 292(4), 497-523.

[61] Koulieris, G. A., Akşit, K., Stengel, M., Mantiuk, R. K., Mania, K., & Richardt, C. (2019, May). Near-Eye Display and Tracking Technologies for Virtual and Augmented Reality. In Computer Graphics Forum (Vol. 38, No. 2, pp. 493-519).

[62] Foi, A., & Boracchi, G. (2016). Foveated nonlocal self-similarity. International Journal of Computer Vision, 120(1), 78-110.

[63] Kim, J., Jeong, Y., Stengel, M., Akşit, K., Albert, R., Boudaoud, B., ... & Shirley, P. (2019). Foveated AR: dynamically-foveated augmented reality display. ACM Transactions on Graphics (TOG), 38(4), 99.

[64] M.E. Lucente, Interactive Computation of Holograms Using a Look-up Table, J. Electron. Imag. 2 (1), 28–34 (1993)

[65] S.-C. Kim and E.-S. Kim, Effective Generation of Digital Holograms of Three-dimensional Objects Using a Novel Look-up Table Method, Appl. Opt. 47 (19), D55–D62 (2008).

[66] L. Ahrenberg, P. Benzie, M. Magnor and J. Watson, Computer Generated Holograms from Three Dimensional Meshes Using an Analytic Light Transport Model, Appl. Opt. 47 (10), 1567–1574 (2008).

[67] D. Mengu, E. Ulusoy and H. Urey, Non-iterative Phase Hologram Computation for Low Speckle Holographic Image Projection, Opt. Express 24, 4462–4476 (2016).

[68] Kazempourradi, S., Ulusoy, E., & Urey, H. (2019). Full-color computational holographic near-eye display. Journal of Information Display, 20(2), 45-59.

[69] J.R. Fienup, Iterative Method Applied to Image Reconstruction and to Computer-generated Holograms, Opt. Eng. 19 (3), 193297–193297 (1980).

[70] Rolland, J. & Cakmakci, O. Head-Worn Displays: The Future Through New Eyes. Opt. Photonics News (2009). doi:10.1364/opn.20.4.000020

[71] Kress, B. & Starner, T. A review of head-mounted displays (HMD) technologies and applications for consumer electronics. in *Photonic Applications for Aerospace, Commercial, and Harsh Environments IV* (2013). doi:10.1117/12.2015654

[72] Urey, H., Chellappan, K. V., Erden, E. & Surman, P. State of the art in stereoscopic and autostereoscopic displays. in *Proceedings of the IEEE* (2011). doi:10.1109/JPROC.2010.2098351

[73] Lambooij, M., Fortuin, M., Ijsselsteijn, W. A. & Heynderickx, I. Measuring visual discomfort associated with 3D displays. in *Stereoscopic Displays and Applications XX* (2009). doi:10.1117/12.805977

[74] Hoffman, D. M., Girshick, A. R., Akeley, K. & Banks, M. S. Vergence-accommodation conflicts hinder visual performance and cause visual fatigue. *J. Vis.* (2008). doi:10.1167/8.3.33

[75] Yaraş, F., Kang, H. & Onural, L. State of the art in holographic displays: A survey. *IEEE/OSA Journal of Display Technology* (2010). doi:10.1109/JDT.2010.2045734

[76] Maimone, A., Georgiou, A. & Kollin, J. S. Holographic near-eye displays for virtual and augmented reality. in *ACM Transactions on Graphics* (2017). doi:10.1145/3072959.3073624

[77] Slinger, C., Cameron, C. & Stanley, M. Computer-generated holography as a generic display technology. *Computer (Long. Beach. Calif).* (2005). doi:10.1109/MC.2005.260

[78] Macovski A. Hologram Information Capacity. *J Opt Soc Amer* (1970).

[79] Chen, J. S., Smithwick, Q. Y. J. & Chu, D. P. Coarse integral holography approach for real 3D color video displays. *Opt. Express* (2016). doi:10.1364/oe.24.006705

[80] Agour, M., Falldorf, C. & Bergmann, R. B. Holographic display system for dynamic synthesis of 3D light fields with increased space bandwidth product. *Opt. Express* (2016). doi:10.1364/oe.24.014393

[81] Yu, H., Lee, K., Park, J. & Park, Y. Ultrahigh-definition dynamic 3D holographic display by active control of volume speckle fields. *Nat. Photonics* (2017). doi:10.1038/nphoton.2016.272

[82] Häussler, R., Schwerdtner, A. & Leister, N. Large holographic displays as an alternative to stereoscopic displays. in *Stereoscopic Displays and Applications XIX* (2008). doi:10.1117/12.766163

[83] Liu, Y.-Z., Pang, X.-N., Jiang, S. & Dong, J.-W. Viewing-angle enlargement in holographic augmented reality using time division and spatial tiling. *Opt. Express* (2013). doi:10.1364/oe.21.012068

[84] Sando, Y., Barada, D. & Yatagai, T. Holographic 3D display observable for multiple simultaneous viewers from all horizontal directions by using a time division method. *Opt. Lett.* (2014). doi:10.1364/ol.39.005555

[85] Hahn, J., Kim, H., Lim, Y., Park, G. & Lee, B. Wide viewing angle dynamic holographic stereogram with a curved array of spatial light modulators. *Opt. Express* (2008). doi:10.1364/oe.16.012372

[86] Finke, G., Kozacki, T. & Kujawińska, M. Wide viewing angle holographic display with a multi-spatial light modulator array. in *Optics, Photonics, and Digital Technologies for Multimedia Applications* (2010). doi:10.1117/12.855778

[87] Kozacki, T., Kujawinska, M., Finke, G., Hennelly, B. & Pandey, N. Extended viewing angle holographic display system with tilted SLMs in a circular configuration. *Appl. Opt.* (2012). doi:10.1364/AO.51.001771

[88] Kim, J. *et al.* Foveated AR: dynamically-foveated augmented reality display. *ACM Trans. Graph.* (2019). doi:10.1145/3306346.3322987

[89] Strasburger, H., Rentschler, I. & Jüttner, M. Peripheral vision and pattern recognition: A review. *J. Vis.* (2011). doi:10.1167/11.5.13

[90] Guenter, B., Finch, M., Drucker, S., Tan, D. & Snyder, J. Foveated 3D graphics. in *ACM Transactions on Graphics* (2012). doi:10.1145/2366145.2366183

[91] Lucente, M. E. Interactive computation of holograms using a look-up table. *J. Electron. Imaging* (1993). doi:10.1117/12.133376

[92] Shimobaba, T., Nakayama, H., Masuda, N. & Ito, T. Rapid calculation algorithm of Fresnel computer-generated-hologram using look-up table and wavefront-recording plane methods for three-dimensional display. *Opt. Express* (2010). doi:10.1364/oe.18.019504

[93] Kim, S.-C., Dong, X.-B., Kwon, M.-W. & Kim, E.-S. Fast generation of video holograms of three-dimensional moving objects using a motion compensation-based novel look-up table. *Opt. Express* (2013). doi:10.1364/oe.21.011568

[94] Shi, Y., Cao, H., Gu, G. & Zhang, J. Technique of applying computer-generated holograms to airborne head-up displays. in *Holographic Displays and Optical Elements II* **3559**, 108–112 (2003).

[95] Cao, H., Sun, J. & Chen, G. Bicubic uniform B-spline wavefront fitting technology applied in computer-generated holograms. in *2nd International Symposium on Advanced Optical Manufacturing and Testing Technologies: Advanced Optical Manufacturing Technologies* (2006). doi:10.1117/12.674234

[96] Li, S. *et al.* A practical method for determining the accuracy of computer-generated holograms for off-axis aspheric surfaces. *Opt. Lasers Eng.* (2016). doi:10.1016/j.optlaseng.2015.08.009

[97] Wyrowski, F. & Bryngdahl, O. Iterative Fourier-transform algorithm applied to computer holography. *J. Opt. Soc. Am. A* (1988). doi:10.1364/josaa.5.001058

[98] Morimoto, Carlos H., and Marcio RM Mimica. "Eye gaze tracking techniques for interactive applications." Computer vision and image understanding 98.1 (2005): 4-24.

[99] Świrski, L., Bulling, A., & Dodgson, N. (2012, March). Robust real-time pupil tracking in highly off-axis images. In Proceedings of the Symposium on Eye Tracking Research and Applications (pp. 173-176). ACM.

[100] G.Iannizzotto and F. L. Rosa, “Competitive Combination of Multiple Eye Detection and Tracking Techniques,” IRE Trans. Ind. Electron. 58(8), 3151–3159 (2011).

[101] Wood, E., & Bulling, A. (2014, March). Eyetab: Model-based gaze estimation on unmodified tablet computers. In Proceedings of the Symposium on Eye Tracking Research and Applications (pp. 207-210). ACM.

[102] Başak, U. Y., Kazempourradi, S., Yilmaz, C., Ulusoy, E., & Urey, H. (2019). Dual focal plane augmented reality interactive display with gaze-tracker. OSA Continuum, 2(5), 1734-1745.

[103] Kumar, N., Kohlbecher, S., & Schneider, E. (2009, October). A novel approach to video-based pupil tracking. In 2009 IEEE International Conference on Systems, Man and Cybernetics (pp. 1255-1262). IEEE.

[104] Lee, J. W., Cho, C. W., Shin, K. Y., Lee, E. C., & Park, K. R. (2012). 3D gaze tracking method using Purkinje images on eye optical model and pupil. Optics and Lasers in Engineering, 50(5), 736-751.

[105] https://www.renesas.com/eu/en/doc/application-note/an1737.pdf

[106] Devereux, H., & Smalley, M. (1995, October). Are infra red illuminators eye safe?. In Proceedings The Institute of Electrical and Electronics Engineers. 29th Annual 1995 International Carnahan Conference on Security Technology (pp. 480-481). IEEE.